Aspects of astroparticle physics in the precision measurement era

A thesis submitted in partial fulfilment of

the requirements for the degree of

Doctor of Philosophy

by

Ashish

(Roll No. 15330016)

Under the supervision of

Prof. Subhendra Mohanty

Professor

Theoretical Physics Division

Physical Research Laboratory, Ahmedabad, India.

DISCIPLINE OF PHYSICS

INDIAN INSTITUTE OF TECHNOLOGY GANDHINAGAR

2020

to

My Family

कुछ कटी हिम्मत-ए-सवाल में उम्र
कुछ उमीद - ए - जवाब में गुज़री

-फ़ानी बदायुनी (1879 - 1941)

Declaration

I declare that this written submission represents my ideas in my own words and where others' ideas or words have been included, I have adequately cited and referenced the original sources. I also declare that I have adhered to all principles of academic honesty and integrity and have not misrepresented or fabricated or falsified any idea/data/fact/source in my submission. I understand that any violation of the above will be cause for disciplinary action by the Institute and can also evoke penal action from the sources which have thus not been properly cited or from whom proper permission has not been taken when needed.

Signature

Name: Ashish

(Roll No: 15330016)

Date:

Department of Physics
Indian Institute of Technology Gandhinagar
Gandhinagar, Gujarat-382355

CERTIFICATE

This is to certify that this thesis titled **"Aspects of astroparticle physics in the precision measurement era"** submitted by **Mr. Ashish (Roll No. 15330016)** to the Indian Institute of Technology Gandhinagar, is a record of bona fide research work carried out under my supervision and has not been submitted elsewhere for a degree. I have read this dissertation and in my opinion, it is fully adequate, in scope and quality, for the degree of Doctor of Philosophy.

Prof. Subhendra Mohanty
Theoretical Physics Division,
Physical Research Laboratory,
Ahmedabad, India.

(Thesis Supervisor)

Date:

Thesis Approval

The thesis entitled

Aspects of astroparticle physics in the precision measurement era

by

Ashish

(Roll No. 15330016)

is approved for the degree of

Doctor of Philosophy

Examiner

Examiner

Supervisor

Chairman

Date:

Place:

Acknowledgments

The work presented in this thesis would not have been possible without the help and support that I received from many people. I take this opportunity to extend my sincere gratitude and appreciation to all those who made this Ph.D thesis possible.

Foremost, I would like to express my sincere gratitude to my advisor Prof. Subhendra Mohanty whose continuous imparting of his genius convincingly guided and encouraged me to be professional and do the right thing in science and life, even when the road got tough. Without his persistent help, this thesis would not have been realized. I could not have imagined having a better advisor and mentor for my training as a scientist.

I would like to express my deepest appreciation to my Doctoral Studies Committee members, Prof. Jitesh R. Bhatt and Prof. Namit Mahajan, for all the time and effort they had put in reviewing my progress and keeping me on the right track throughout my PhD. My sincere thanks also goes to other current and previous members of THEPH division Prof. S. D. Rindani, Prof. Raghavan Rangarajan, Prof. Jay Banerji, Prof. Srubabati Goswami, Prof. Hiranmya Mishra, Prof. Dilip Angom, Prof. Partha Konar, Prof. Navinder Singh, and Dr. Ketan Patel from whom I have learnt a lot through their lectures and discussion during various seminars. I extend my special thanks to Prof. Namit Mahajan and Prof. Srubabati Goswami for their precious advises which helped in handling numerous personal issues.

I would like to extend my sincere thanks to my collaborators Dr. Gaetano Lambiase, Dr. Soumya Sadhukhan, Dr. Abhass Kumar, Dr. Bhavesh Chauhan, Dr. Bharti Kindra and Priyank Parashari who directly or indirectly helped me understand how science is done in practice. I am also thankful to Anshika for careful reading of this thesis.

I am thankful to all the staff members of our division, library, computer center, administration, dispensary, canteen, workshop and maintenance section of PRL for their assistance and support. I also take this moment to express my gratitude to the academic and administrative staff members of IIT Gandhinagar for helping with the registration procedures.

I must add that the journey on this path would not have started without the motivation from my teachers Prof. A. K. Kavathekar and Prof. T. R. Seshadri and my friends Prerna, Kiran, Gaurav, Raj, Garima and Brijesh at Delhi University. I am thankful to them for all those conversations and discussions about science and life.

Numerous thanks to Harsh for always being there with me on this roller coaster ride. I would also like to thank my friend Kaustav, with whom I have been sharing my office for last four years, for patiently putting up with me all this while. I am also thankful to Aarthy and Harsh for bestowing me with their friendship and all the fun that comes with it since the first day of PhD. I express my thanks to my friends and batch-mates Balbeer, Arvind, Richa, Akanksha, Naman, Archita, Subir, Shivangi, Rahul, Varun, Nidhi and Shefali for keeping life upbeat throughout these five years.

I thank my badminton buddies Aman, Vishnu, Nijil, Pradeep, Ila, Deepthi, Manu, Girish, Aravind, Amit, Atif, Sovan, Jivan and Deva for the stress-busting badminton drills every evening. I am also grateful to all the fellow researchers from PRL for the numerous helps and the support that they have given at various times. Especially, I would like to mention Gaurav, Girish, Ujjal, *Soumya, Abhishek, Rukmani, Tripurari, Tanmoy, Abhaya, Lata, Ikshu, Anil, Shraddha, Navpreet, Shweta, Sukanya, Surya, Ayon, Tanmay, Vishal, Deepak, Sudipta, Amit, Pravin and Hrushikesh. Kindly forgive if I have left out anyones name and please know that I am thankful to all of you.*

My parents and sisters have been a constant source of unconditional support and encouragement throughout my life. This thesis would not have been possible without their backing. I reserve my most sincere and deepest thanks for them.

Pandemic Mentions: Life took a drastic turn due to the Covid-19 pandemic. I am immensely thankful to my hostel mates, Deva, Siddharth, Jivan, Supriyo, Deepak and Sarika and neighbors in PRL colony, Pragya, Nurul, Sangeeta, Rajesh, Dipali, Ashish, Riya, Abhishek, Vishnu, Asha, Srishti and Sujata for numerous helps they provided to me and my parents during these tough times. I am also grateful to Shameem for letting me use his house to ensure safe stay of my parents during the pandemic.

Ashish

Abstract

Astroparticle physics is a synthesis of particle physics, cosmology and astrophysics which enables us to study high energy particle physics phenomena in natural laboratories like early universe and black holes using natural probes such as cosmic microwave background radiation (CMBR), cosmic rays (CR) and gravitational waves (GW). Till the end of the 20th century, the standard model (SM) of particle physics, the standard model of cosmology (ΛCDM model) and Einstein general relativity (GR) were immensely successful at explaining the observed particle interactions, the observed evolution of the expanding universe and gravitational observations, respectively. The advent of the precise measurements at all these fronts have brought into light several shortcomings of these models and hence a need to go beyond the so called standard picture is indispensable. The observation of neutrino oscillation confirms that neutrinos have non-zero mass, which is in direct conflict with both SM and ΛCDM model. Moreover there is no particle candidate for dark matter (DM) in the SM. Additionally, in the ΛCDM model, there are discrepancies in determination of two derived parameters, namely the H_0 (Hubble parameter) and the σ_8 (density fluctuations at 8 Mpc length scale) between two different observations (CMBR and large scale structure) and also there is no theoretical explanation of the so called coincidence problem. The recent observation of the M87* black hole shadow by the event horizon telescope (EHT) has a possible deviation(< 10 %) from the shadow predicted by Einstein's general relativity which opens a window to consider other theories of gravity.

In this thesis, the focus has been on extending the standard models to address the above mentioned issues. The ν2HDM (Neutrinophilic 2-Higgs doublet model), which is an extension of the SM by one Higgs and three right handed neutrinos explains the non-zero neutrino mass and provides a viable dark matter candidate in the form of the neutral component of the second Higgs. This model also provides an explanation to the long-standing problem of non-observation of Glashow resonance at the IceCube neutrino detector. At the cosmological front, to address the cosmological parameter discrepancies, the coincidence problem and the incorporation of massive neutrinos in the cosmological model a comparative study of two dark energy models, namely Hu-Sawicki (HS) model and dynamical dark energy (DDE) model suggests that the resolution of parameter discrepancies prefers DDE model over HS model. At the gravity front, a study of Kerr-Sen

black hole (KSBH), which emerges as a solution to 4-dimensional heterotic string theory and has axionic hair, in the light of EHT observation reveals that even more precise measurements of the shadow along with the polarimetric observation of the black hole are required to concretely conclude M87* to be a KSBH.

Contents

List of Figures

Chapter 1

Introduction

1.1 A Brief Introduction to Astroparticle Physics

The discovery of the expanding Universe suggests that the Universe originally was of a very small size and later on expanded to the present form. At primordial times the Universe was a microsystem that can only be studied in terms of elementary particles. The high temperature (energy) scales of the early Universe can never be reached in earth-bound laboratories. On the other hand, the energy of ultra high energy cosmic rays (CR) - particles coming to earth from extraterrestrial objects- are also way beyond the reach of particle accelerators at the earth. Therefore, to probe the fundamental interactions of particles in the primordial Universe and also through cosmic ray production and propagation, a symbiosis of particle physics, astrophysics and cosmology is called for. Astroparticle physics is such a union of the above mentioned fields in which the fundamental particle interactions are studied using several messengers such as cosmic microwave background radiation (CMBR), cosmic rays (CR), gravitation waves (GW) etc.

The standard model (SM) of particle physics is widely tested and accepted paradigm of particle interactions at the present time. The SM is based on the non-Abelian symmetry group $SU(3)_C \times SU(2)_L \times U(1)_Y$ and describes the behavior of 12 fermions (six quarks and six leptons, which are often arranged into the three 'generations' owing to the observed behavioral similarities), under the electromagnetic, weak and strong forces [1–3]. Each fermion has an antimatter counterpart, which the Standard Model treats in the same way as its matter equivalent. The Lagrangian of the standard model is given by

$$\begin{aligned}\mathcal{L} &= \bar{q}i\not{D}q + \bar{\ell}i\not{D}\ell - \frac{1}{4}\left(F^a_{\mu\nu}\right)^2 \\ &\quad + |D_\mu\phi|^2 - V(\phi) \\ &\quad - \left(\lambda^{ij}_u \bar{u}^i_R \phi \cdot Q^j_L + \lambda^{ij}_d \bar{d}^i_R \phi^* \cdot Q^j_L + \lambda^{ij}_\ell \bar{e}^i_R \phi^* \cdot L^j_L + \text{h.c.}\right) \end{aligned} \tag{1.1}$$

The first line of Eq. 1.1 is the pure gauge theory mentioned in the previous paragraph and describes the couplings of all species of quarks (denoted by q, Q, u and d) and leptons (denoted by ℓ, e and L) to the strong, weak, and electromagnetic gauge boson. The second line of Eq. 1.1 is associated with the Higgs field (ϕ), a doublet of SU(2), whose vacuum expectation value (vev) gives mass to W and Z bosons. The third line of Eq. 1.1 gives mass to all the matter particles, quarks and leptons through the vev of Higgs. When ϕ acquires a vev, the matrices λ^{ij} become the mass matrices of quarks and leptons. Notice that there are only singlet right haded quarks and leptons in the Eq. 1.1, this is because the left-handed and right handed fields belong to different representation of the $SU(2) \times U(1)$. Also there are no right handed neutrinos in the SM and hence rendering them massless. Neutrinos interact only through weak interactions and hence their interaction cross section with other particles in very small. This small cross section, on one hand is a bane because it demands detectors of very large size for detection of neutrinos but on the other hand this turns out to be a boon in the neutrino astronomy. Due to the small cross section, the astrophysical neutrinos coming from distant sources reach to earth almost unperturbed and unattenuated, making the tracing of their sources much easier in comparison to charged messengers. This nature of neutrinos makes them a unique messenger to probe and locate the most violent processes in the Universe which produce particles of energy much higher than that produces in laboratory experiments on earth. Several astrophysical objects such as Blazar, Quasar, Active Galactic Nuclei(AGN) are promising sources of these high UHE neutrinos. The general production mechanics of neutrinos in such sources is through the acceleration of protons due to high temperature and magnetic field. During the acceleration and propagation, these protons interact among themselves and also with other particles such as photons and neutrinos through the processes shown in Fig. 1.1. The present and proposed neutrinos telescopes such as IceCube [4], ANTARES [5], ANITA [6], ARIANNA [7] aim to look for these high energy neutrinos through their interactions with large collection of ice and water.

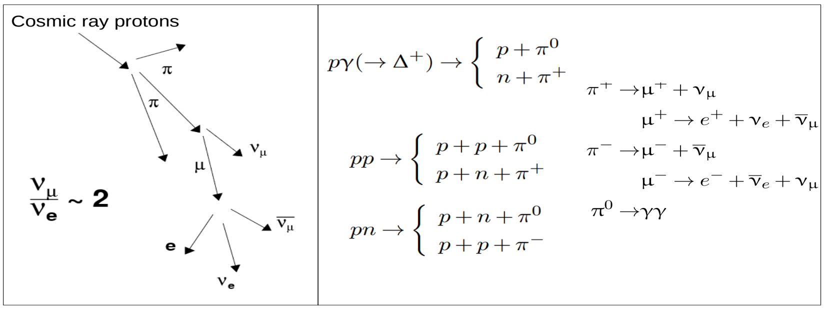

Figure 1.1: The production of Cosmic Ray neutrinos is schematically shown here. Notice that ν_μ to ν_e ratio is 2 at the end of the neutrino production chain.

The other most important constituent of the astroparticle physics is cosmology. The ΛCDM (cold dark matter) model is the largely accepted standard model of cosmology based on the assumptions of large scale homogeneity and isotropy. At the heart of the ΛCDM model lies the isotropic homogeneous Friedman-Robertson-Walker (FRW) metric which when treated into Einstein's theory of general relatively (GR), describes the observable Universe successfully. The ΛCDM model is based on the big bang hypothesis, according to which the Universe originated from a space-time singularity and then expanded at different rates during its 13.8 billion years long evolution to the present state. The Universe at the big bang is expected to have near infinite density and temperature and therefore we cannot explain the exact big bang instant with the existing theories of physics. A theory of quantum gravity is required to study the evolution of the Universe at that epoch.

A generally expected paradigm of the Universe just after the big bang is the inflationary paradigm during which the Universe expanded at an exponential rate and cooled down as a consequence of the expansion. Inflation was first proposed in [8–15] to solve the *horizon* problem (extreme homogeneity at non-causal length scales) and the *flatness* problem (curvature of the Universe being $\sim$0 today). In the inflationary model, the apparent causally disconnected regions were in contact before the end of inflation and hence are homogeneous. Whereas the flatness problem is resolved by the exponential expansion which dilutes the curvature during inflation, a longer inflation makes $\Omega_{\rm tot}$ (total energy density of the Universe) closer to 1 at its end. To solve both the flatness and the horizon problems, inflation should have lasted for at least 50 to 60 *e-foldings*, i.e., the length scales of the Universe should increase by e^{50} to e^{60} times as a result of the inflation. Inflation is usually parameterized by a scalar field ϕ, called *inflaton* which decays into other particles as it evolves to settle to the lowest values of potential $V(\phi)$ at the end of the inflation. As a result of this decay the energy of the inflaton is transferred to the decay products. This phase is termed as *reheating*, since the temperature of the resulting plasma is higher due to the increase in the overall particle density of the Universe. These decay products of the inflaton are the fundamental particles of nature which obey the symmetries and interaction rules of the standard model of particle physics.

As the Universe expands further its temperature continuously decreases and the kinematics of the constituents of the plasma keeps changing according to the temperature of the Universe. At a certain temperature, when the production rate of a particle goes below the expansion rate of the Universe, the production of that particle stops and the particle disappears from the plasma by annihilating into the lighter particles. A particle that goes out of thermal equilibrium of the plasma is said to be decoupled from the plasma. During the course of evolution, as a result of cooling some of the symmetries of the SM that were perfectly intact in the hot Universe start to spontaneously break: electroweak symmetry gets broken at 160 GeV and as a result the leptons, quarks and bosons of the weak interaction get mass. These particles which are produced relativistic become non-relativistic once the temperature drops below their mass. Further decrease in the temperature reduces the kinetic energy of quarks for them to combine and produce protons and neutrons and hence this epoch is called the hadron epoch.

Before this time, the dark matter (DM) particle can go out of equilibrium, depending on their mass. The rate of annihilation of DM depends on the square of number density which decreases as the Universe expands.

At a temperature of around 1 MeV, the neutrino-electron interaction ceases to exist and therefore the neutrinos decouple from the rest of the plasma. This relic of the neutrinos is called *Cosmic Neutrino Background* (CνB). The very low energy of CνB and extremely weak interaction strength of neutrinos makes it very hard to be detected directly. However, there are several indirect hints of CνB. Most prominently, the number of relic relativistic species is highly compatible with the presence of three relic neutrinos, but an assured signature of these relic relativistic particles being SM neutrinos is still needed.

Shortly after neutrino decoupling, the photon temperature goes below the mass of the electron and hence the production of electron-positron pairs stops and electrons start to decouple. The photons take away the energy from the electrons through the annihilation process $e^+e^- \to 2\gamma$. As a result, the temperature of the photon is higher than the neutrino. As the photon energy goes below 0.1 MeV, the nuclear bounds start forming and the production of light nuclei starts through hadron scatterings. The protons and neutrons combine to form the deuterium (^2H) nuclei. Further inelastic scatterings produce stable elements ^3He, ^4He, ^7Li and some unstable elements such as ^3H, ^7Be, that decay into ^3He and ^7Li.

Photons still have enough energy to break the electron-nucleus bounds and therefore the plasma is still charged. After the matter radiation equality, photons and relic neutrinos become less and less abundant as the Universe becomes matter dominated. As the photon temperature reaches $\sim 0.1\,\mathrm{eV}$, electron-nucleus dissociation is no longer possible and hence neutral atoms start coming into existence and the Universe become devoid of charged particles. As a result, the photons start streaming through the Universe uninterrupted. These freely moving photons constitute the cosmic microwave background (CMB) which we currently observe as a black body radiation of 2.73 K coming from all directions in the sky. This epoch is called the recombination and the time surface of last scattering of photons is called last scattering surface. In addition to providing the solutions for flatness and horizon problem through accelerated expansion, inflation also generates quantum fluctuations called primordial perturbations. Since all the matter and radiation is produced as a decay product of inflaton, the signature of the primordial fluctuations is also transferred to them. As a result, the CMB and the neutral matter, after the last scattering surface have imprints of these primordial fluctuations. The effect of these fluctuations on the CMB spectrum is seen as the temperature anisotropy at the 10^{-5} order over a constant 2.73 K background. From the last scattering surface to the present epoch, the CMB photons interact rarely. Therefore the study of CMB reveals information of the recombination epoch, and also of the earlier Universe through the CMB anisotropies generated because of primordial perturbations. The neutral matter after the CMB decoupling evolves under the action of gravity leading to the formation of large scale structures

(LSS) in the Universe. The CνB is also expected to have anisotropies generated through the same mechanism, studies of which would complement the deductions from the CMB anisotropies. However, the current detection technologies and precision render the study of the CνB anisotropies extremely difficult.

CMB measurements in past 3 decades have established inflation as the most successful explanation of the generation of CMB anisotropies. However, these measurements do not specifically prefer any particular particle physics model out of innumerable models of inflation. To explain the CMB observation within the ΛCDM model, a set of minimum six independent parameters is needed, which are as follows:

1. The amplitude of primordial scalar perturbations A_s and,
2. The tilt n_s of the power spectrum of the primordial fluctuations;
3. The baryon density fraction today $\Omega_b h^2$;
4. We can use either the CDM density fraction $\Omega_c h^2$ or the total matter density fraction $\Omega_m = \Omega_b + \Omega_c$;
5. The optical depth to reionization, τ_{re};
6. Assuming a spatially flat Universe, we can either consider H_0 or the cosmological constant density fraction Ω_Λ. Since for a fixed Ω_m the evolution of Hubble parameter is only because of Ω_Λ through the relation $H^2(z) = H_0^2(\Omega_m + \Omega_\Lambda)$, therefore we can write $\dfrac{H_0}{100\text{Kms}^{-1}\text{Mpc}^{-1}} \equiv h = \dfrac{\Omega_m}{1-\Omega_\Lambda}$.

With this set of six parameters, the ΛCDM model is immensely successful in explaining the current observations of CMB and LSS. As we will see in Ch. 4 that this set of six parameters is not unique in the ΛCDM model. Also, the number of parameters can be more than six in other cosmological models.

At the fundamental level, any cosmology theory relies on a theory of gravity parametrized by the metric of the space-time of the Universe. General relativity is the theory of gravity at the core of the ΛCDM model. The unparalleled success of GR in explaining the plethora of observations has established it as the most competent theory of gravity. The gravitational redshift, mercury's perihelion shift, gravitational lensing are a few such phenomena. The expanding Universe and the existence of black hole are two remarkable predictions of GR which have attained outstanding approval due to the observations of finite expansion rate of the Universe and recently by the gravitational wave observations by LIGO [16, 17]. In addition to the LIGO observation, the recent observation of black hole shadow adds more competency to GR [18–23].

In spite of the enormous success, there are domains such as black hole and big bang singularities [24–26], where GR loses its predictive power. Also, the ultraviolet character of gravity remains elusive in GR. Observations in the high curvature regions, where the energies are of the order of Planck mass, are expected to suggest features of a complete theory of gravity and its quantum nature [27–30]. There are several candidates for the alternate theory of gravity. The list includes $f(R)$ theories [31–33], Lanczos-Lovelock models [34, 35], higher dimensional theories[36–41], scalar tensor theories [42–44] and many other string inspired models of gravity [45–49].

1.2 Organization of the Thesis

In this thesis, the focus has been on extending the standard models to address observations that do not agree with the standard picture.

The thesis is organized in the following manner: Chapter one gives a brief introduction of astroparticle physics and its constituting fields. Chapter two discusses observations that motivate the studies beyond the standard models of cosmology and particle physics. These two chapter constitute the introduction and motivation of the thesis.

In Chapter three, we discuss the ν2HDM model, which is an extension of the SM by one Higgs and three right handed neutrinos. We explain the non-observation of Glashow resonance at the IceCube neutrino detector and the non-zero neutrino mass generation in this model. A further extension of this model by a singlet scalar provides a viable dark matter candidate. In Chapter four, we provide a comparative study of three cosmological models namely, ΛCDM model, HS model and DDE model to address the discrepancies in the assertion of cosmological parameters from different observations. We also give bounds on neutrino mass in these models. In Chapter five, we discuss the possibility of M87* being a Kerr-Sen black hole in light of the black hole image observed by the Event Horizon Telescope. We also provide a study of polarization of light coming from the black hole due to axion-photon interaction around the KSBH and conclude that a simultaneous study of shadow and polarization can give a distinct signature of KSBH.

Chapter six includes the discussion over the outcomes of the thesis and conclusion of the thesis.

Chapter 2

Signatures Beyond the Standard Picture

Despite the immense success, the so called standard models of particle physics and cosmology fail to accommodate some of the recently observed phenomena. The observation of neutrino oscillation [50] confirms that neutrinos have non-zero mass, which is in direct conflict with both SM and ΛCDM model. Moreover, there is no particle candidate for dark matter (DM) in the SM. Additionally, in the Lambda-CDM model, there are discrepancies in determination of cosmological parameters from early and late time Universe [51, 52] and there is no theoretical explanation of the so called coincidence problem as well [53]. The recent observation of the M87* black hole shadow by the event horizon telescope (EHT) has a possible deviation($\lesssim$ 10 %) from the shadow predicted by Einstein's general relativity. All these observations certainly demand to explore the theories beyond the standard picture. In this chapter we discuss these discrepancies in detail and emphasize the need for beyond standard theories for their explanations.

2.1 IceCube Observations

The IceCube Neutrino Observatory (IceCube) [54], located near the Amundsen-Scott South Pole Station in Antarctica, is a neutrino telescope comprising of an array of Digital Optical Modules (DOMs) distributed over 86 strings with 60 DOMs over each. The DOMs on each strings are separated by 17 m and the strings are separated by 125 m. The whole array is immersed in ice starting 1450 m below the Antarctic surface and extends upto 2450 m. The central array, called DeepCore [54] has DOMs distributed with higher

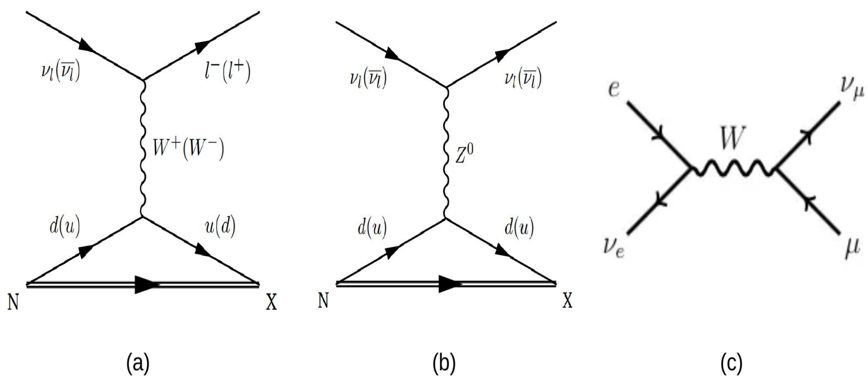

Figure 2.1: Feynman diagrams for Charged Current (CC), Neutral Current (NC) and Glashow Resonance are shown in (a), (b) and (c) respectively.

density.

The ultra high energy cosmic ray neutrinos can interact with the nucleons or the electrons in the ice. The neutrino-nucleon interactions are mediated by neutral current (NC) or charged current (CC), whereas the interaction with electron is always mediated by the CC. The Feynman diagrams for these interactions are depicted in Fig. 2.1. These interactions produce relativistic particles inside the detector that emit Cherenkov radiation. This radiation and its time of detection is recorded by the photon multiplier tubes (PMTs) in DOMs and is used to deduce the energy and direction of the neutrino. The two event topologies that have been reported so far are shower (or cascade) and tracks.

The cross sections of neutrino-electron cross section is very small as compared to that of neutrino-nucleon interaction and is ignored in general [55]. An exception to this is when an anti-neutrino of energy 6.3 PeV interacts with the electron. This interaction resonantly produces the W boson [56]. This resonance, called Glashow Resonance, should produce a spike of events at the energies close to 6.3 PeV in the event spectrum of the IceCube neutrino detection, however no such events are yet recorded at IceCube.

IceCube has observed a total of 82 high energy cosmic neutrino events in six years of its operation. A clear 6σ excess of events is observed at IceCube for energies above 60 TeV and these events cannot be explained by the atmospheric neutrinos [57]. The initial choices to explain the ultra high energetic (UHE) neutrino events were different astrophysical sources [58–61]. As the recent observation of the 290 TeV neutrino [62, 63] indicates, exploring these sources and the spectrum of neutrinos observed at IceCube lead

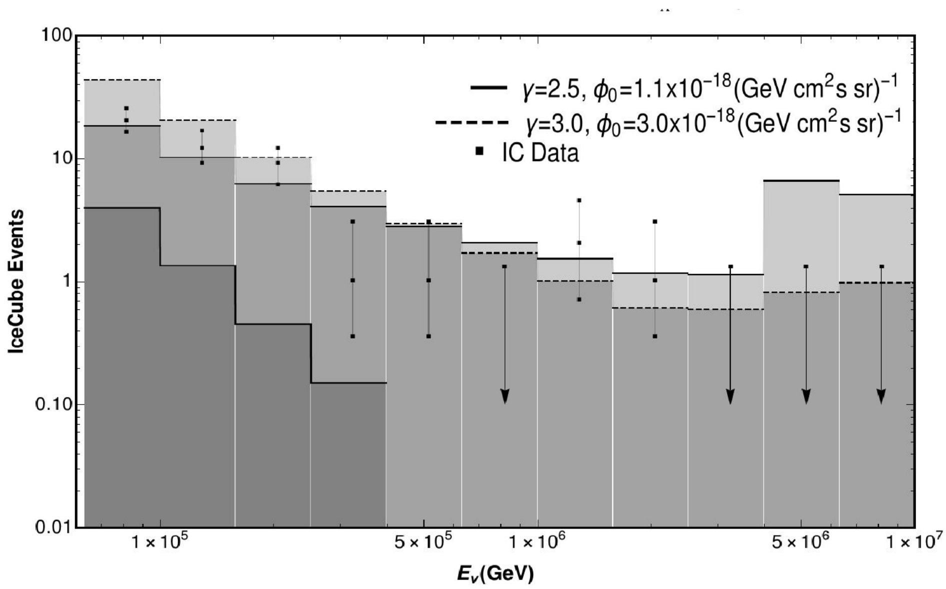

Figure 2.2: The limitation of using single power law is shown here. The dashed plot shows the IceCube even spectrum for a steeper power law whereas the solid plot is for a relatively flatter power-law flux. As can be seen that none of these fit the whole event spectrum satisfactorily.

us towards the conclusion that the events do point back to clear identifiable single power law astrophysical sources [64] (i.e. Active Galactic Nuclei (AGN), Gamma Ray Bursts (GRB) etc), mainly pointing to the neutrinos from the blazars. The power law neutrino flux is in general quantified as

$$\frac{d\Phi}{dE_\nu} = \phi_0 \left(\frac{E_\nu}{100 \text{ TeV}} \right)^{-\gamma} . \tag{2.1}$$

Fig. 2.2 shows the IceCube event spectrum with two benchmark specifications of power law cosmic ray neutrino flux. In both cases, it is difficult to have a good fit of the whole event spectrum. Each power law flux misfits either low energy bins ($60 - 600$ TeV) or the high energy bins (> 2 PeV). An attempt to fit the IceCube event spectrum with a steeper flux generally results in an excess of events in the sub-PeV which, when fixed by adjusting the amplitude of the flux results in deficit of events at energies $1 - 3$ PeV. Whereas, a flatter flux of neutrinos fits the events spectrum at lower energies but predicts larger event rate in the higher energy bins.

Various explanations of the observed 1 PeV excess feature in the IceCube event spectrum include neutrinos resulting from PeV dark matter decay or annihilation [65–69], the resonant production of leptoquarks [70–74] and the interactions involving R-parity violating supersymmetry [75]. On the other hand, there are depletion models which try to explain the non-observation of the Glashow resonance [56, 76–79]. The decay of the real W is expected to give hadron and lepton shower or lepton track events [80]. Depletion of high-energy neutrinos can occur via oscillation to sterile neutrinos in pseudo-Dirac neutrinos [81] and for visible decay [82]. Exotic scenarios have also been invoked to explain a cutoff at the Glashow resonance energies such as Lorentz violation [83, 84] and CPT violation [85].

2.2 Neutrino Mass

The discovery of neutrino oscillation by Takaaki Kajita and Arthur B. McDonald was conferred with Nobel Prize in physics in 2015. B. Pontecorvo first suggested that the neutrinos may exist in and oscillate between different flavors [86]. The observation of neutrino oscillation, after many years of Pontecorvo's proposal, opened several new dimensions in the modern particle physics. Existence of neutrino oscillations imposes the existence of mass of at least 2 neutrinos.

The probability of neutrino oscillation from one flavor to other ($\nu_\alpha \to \nu_\beta$) in three neutrino scenario is given by [87, 88]:

$$P_{\nu_\alpha \to \nu_\beta} = \delta_{\alpha\beta} - 4 \sum_{k \neq p} |U_{\alpha k}|^2 \left(\delta_{\alpha\beta} - |U_{\beta k}|^2\right) \sin^2 \Delta_{kp} + 8 \sum_{\substack{j>k \\ j,k \neq p}} |U_{\alpha j} U_{\beta j} U_{\alpha k} U_{\beta k}| \sin \Delta_{kp} \sin \Delta_{jp} \cos(\Delta_{jk} \overset{(+)}{-} \eta_{\alpha\beta jk}) , \tag{2.2}$$

where α and β are flavor index and the roman subscripts are mass index, and

$$\Delta_{kp} = \frac{\Delta m^2_{kp} L}{4E} , \qquad \Delta m^2_{jk} = m^2_j - m^2_k , \qquad \eta_{\alpha\beta jk} = \arg\left[U^*_{\alpha j} U_{\beta j} U_{\alpha k} U^*_{\beta k}\right] . \tag{2.3}$$

Here p is an arbitrary fixed index which can be chosen in the most convenient way depending on the case under consideration. For a fixed p, there exists only one possibility for j and k with $j > k$. As a consequence, in the case of three-neutrino mixing, there is only one interference term in Eq. 2.2.

As can be seen from the above relations, a non-zero oscillation probability requires non-zero squared mass difference between two neutrinos. The observation of neutrino oscillation (studies of survival probability of electron neutrinos) in neutrinos coming from the Sun leads to the solar squared-mass difference [89]

$$\Delta m^2_{\text{SOL}} \simeq 7.5 \times 10^{-5}\,\text{eV}^2\,, \tag{2.4}$$

whereas, the studies of neutrino oscillation with atmospheric neutrinos reveal the atmospheric squared-mass difference [50]

$$\Delta m^2_{\text{ATM}} \simeq 2.4 \times 10^{-3}\,\text{eV}^2\,. \tag{2.5}$$

The fact that these two mass difference are non zero guarantees that at least two of the three neutrinos are massive. We can conveniently label the masses of the three light neutrinos according to the convention

$$\Delta m^2_{\text{SOL}} = \Delta m^2_{21} \ll \Delta m^2_{\text{ATM}} = \frac{1}{2}\left|\Delta m^2_{31} + \Delta m^2_{32}\right|\,, \tag{2.6}$$

although there are several other definitions present in the literature (see e.g. Ref. [90]). The sign of Δm^2_{SOL} is already determined by the considerations of Mikheev-Smirnov-Wolfenstein (MSW) effect [91–93], generally referred as matter effect, in solar neutrino oscillations (see also Ref. [94, 95]). On the other hand, the sign and absolute value of Δm^2_{ATM} is still unknown. In consequence, we do not know the exact ordering of the masses of three neutrinos. The two possible orderings or hierarchies are:

- the normal hierarchy (NH)

$$m_1 < m_2 < m_3\,, \qquad \Delta m^2_{31},\, \Delta m^2_{32} > 0, \tag{2.7}$$

- the inverted hierarchy (IH)

$$m_3 < m_1 < m_2\,, \qquad \Delta m^2_{31},\, \Delta m^2_{32} < 0. \tag{2.8}$$

On the other hand, cosmological observations [96] also accept the existence of massive neutrinos. With the advent of more and more precise observations, cosmological bounds on neutrino mass are rapidly approaching the lower bounds predicted by neutrino oscillation experiments. Planck 2015 data release [96] gives upper limit of $M_\nu < 0.23$ eV (95% CL) using a combined analyses of CMB temperature anisotropy data, type Ia supernovae [97], BAO measurements [98–100] along with low-ℓ polarization and CMB lensing. Tighter constraints, $M_\nu < 0.15$ eV, were found in Ref. [101].

Precise observations to a level where mass sum < 0.1 eV can be used to decide the mass hierarchy of neutrinos. Upcoming cosmological surveys, such as the Large Synoptic Survey Telescope (LSST) [102] , Wide-Field Infrared Survey Telescope (WFIRST) [103], Euclid [104], Simons Observatory [105], and CMB-S4 [106] are expected to reach this precision.

The mass of fermions in the SM is generated through the coupling of right and left handed fermions with the Higgs. Neutrinos, unlike other fermions in the SM, do not have right handed partners and hence are massless in SM. However, we know from the experiments that at least two of the three neutrinos are massive. Any attempt to explain these small masses necessarily requires particles that are not part of the SM spectrum. The simplest models that generate the neutrino mass use the seesaw mechanism with heavy right-handed neutrinos (type-I) [107–109], scalar triplet (type-II) [110–112], or fermion triplet (type-III) [113]. In these scenarios, the lightness of neutrino masses is associated with the heaviness of new particle, hence the name seesaw.

2.3 Dark Matter

Fritz Zwicky first speculated the existence of DM more than eighty years ago through his studies of Coma cluster [114]. Zwicky's analysis concluded that to explain the motion of constituent galaxies of Coma cluster large amount of non-luminous matter is demanded, which he termed as *Dunkle Materie*. One of the most popular evidence of DM nowadays is galaxy rotation curve, i.e., the relation between the orbital velocity of visible stars and their radial distance from the center of the galaxy. Several galaxy observations dating back to late 30s [115] have concluded that the outer parts of the galactic disc move at velocities much higher than that expected from the motion under the influence of the visible matter only [116–118]. Similar conclusions about the existence of DM are also derived from the weak lensing measurements [119]. All these effects are due to the gravitational nature of the DM and do not tell anything about the total abundance and fundamental nature of the DM.

CMBR observations play an important role in determination of the matter content of the Universe. In ΛCDM model, the abundance of DM and baryonic matter is obtained by fitting power spectrum of CMB anisotropy using the six parameters described previously. The recent observations of CMBR [96] conclude that the matter content of the Universe is dominated by non-baryonic matter,

$$\Omega_b h^2 = 0.02207(27) \tag{2.9}$$

$$\Omega_{DM} h^2 = 0.1198(26) \tag{2.10}$$

whereas the remaining contribution is accounted for the so called *dark energy*, $\Omega_\Lambda = 0.0685$. The rotation curves of galaxies [120], the power spectrum of the CMB, and weak lensing measurements strongly suggest the existence of cosmological dark matter. However, the fundamental particle nature of dark matter still unknown. The only candidate for DM in the standard model of particle physics is neutrino but LSS data accompanied with deep-field observations suggest that the DM has non-relativistic velocities canceling the candidature of neutrinos for DM [121].

The requirements of DM to be neutral, non baryonic and non-relativistic can be fulfilled by a moderately heavy, weakly interacting particle. The weakly interacting massive particle (WIMP) is one popular paradigm wherein an elementary particle of mass approximately 100 GeV annihilating to SM particle with cross section of weak interactions gives the correct estimate of the relic abundance of the DM. This is known as the wimp miracle. However, recent results from several direct detection experiments such as LUX [122] and XENON100 [123] have imposed severe constraints on the multi-GeV mass window for various dark matter (DM) models which suggest that DM can be of lower mass scales. In the cosmological scenario, recent simulations of structure formation with WIMPs have suggested that there are discrepancies at the scale of galaxies (small scale crisis), majorly (i) core vs. cusp problem [124], (ii) missing satellites problem [125], (iii) diversity problem, and (iv) too big to fail problem [126].

2.4 Inconsistent Cosmological Observations

The cosmological parameter estimation within the ΛCDM model is done by measuring the CMB power spectrum. The most successful experiment in doing so is the state-of-the-art Planck satellite mission [127]. With every data release [51, 96, 128], the agreement between observations and the ΛCDM model has impressively increased. Despite this, there are several hints of deviation from the standard scenario which stayed along with all these data releases. There are tensions between Planck CMB observations and parameters estimated from some other cosmological probes. The direct measurements of the Hubble constant [129–131] gives a value 3σ away from the Planck measurement. There is also a mismatch between the value of H_0 obtained from Planck measurement and other late Universe large scale structure (LSS) measurements. Furthermore, there are evidences of more than 2σ tension in the $\sigma_8 - \Omega_m$ plane between Planck and cosmic shear experiments [132–137]. Moreover, the constraints obtained from high and low multipoles separately do not agree with each other [128, 138, 139].

In this thesis, the focus is on the discordance between σ_8 and H_0 measured from CMB and LSS surveys. In particular, the value of σ_8, the r.m.s. fluctuation of density perturbations at 8 h^{-1}Mpc scale and H_0, the value of Hubble parameter today which are inferred from CMB and LSS observations are out of accord [52, 140–145]. Fig. 2.3 illustrates this inconsistency between CMB and LSS observations. For this illustration, we use Planck CMB observations [96] for temperature anisotropy power spectrum over the multipole range $\ell \sim 2 - 2500$ and Planck CMB polarization data for low ℓ only. We refer to these data sets combined as Planck data. Whereas, in the LSS sector we use the baryon acoustic oscillations (BAO) data from 6dF Galaxy Survey [146], BOSS DR11 [98, 147] and SDSS DR7 Main Galaxy Sample [100] along with Planck SZ survey [148], lensing data from Canada France Hawaii Telescope Lensing Survey (CFHTLens) [149, 150] and CMB lensing data from Planck lensing survey [151] and South Pole Telescope (SPT) [152, 153]. We also use the data for Redshift space distortions (RSD) from BOSS DR11 RSD measurements [154]. We combine Planck SZ data, CFHTLens data, Planck lensing data, SPT lensing data and RSD data and refer them as LSS data.

σ_8-Ω_m^0 tension : The lensing potential ($C_\ell^{\phi\phi}$) determined from the weak lensing observation is quantified by two parameters: the matter-radiation equality scale, $k_{\rm eq}$ and amplitude of primordial perturbations, A_s [155, 156]. These two parameters thus in-turn control the matter power spectrum $P(k)$. The amplitude of $P(k)$ increases with A_s. However, the peak of $P(k)$ shifts with change in $k_{\rm eq}$. Hence, for a fixed k several combinations of A_s and $k_{\rm eq}$ can give same value for $P(k)$, i.e., A_s and $k_{\rm eq}$ are degenerate for a fixed $P(k)$. Therefore, the deduction of cosmological parameter using the matter power spectrum also

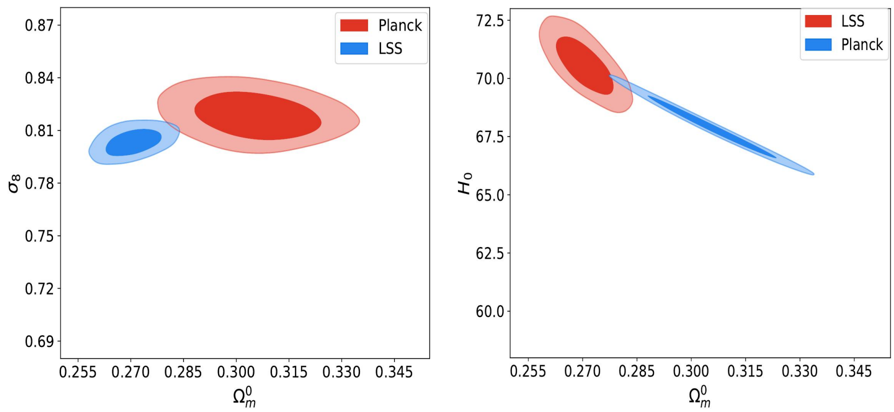

(a) (b)

Figure 2.3: Depiction of (a) σ_8-Ω_m^0 tension from LSS observations and Planck CMB observations, and (b) the mismatch in the allowed values of Ω_m^0 manifested as a mismatch in $H_0 - \Omega_m^0$ plane.

manifests this degeneracy in σ_8 and Ω_m. This is because σ_8 depends on A_s and Ω_m. Also, $k_{\rm eq} \equiv a_{\rm eq} H_{\rm eq} \propto \Omega_m h^2$.

Galaxy cluster surveys use SZ effect to count the number of clusters of a given mass within a given volume in the line of sight. This cluster count also depends on σ_8 and Ω_m and hence almost all of the LSS observations release their likelihoods in the σ_8-Ω_m^0 plane as

$$\sigma_8 \left(\frac{\Omega_m^0}{\Omega_{m,\,\rm ref}} \right)^{\alpha} = \text{const}\,. \tag{2.11}$$

For a particular observation, the values of α and $\Omega_{m,\,\rm ref}$ are so fixed such that the above relation remain independent of Ω_m. Hence, the values of α and $\Omega_{m,\,\rm ref}$ deduced for different observations are not same.

However, in the case of the CMB observations, the value of σ_8 is obtained by fitting a theoretical matter power spectrum with best fit values of Ω_m^0 and A_s obtained from CMB power spectrum fitting. In the ΛCDM model, there is a 2-σ mismatch between this value and the σ_8-Ω_m^0 degeneracy direction obtained from LSS observations (see Fig. 2.3). Although, the degeneracy is removed by a combined analysis of several LSS experiments but the region of σ_8-Ω_m^0 allowed from Planck CMB and LSS experiments still disagree.

H_0-Ω_m^0 **tension :** From the CMB observations the H_0 is inferred indirectly from the scale of baryon acoustic oscillations (BAO) at the recombination epoch. Similarly, in the LSS observations H_0 is measured indirectly through acoustic oscillations in matter power spectrum. Co-moving acoustic oscillation scale is a standard ruler in the cosmology which can be obtained from both CMB and LSS observations [157]. The co-moving distance at a given redshift z is

$$\chi(z) = \int_0^z \frac{dz'}{H(z')}\,, \tag{2.12}$$

where,

$$H(z)^2 = H_0^2(\Omega_m^0(1+z)^3 + \Omega_\Lambda)\,. \tag{2.13}$$

Given the value of Ω_m^0, BAO observations can fix value of H_0. Fig. 2.3 shows that the value of H_0 derived from CMB observations is more than that from LSS observations.

There have been discussion on these discrepancies being an artifact of systematics, however, several systematic studies over the years have failed to prove so and the tension still remains [138, 139, 158–162]. This, in a way, is a sign that we must consider the alternative models to bridge this gap between model dependent and model independent deduction of cosmological parameters.

There have been numerous attempts at resolving these discrepancies via non-standard cosmological models [163–177, and references therein], however, in most of these attempts the resolution of one tension worsens the other. Solving the Hubble tension requires either the reduction of the size of sound horizon, r_s by modifying early-universe cosmology [178–180], or the increment of the D_A to the CMB by introduction of new physics after the recombination epoch. On the other hand, solution to the σ_8 tension demands suppression of the linear matter power spectrum by modification of late-universe physics or a smaller value of Ω_m predicted from CMB.

2.5 Black Hole Shadow Observation

One of the most fundamental predictions of Einstein's theory of relativity is the existence of black holes. Schwarzschild BH (uncharged, non-rotating) and Kerr BH (uncharged, rotating) are two most common BHs predicted by the general relativity. According to *Kerr*

Hypothesis: an isolated, stationary, and axisymmetric astrophysical (uncharged) BH is always described by the Kerr metric. In other words, most commonly abundant BHs in the Universe are the Kerr BHs. Observation of gravitational waves coming from coalescing compact objects have more or less confirmed the existence of BHs [16, 17]. However, these observations give the information only about the violent merger stage and hence can be used to study metrics only via their dynamics. Whereas, to study several other BH phenomena such as information paradox, no hair theorem, Hawking radiation and horizon structure long time observations of particle dynamics around the BH are called for.

The Event Horizon (EHT) Telescope [18–23] is one such globally spread array of radio telescopes which enables the observation of particle dynamics in the close proximity of the BH. The aim of the EHT is to obtain the highest resolved images of astronomical objects such as BHs. The BH observation through the EHT should qualitatively show two distinct regions: a central dark region and a surrounding annular bright region. The bright region is formed by the photons reaching us from outside the horizon of the BH. The photon geodesics from the central region can't escape to the spatial infinity, rendering that region dark to us. The central darker region is called the *shadow* of the black hole. For a super-massive black hole (SMBH), the shadow appears in a strong gravity region near the event horizon and hence, in principle, it can be used to determine the properties of the BH space-time. Moreover, these EHT observations are longer duration observations of the stationary state of BH in comparison to the observation of gravitational waves coming from violent black hole mergers and hence complimentary. This complementarity between these two observations plays an important role in gravitational tests involving BHs since a large number of gravitational theories predict similar BHs with mild differences in particle dynamics and gravitational wave signals which can be probed with high resolution observation in the strong gravity region of the BH.

The recent extraordinary observation of M87* BH by the EHT measured the angular diameter of the BH shadow to be 42 ± 3 μas [18–20] with an axis ratio of $4/3$. The shadow is not entirely circular and the upper bound on the deviation of circularity is 10%. In general relativity the shadow of a rotating, uncharged black hole such as Kerr BH is highly circular irrespective of the inclination angle [181] assuming that the black hole can entirely be characterized by its mass and angular momentum. However, several other theories of gravity predict different shape, size and properties of BH shadow. Hence, deviation from circularity observed in the shadow of the M87* BH could be a sign of it being a non-Kerr BH and hence of a non-GR origin.

Chapter 3

Glashow Resonance, Neutrino Mass, Dark Matter

The absence of Glashow resonance in the IceCube event spectrum and the observation of more numbers of PeV events than expected have been the major outcomes of IceCube neutrino detection. In this chapter we try to resolve anomalies in IceCube neutrino event spectrum by invoking cosmic ray neutrino absorption enabled by ν2HDM (neutrinophilic 2-Higgs doublet model). We also provide neutrino mass generation through Type-I see-saw mechanism. The absorption of CRν by CνB through production of a new particle has been discussed earlier [182–187].

This chapter is organized as follows. In Sec. 3.1 We explore the method to compute the event spectrum of IceCube and bring to notice the features of the spectrum such as HESE events and Glashow resonance events, in the SM. In the next Sec. 3.2, we explain the ν2HDM and then in subsequent sections 3.3, 3.4 and 3.5 we provide resolutions to issues discussed in Sec. 2.1, Sec. 2.2 and Sec. 2.3 respectively within ν2HDM. Finally, we summarize and conclude this chapter in Sec. 3.6.

3.1 IceCube Events in SM

As explained in Sec. 2.1, the high energy cosmic ray neutrinos are detected at IceCube through deep inelastic scattering with the quarks and electrons (see Fig. 2.1) present in the detector volume. The expressions for the differential cross section for these interactions can be found in [55] which are shown in Fig. 3.1. The cross section of $\bar{\nu}_e e^-$ interaction at energies near $E_\nu = M_W^2/2m_e \simeq 6.3$ PeV is about 300 times higher than that of the charged current (CC) neutrino-nucleon interaction. As a result of higher cross section of Glashow resonance, a significantly higher number of events is expected in the IceCube event spectrum. However, as shown in Fig. 3.2, in the 6 years of its data collection IceCube has observed no GR events. This is in general referred to as the "missing Glashow resonance" problem.

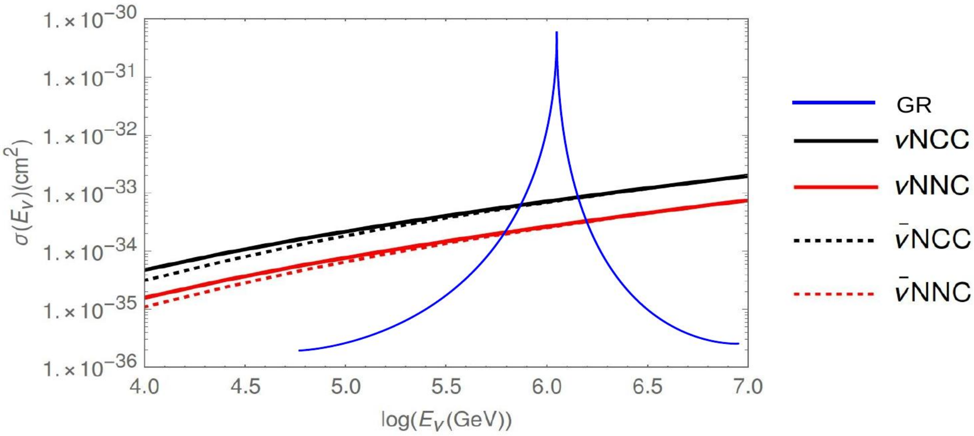

Figure 3.1: The cross section of ν-nucleon and $\bar{\nu}$-neucleon interaction along with the $\bar{\nu}_e e^-$ responsible for GR are shown here. The CS of $\bar{\nu}_e e^-$ is very large compared to interaction with nucleons at energy around 6.3 PeV

The number of events at IceCube in the deposited energy interval (E_i, E_f) is given by[84, 188, 189]

$$\mathcal{N} = T\, N_A \int_0^1 dy \int_{E_\nu^{ch}(E_i,y)}^{E_\nu^{ch}(E_f,y)} dE_\nu\, \mathcal{V}_{eff}(E_{dep}^{ch})\, \Omega(E_\nu)\, \frac{d\phi}{dE_\nu} \frac{d\sigma}{dy}^{ch}. \tag{3.1}$$

where the total exposure time for six year $T = 2078$ days, $N_A = 6.023 \times 10^{23}$ is the Avogadro's Number, and ch denotes the interaction channel (neutral current (NC), charged current (CC)). E_{dep}^{ch} is the deposited energy as explained in [190]. We have used $\Omega = 2\pi$ and $\Omega = 4\pi$ for the super-PeV ultra high energetic bins and sub-PeV IceCube bins respectively. The terms appearing in the above expression are explained in detail below.

- $\dfrac{d\phi}{dE_\nu}$ is the flux of the cosmic ray neutrinos. It is assumed that for neutrinos and anti-neutrinos of each flavor the flux is isotropic and is given by a power law flux parametrized as

$$\frac{d\Phi}{dE_\nu} = \phi_0 \left(\frac{E_\nu}{100\ \text{TeV}}\right)^{-\gamma}. \tag{3.2}$$

We take

$$\phi_0 = 1.1 \times 10^{-18} \text{GeV}^{-1} s^{-1} sr^{-1} cm^{-2} \tag{3.3}$$

$$\gamma = 2.5. \tag{3.4}$$

- $\mathcal{V}_{eff}(E^{ch}_{dep})$ is the effective volume of the detector available for the interaction, given by

$$\mathcal{V}_{\text{eff}}(x) = \begin{cases} \dfrac{1 + d\,x^q}{c\,x^q} & \text{if } x \geq 0 \\ \\ 0 & \text{if } x < 0\,, \end{cases} \tag{3.5}$$

where $x \equiv \log_{10}\left(\dfrac{E^{ch}_{dep}}{E_{\text{th}}}\right)$ with $E_{\text{th}} = 10$ TeV.

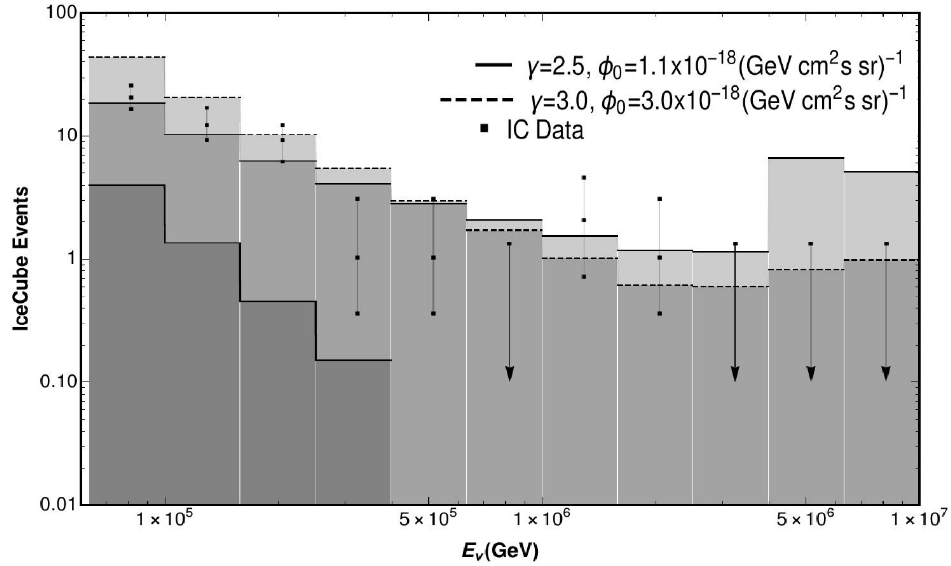

Figure 3.2: The IceCube event spectrum with a single power law flux of the cosmic ray neutrinos is shown here. The figure shows that with SM interactions and a single power law flux one cannot fit the IceCube data completely. SM with single power law flux expects events in the last three bins due to GR but there are no events seen in these bins.

- $\frac{d\sigma^{ch}}{dy}$ is the SM differential cross section of the neutrino-nucleon interaction. Depending on the channel ch of the interaction, these are given as

$$\frac{d^2\sigma^{(CC)}}{dx\,dy} = \frac{G_F^2}{\pi}\frac{2M_W^4}{(Q^2+M_W^2)^2}M_N E_\nu \{xq(x,Q^2) + x\bar{q}(x,Q^2)(1-y)^2\}, \tag{3.6}$$

$$\frac{d^2\sigma^{(NC)}}{dx\,dy} = \frac{G_F^2}{2\pi}\frac{M_Z^4}{(Q^2+M_Z^2)^2}M_N E_\nu \{xq^0(x,Q^2) + x\bar{q}^0(x,Q^2)(1-y)^2\} \tag{3.7}$$

and for the processes contributing to the Glashow resonance

$$\frac{d\sigma(\bar{\nu}_e e \to \bar{\nu}_e e)}{dy} = \frac{G_F^2 m_e E_\nu}{2\pi}\left[\frac{R_e^2}{(1+2m_eE_\nu y/M_Z^2)^2} + \left|\frac{L_e}{1+2m_eE_\nu y/M_Z^2} + \frac{2}{1-2mE_\nu/M_W^2 + i\Gamma_W/M_W}\right|^2 (1-y)^2\right] \tag{3.8}$$

$$\frac{d\sigma(\bar{\nu}_e e \to \bar{\nu}_\mu \mu)}{dy} = \frac{G_F^2 m_e E_\nu}{2\pi}\frac{4(1-y)^2[1-(m_\mu^2-m_e^2)/2m_eE_\nu]^2}{(1-2m_eE_\nu/M_W^2)^2 + \Gamma_W^2/M_W^2}\ , \tag{3.9}$$

and

$$\frac{d\sigma(\bar{\nu}_e e \to \text{ hadrons})}{dy} = \frac{d\sigma(\bar{\nu}_e e \to \bar{\nu}_\mu \mu)}{dy}\cdot\frac{\Gamma(W \to \text{ hadrons})}{\Gamma(W \to \mu\bar{\nu}_\mu)}\ , \tag{3.10}$$

where $\Gamma_W = 2.09$ GeV is the decay width of the W boson, $L_e = 2Sin^2\theta_W - 1$ and $R_e = 2Sin^2\theta_W$ are chiral couplings of Z to electron, and M_W and M_N are the W boson and the nucleon masses respectively, $-Q^2$ is the invariant momentum transferred to hadrons, and G_F is the Fermi constant. The Bjorken scaling variable x and the inelasticity y are defined as

$$x = \frac{Q^2}{2M_N E_\nu y} \quad \text{and} \quad y = \frac{E_\nu - E_\ell}{E_\nu}, \tag{3.11}$$

where E_ν is the energy of the incoming neutrino and E_ℓ is the energy carried by the outgoing lepton in the laboratory frame. $q(x,Q^2)$, $\bar{q}(x,Q^2)$, $q^0(x,Q^2)$ and $\bar{q}^0(x,Q^2)$ are quark distribution functions in the nucleon, the expression of and further details on which can be found in [55, 190]. Fig. 3.2 shows the IceCube event spectrum with 6 years IceCube data. We can see that no events have been seen where the dramatic increase of the event rate was expected due to the Glashow resonance.

3.2 The $\nu\mathrm{2HDM}$: Neutrinophilic 2-Higgs Doublet Model

In this section we present a new type of 2-Higgs doblet model (2HDM) called the "neutrinophilic 2-Higgs doublet model (ν2HDM)" [191, 192] which results from the idea that neutrino masses being much smaller than other fermions should originate from a Higgs with a smaller vev. The motivation for such an idea is derived from the following arguments. See-saw mechanism in minimal extentions of the SM naturallly gives the small masses of active neutrinos through heavy particles coupled with lef-handed neutrinos. However, the heavy particles in the picture are almost decouple from the low-energy scenario rendering the model intangible at low energies. A few corrective measures to this scenarios, such as [193–198], brought down the see-saw scale to TeV with the expectations that effects of TeV scale right-handed neutrinos might be seen in collider experiments. However, these models required a bit of fine tuning to generate tiny neutrino masses. The dependence of Dirac mass on Yukawa coupling and vev of the Higgs notifies that the smallness of neutrino masses might not be due to the small Yukawa coupling but a small vev, hence giving rise to the idea of 2HDM with second Higgs having a very small vev. For Example, a Type-II 2HDM with a large mixing angle (tan $\tan\beta$) explains the msss hierarchy of up-type quarks and down-type quarks through the ratio of Higgs vevs (a $\tan\beta \sim 40$ gives a unity Yukawa coupling for both up and down-type quarks). Similarly, the smallness of neutrino masses compared to other fermions and quarks can be due to a coupling to a different scalar doublet.

The ν2HDM theory is based on the symmetry group $SU(3)_c \times SU(2)_L \times U(1)_Y \times Z_2$ and contains three EW singlet right-handed (RH) neutrinos, N_{R_i}, for each flavor of SM lepton. In addition to that the model has two Higgs doublets, Φ_1 and Φ_2. All the charged fermions and the Higgs doublet Φ_1, are even under the discrete symmetry, Z_2, while the RH neutrinos and the Higgs doublet Φ_2 are charged under Z_2. Such a setup leads to Yukawa structure in which all the charged fermions couple with Φ_1 only and the left-handed neutrinos, together with the right-handed neutrino added here, couple to the Higgs doublet Φ_2. The breaking of Z_2 discrete symmetry by a vev of Φ_2 results in generation of mass for neutrinos through see-saw mechanism explained in Sec. 3.4.

The 2-Higgs potential of the CP invariant Higgs sector with Z_2 symmetry is given as [192]

$$V = -\mu_1^2\,\Phi_1^\dagger\Phi_1 - \mu_2^2\,\Phi_2^\dagger\Phi_2 + m_{12}^2\,(\Phi_1^\dagger\Phi_2 + h.c.) + \lambda_1(\Phi_1^\dagger\Phi_1)^2 + \lambda_2(\Phi_2^\dagger\Phi_2)^2 + \lambda_3(\Phi_1^\dagger\Phi_1)(\Phi_2^\dagger\Phi_2) + \lambda_4|\Phi_1^\dagger\Phi_2|^2 + \frac{1}{2}\lambda_5[(\Phi_1^\dagger\Phi_2)^2 + (\Phi_2^\dagger\Phi_1)^2]. \tag{3.12}$$

After the EW symmetry breaking, the two doublets can be written as follows in the unitary gauge

$$\Phi_1 = \frac{1}{\sqrt{2}}\begin{pmatrix} \sqrt{2}(v_2/v)H^+ \\ h_0 + i(v_2/v)A + v_1 \end{pmatrix},$$

$$\Phi_2 = \frac{1}{\sqrt{2}}\begin{pmatrix} -\sqrt{2}(v_1/v)H^+ \\ H_0 - i(v_1/v)A + v_2 \end{pmatrix}, \tag{3.13}$$

where charged fields $H^\pm$, two neutral CP even scalar fields h and H, and a neutral CP odd field A are the physical Higgs fields and $v_1 = \langle\Phi_1\rangle$, $v_2 = \langle\Phi_2\rangle$, and $v^2 = v_1^2 + v_2^2$. There is an orthogonal mixing of the charged and CP odd interaction states with corresponding charged and neutral Goldstone modes with a mixing angle β. As a result of the mixing mass eigenstates $H^\pm$, A and massless Goldstone bosons are produced. The mixing angle is expressed as $\tan\beta = \frac{v_2}{v_1}$. The masses of charged Higgs and the CP-odd Higgs in this model are of the order 100 GeV. This model also gives rise to a very light scalar H with mass varying from 1 eV to 1 GeV.

The mass eigenstates h, H are related to the weak eigenstates h_0, H_0 by

$$h_0 = c_\alpha h + s_\alpha H,\ \ H_0 = -s_\alpha h + c_\alpha H, \tag{3.14}$$

where $c_\alpha = \cos\alpha, s_\alpha = \sin\alpha$, and are given by

$$\begin{aligned} c_\alpha &= 1 + O(v_2^2/v_1^2), \\ s_\alpha &= -\frac{\lambda_3 - \lambda_4 - \lambda_5}{2\lambda_1}(v_2/v_1) + O(v_2^2/v_1^2). \end{aligned} \tag{3.15}$$

The vev of the seconds Higgs is taken to be $v_2 \sim 1$ keV (to fit the neutrino mass) which along with $v_1 \sim 246$ GeV gives rise to very small mixing and therefore can be neglected. This results in very small $\tan\alpha$ which in turn makes $\tan\beta$ small. Hence, the neutral scalar h effectively behaves like the SM Higgs. So we expect that the all the constraints on the coupling of the SM Higgs are also satisfied by h (see Sec. 3.2.1), except in the loops. The effect of $H^{\pm}$ loop in the $h\gamma\gamma$ constraints is given in Ref. [199] and also how a sizable Higgs invisible decay is allowed is also discussed.

3.2.1 Constraints on the Model

Peskin-Takeuchi oblique parameters S,T, U are measure of corrections to the gauge boson two point functions (Π_{VV}) [200]. The deviation of these oblique parameters from SM measured by the LHC are:

$$\begin{aligned} \Delta S^{SM} &= 0.05 \pm 0.11, \\ \Delta T^{SM} &= 0.09 \pm 0.13, \\ \Delta U^{SM} &= 0.01 \pm 0.11, \end{aligned} \tag{3.16}$$

In the model discussed here, we have very tightly constrained scalar sector, since we take $v_2 \ll v_1$ the mixing between the two Higgs is negligible. λ_1 is fixed by taking h to be the 125 GeV Higgs discovered at LHC. The other CP-even Higgs is very light and for typical quartic couplings within the perturbative limit, the masses of charged scalars and the CP-odd scalar are below the TeV scale. As a result of the presence of a light neutral scalar the oblique parameters S and T will play a decisive role in constraining the model. These constraints are discussed in [201].

The charged Higgs production at LHC in ν2HDM is same as in 2HDM. Due to the smallness of the mixing between the two Higgs the decays of charged Higgs to quarks are highly suppressed by the mixing factor $\tan\beta$. So the dominant channel of charged scalar decay is $H^{\pm} \longrightarrow l^{\pm}\nu$ which is constrained by LEP as $m_{H^{\pm}}$ 80 GeV. Charged Higgs can also contribute to di-photon production through loop. Even with that contribution the di-photon bound is satisfied. The status of constraints from flavor physics is given in [202]. Astrophysical consequences of ν2HDM are discussed in [203].

Due to difference in vacuum expectation value of two scalar doublets ($v_2 \ll v_1$), the mixing between two doublets is tiny. As neutrinos in our model couple only to Φ_2, so the SM Higgs coupling to ν, N is negligibly small and therefore, that decay does not affect any constraints. The other CP even scalar dominantly from Φ_2 is very light $m_H \sim 10$ MeV and with right handed neutrinos with masses around 15 MeV the $H \rightarrow \nu N$ decay is negligible even with order one scalar Yukawa coupling.

3.3 Cosmic Ray ν Absorption by CνB

As discussed in Sec. 1.1, Cosmic neutrino background (CνB) is the relic of the hot plasma from the early Universe. These neutrinos decouple from the hot plasma at $\sim$1 MeV and expected as an isotropic background with a temperature of $T_\nu = 1.95$K today. To resolve the enigma of absence of Glashow resonance at IceCube, we propose a scenario where CRνs interact with the CνB neutrinos inelastically to produce new particles which cannot produce any signatures at IceCube. This scenario is shown schematically in Fig. 3.3. When the CR neutrinos of energy much greater than T_ν hit the CνB neutrinos, CνB neutrinos can be considered as stationary. Since this absorption process would take place only if the CRν has enough energy to produce particles in the final state (particles A, B in Fig. 3.3), therefore depending on the masses of the particles in the final state the CRν of different energies can be absorbed. A and B are particles which go undetected through IceCube.

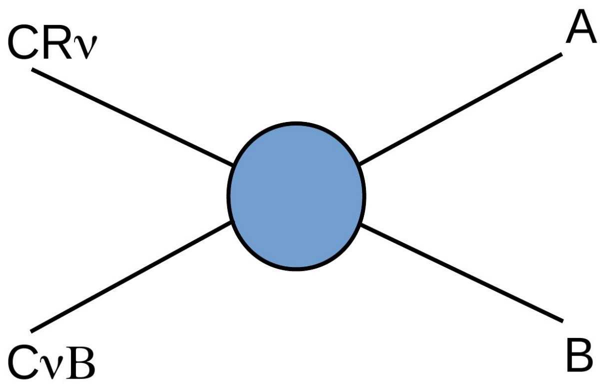

Figure 3.3: Schematic diagram of CRν capture by CνB neutrino.

3.3.1 Modification of CRν Flux

The ν2HDM discussed in Sec. 3.2 allows us to have one such process which serves as the capture of CRν by CνB. This t-channel process is special in the way that the mass of the mediator does not decide CRν of which energy will be absorbed, as is the case for such s-channel processes. Instead, the occurrence of the absorption process is managed by the mass of the CνB neutrinos and masses of the particles in the final state. The process takes place only if the CRν has sufficient energy,i.e., a threshold energy decided by the masses of the target and the product particles. Once the CRν has enough energy for the process to happen then the strength of the interaction is decided by other parameters like coupling and the mediator mass. The t-channel diagram is shown in Fig. 3.4 and its cross matrix element is computed as:

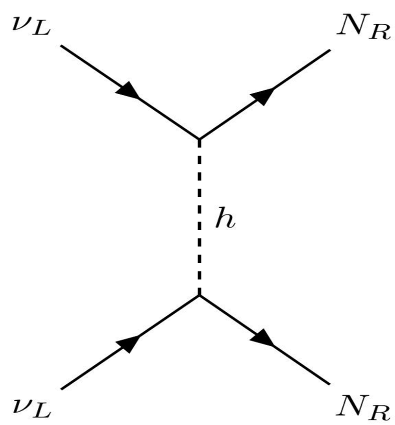

Figure 3.4: t-channel absorption of UHE neutrino by CνB

$$M^2 = \frac{4y_i^2 y_j^2}{(t - m_h^2)^2} \left(-\frac{1}{2}(t - m_R^2) + m_{\nu_i} m_R \right)^2 \tag{3.17}$$

where t represents the energy transfer to the final state right handed neutrinos. Here m_h and m_R are the ultralight scalar mass and the right handed neutrino mass respectively, with y being the neutrino-scalar Yukawa coupling. Depending on the mass of the final state right handed neutrinos N_R the t-channel process kicks off at certain neutrino energies, overcoming phase space barrier which renders the cross section to non-physical values at lower energies. The incoming UHE neutrino energy where this absorption process starts to kick off is called the cutoff of the neutrino spectrum.

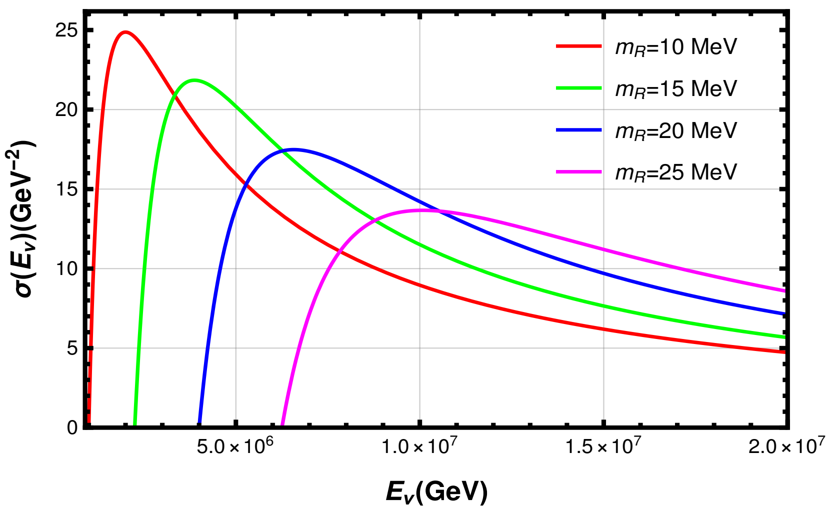

Figure 3.5: t-channel absorption cross section and its variation with m_R taking $y \sim 1$ and target neutrino mass 0.1 eV.

The variation of t-channel process cross section with incident neutrino energy is shown in Fig. 3.5. The cutoff neutrino energy for different m_R values are also shown there. Required energy threshold to kick off the process increases with m_R as production of heavier particles needs more energy transfer after absorption to enable this process kinematically.

The absorption of CRν modifies the CRν flux according to the nature of the interaction. The mean free path of this interaction is,

$$\lambda_i(E_i, z) = \left(\sum_j \int \frac{d^3\mathbf{p}}{(2\pi)^3} f_j(p, z) \sigma_{ij}(p, E_i, z) \right)^{-1} \approx \left(n_\nu(z) \sum_j \sigma_{ij}(p, E_i, z) \right)^{-1} \tag{3.18}$$

where f_i is the distribution function for the neutrinos given by,

$$f_i(p, z)^{-1} = \exp\left(\frac{p}{T_i(1+z)} \right) + 1 \tag{3.19}$$

and $T_i = 1.95\ K$ for all three mass states. Away from the sources, due to the mixing, flavor ratio of neutrinos in the cosmic rays is $(1:1:1)$. The mean free path (MFP) of the CRν is much greater than the coherence length ($\mathcal{O}(1)$ Mpc) of neutrinos, therefore the coherence is lost and hence the scattering process can be described in terms of mass eigenstates. Also, the (1:1:1) flavor ratio directly translates to (1:1:1) ratio in the three mass eigenstates. Away from the sources, each flavor and in-turn each mass eigenstate has power law flux. We express the modified flux due to the absorption as

$$\left(\frac{d\Phi}{dE_\nu}\right)_{cap} = \exp\left[-\int_0^{z_s} \frac{1}{\lambda_i}\frac{dL}{dz}dz\right]\frac{d\Phi}{dE_\nu} \tag{3.20}$$

where z_s denotes the redshift of source and,

$$\frac{dL}{dz} = \frac{c}{H_0\sqrt{\Omega_m(1+z)^3+\Omega_\Lambda}}. \tag{3.21}$$

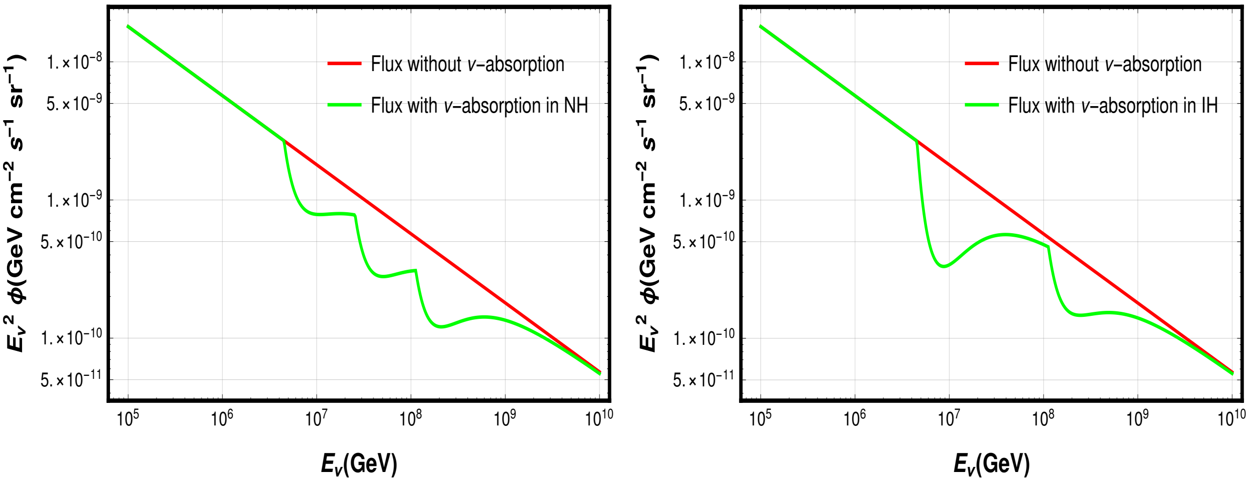

Figure 3.6: Comparison of $E_\nu^2\times$ flux for the incoming cosmic neutrinos after they got absorbed by the CνB (green) with that when there is no cosmic neutrino absorption (red) for a. normal mass hierarchy with $(m_1, m_2, m_3) = 2\times10^{-3}, 8.8\times10^{-3}, 5\times10^{-2}$ eV (left) b. inverted mass hierarchy with $(m_1, m_2, m_3) = 4.9\times10^{-2}, 5\times10^{-2}, 2\times10^{-3}$ eV (right). These benchmark values for neutrino masses chosen in such a way that they satisfy Eq. 2.4 to Eq. 2.8. Any set of values satisfying these relations would give the similar flux signatures.

Here the absorption cross section peaks at t-channel resonant condition, i.e., $t = m_h^2$, which in this process at the lab frame translates to $m_\nu E_\nu = m_h^2$. The cross section will peak at neutrino energies E_ν, where this condition will be satisfied. The peak will drastically increase the suppression factor for the corresponding neutrino energy, as we see in Eq. 3.3.1. The neutrino flux after incorporating the modification due to the t-channel absorption of CRν for all three mass eigenstates in (a) normal hierarchy and (b) inverted hierarchy is shown in Fig. 3.6.

3.3.2 Dips in IceCube Spectrum

These two right handed neutrinos, unlike their left handed partners, do not have charged current and neutral current interaction with IceCube matter therefore those will not be detected in the IceCube, which results in vanishing one astrophysical neutrino in this process. We have fixed two benchmark points in the standard cosmological description of single flux neutrino propagation. The effects of the presence of the t-channel absorption are shown for those scenarios.

- Benchmark Point-I:
  $\Phi_0 = 1.1 \times 10^{-18}\ (\text{GeV cm}^2\text{s sr})^{-1},\ \ \gamma = 2.5$

- Benchmark Point-II:
  $\Phi_0 = 1.18 \times 10^{-18}\ (\text{GeV cm}^2\text{s sr})^{-1},\ \ \gamma = 2.55$

We fix the initial UHE neutrino energy cutoff at 4.5 PeV i.e. the t-channel resonant absorption process will start to contribute only at incident neutrino energies higher that 4.5 PeV. To set this cutoff we need to have one N_R with mass at around $m_R \approx 15$ MeV. In Fig. 3.6, we plot the quantity $E_\nu^2\Phi_\nu$ to show how the incoming neutrino flux can be modified due to this t-channel cosmic neutrino absorption. This results in multiple dips in neutrino flux spectrum in some particular energies, for both the normal and inverted neutrino mass hierarchies. The first lower energy dip happens at $E_\nu \sim 5$ PeV, corresponding to the heaviest neutrino present in the cosmic neutrino background (CνB). For normal hierarchy the neutrino masses are well separated and therefore three different neutrino mass eigenstates produce three dips in the neutrino flux spectrum. On the other hand, for inverted mass hierarchy with tiny Δm_{12}^2, two heavier neutrino states have masses $m_1 \approx m_2$. This results in a deeper first dip in the flux, due to combined effect of cosmic neutrino absorption by both $\nu_{1,2}$. How this flux spectrum looks like compared to the measured flux at IceCube is shown in Fig. 3.7.

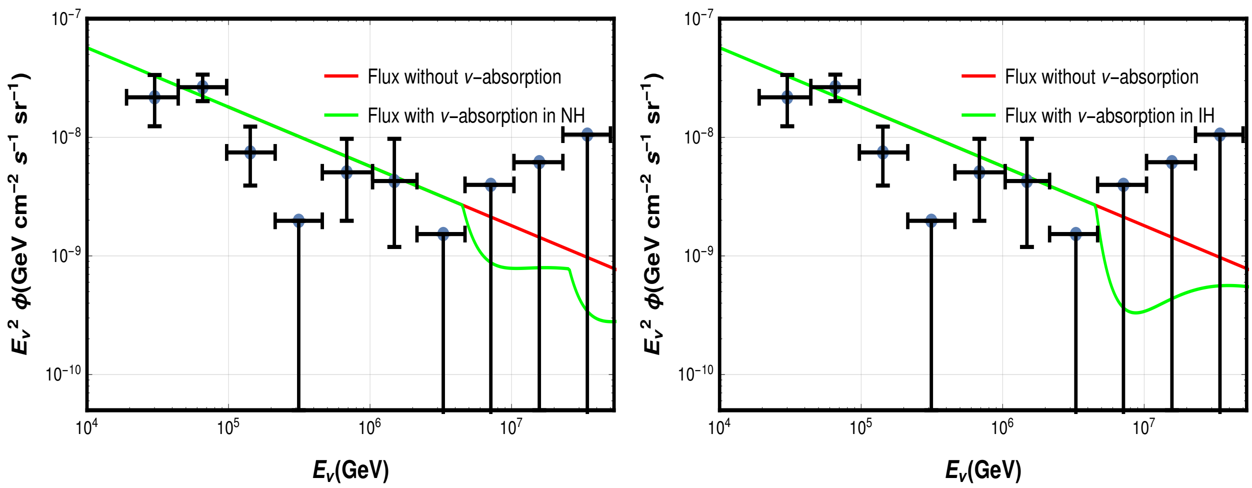

Figure 3.7: Comparison of $E_\nu^2\times$ flux for the incoming cosmic neutrinos after they got absorbed by the CνB (green) with that when there is no cosmic neutrino absorption (red) for a. normal mass hierarchy with $(m_1, m_2, m_3) = 2\times10^{-3}, 8.8\times10^{-3}, 5\times10^{-2}$ eV (left) b. inverted mass hierarchy with $(m_1, m_2, m_3) = 4.9\times10^{-2}, 5\times10^{-2}, 2\times10^{-3}$ eV (right). The data points obtained from the IceCube measurement are given in black. Yukawa couplings here are taken to be 0.1 for the representation purpose.

Effect of the t-channel resonant absorption in this model, resulting in neutrino flux suppression at particular energies of IceCube spectrum is shown in Fig. 3.8. For the benchmark points mentioned, incoming cosmic neutrinos start interacting with CνB and get absorbed only when their energy is more than 4.5 PeV. Those neutrinos therefore do not reach the IceCube detector to deposit energy or leave a track there. Suppression of incoming neutrino flux above $E_\nu \geq 4.5$ PeV that can possibly interact with the electron in the IceCube results in absence of the Glashow resonance at 6.3 PeV. Amount of neutrino flux suppression at different energies depends on the t-channel absorption cross section that peaks at an energy determined by the light scalar propagator mass (m_h) and then decreases with increasing energy. Setting $m_h \approx 10$ MeV with a cutoff at $E_\nu \geq 4.5$ PeV, fixing the CνB and N_R masses, we get maximum suppression of neutrino flux at the 11th energy bin $(6.3 - 10$ PeV) of the IceCube spectrum. As the incident neutrino energy does not entirely get deposited at the IceCube, few high energetic incident neutrino contribute to the lower energy bins. Here, also due to absence of some UHE neutrinos, event count in the nearest energy bins also get a bit suppressed. Once the t-channel maximal cross

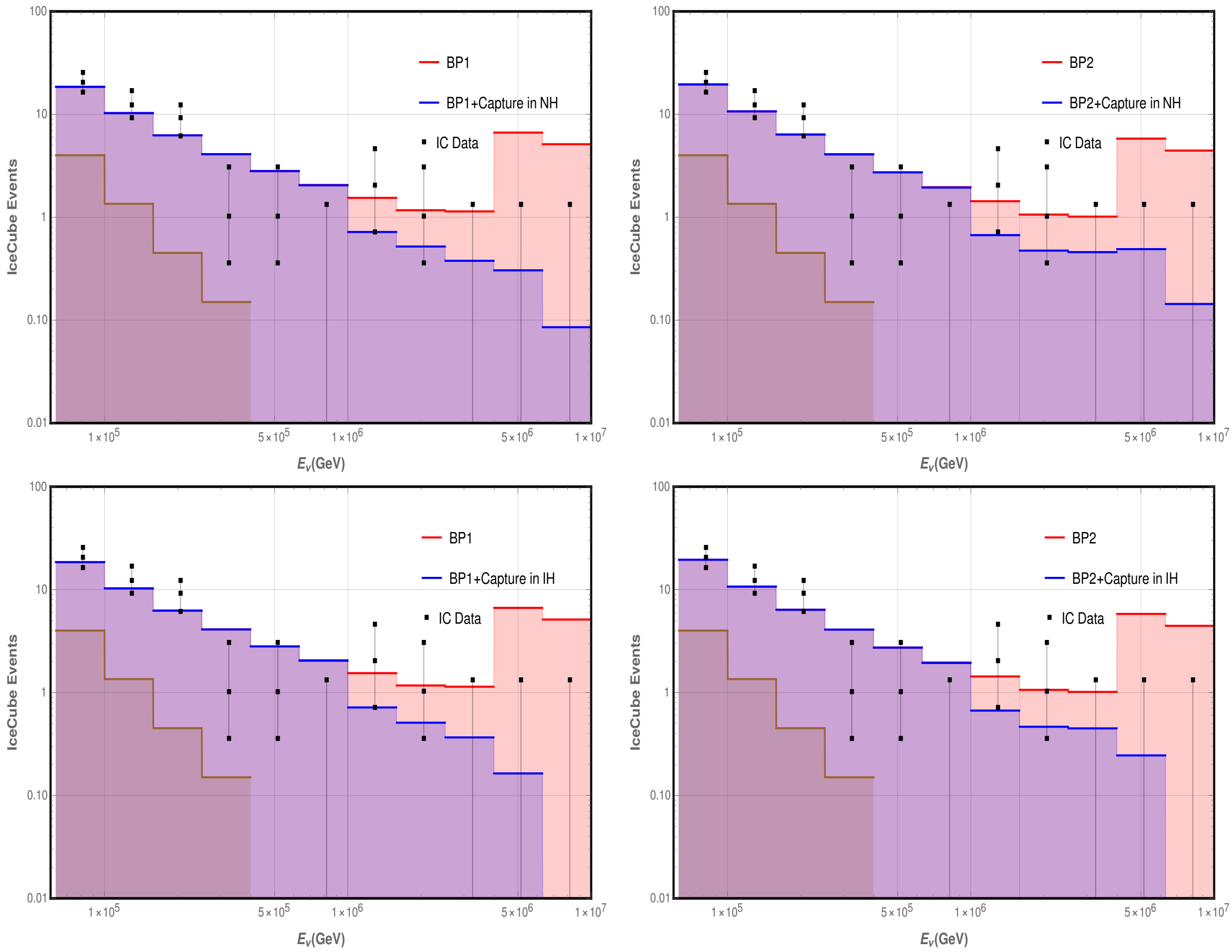

Figure 3.8: IceCube event spectrum with (violet) and without (red) neutrino capture for Benchmark Point-I (left) and Benchmark Point-II (right). Effect on the event spectrum due to neutrino absorption is shown for normal hierarchy (upper row) and inverted hierarchy (lower row). The atmospheric background is given in brown. Here we have taken $m_R = 15$ MeV and $y = 1$.

section and consequently the sharpest dip occurs in the incident neutrino spectrum, this process cross section starts decreasing with E_ν and eventually matches with the original single power law astrophysical neutrino spectrum at some higher energy. The Yukawa coupling also changes the strength of the cross section and therefore can modify the amount of suppression we can see in the IceCube spectrum. Due to the presence of a cutoff in the t-channel absorption, which we can fix at $E_\nu \sim 4.5$ PeV, this process does not affect the IceCube spectrum at lower energy bins where the we observe no neutrino event suppression as shown in Fig. 3.8. For the normal hierarchy, the heaviest neutrino mass eigenstate causes the dip at higher energy IceCube bins whereas for the inverted hierarchy two almost degenerate heavier mass eigenstates cause a sharper dip at the same energy bins.

The best fit single power law flux parametrization is $\phi_0 = 2.46 \pm 0.8 \times 10^{-18}$ and $\gamma = 2.92$ [204], which is different from our benchmark points. We quantify the goodness-of-fit for our chosen benchmark points as well as the IceCube best fit parameters by the respective χ^2 values. We find that although the fitting, in the absence of absorption, worsens for our benchmark points compared to the IceCube best fit, it improves significantly once we include the t-channel resonant absorption in the analysis. The χ^2 value for the IceCube best fit is 21.9 and the same for our benchmark points is shown in Tab. 3.1.

	BP1		BP2	
Without Absorption	49.25		38.55	
With Absorption	NH	IH	NH	IH
	7.23	7.17	6.86	6.72

Table 3.1: The goodness-of-fit for our all benchmark points is shown here. The numerical entries are the χ^2 values.

3.4 Neutrino Mass: Type-I Low Scale See-Saw

With no lepton number conservation imposed, ν2HDM allows Majorana mass generation of neutrinos with a low scale seesaw mechanism. The added three right handed neutrinos are gauge singlet Majorana neutrinos $N_{R,\beta}$, all of which transform as odd under the Z_2 symmetry. With all the SM fermions being Z_2 invariant, the Yukawa interaction in this model in the flavor basis takes the form,

$$\mathcal{L}_Y = Y^d_{\alpha\beta}\bar{Q}_{L,\alpha}\Phi_1 d_{R,\beta} + Y^u_{\alpha\beta}\bar{Q}_{L,\alpha}\tilde{\Phi}_1 u_{R,\beta} + Y^l_{\alpha\beta}\bar{L}_{L,\alpha}\Phi_1 l_{R,\beta} + Y^\nu_{\alpha\beta}\bar{L}_{L,\alpha}\tilde{\Phi}_2 N_{R,\beta} + \text{h.c.} \quad (3.22)$$

If we restrict our model to only one right handed Majorana neutrino N_R, then the relevant Yukawa and mass terms of the right handed neutrino in the mass basis of the SM neutrinos are written as,

$$\mathcal{L} = y_i \bar{L}_i \tilde{\Phi}_2 N_R + \frac{m_R}{2} N_R N_R. \quad (3.23)$$

Here the Yukawa couplings y_i are mixture of flavor basis Yukawas $Y_{\alpha\beta}$ for one particular right handed Majorana neutrino. The neutrino mass matrix takes the form:

$$M_{\nu_i} = \begin{pmatrix} 0 & \frac{y_i v_2}{\sqrt{2}} \\ \frac{y_i v_2}{\sqrt{2}} & \frac{m_R}{2} \end{pmatrix}. \tag{3.24}$$

Diagonalizing this matrix we compute Majorana neutrino mass term as:

$$\mathcal{L}_{\nu_i} = m_{\nu_i} \nu_{iL} \nu_{iL}$$

with

$$m_{\nu_i} = \frac{y_i^2 v_2^2}{m_R}. \tag{3.25}$$

With a Yukawa coupling $y_i \sim O(1)$, we get the Majorana neutrino mass of 0.1 eV for $v_2 \approx 1$ keV with right handed neutrino mass $m_R \sim 10$ MeV. This type of low scale seesaw mechanism was first proposed in the Ref. [205].

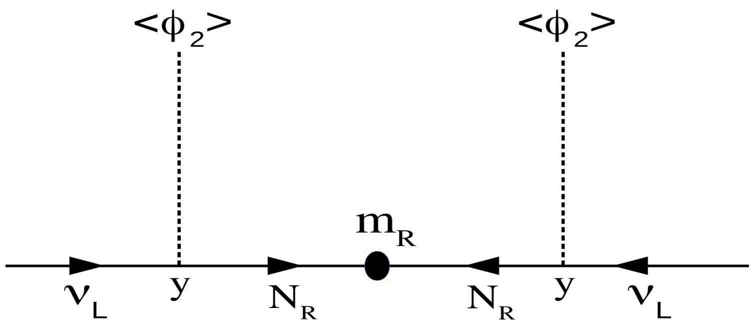

Figure 3.9: Majorana neutrino mass generation through seesaw mechanism.

3.5 Singlet Dark Matter

We extend the model of Sec. 3.2 to include a gauge singlet scalar χ which is odd under Z_2 symmetry. The scalar potential is now modified with the addition of

$$V_{DM} = \frac{1}{2} m_\chi^2 \chi^2 + \frac{\lambda_\chi}{4!} \chi^4 + \lambda \Phi_2^\dagger \Phi_2 \chi^2 \tag{3.26}$$

3.5.1 Relic Density

Based on the structure of the model explained in Sec. 3.2, DM-DM annihilation to the SM particles through SM Higgs H is kinematically suppressed because of the relatively high Higgs mass. DM can annihilate to SM fermions and neutrinos through the CP even scalar of Φ_2. The annihilation to the SM fermions (except ν_L) is suppressed due to the smallness of $\tan\beta$. As a result, the only process which contributes significantly to the relic density is the annihilation of DM into neutrinos through light mediator h as given in Fig. 3.10. The annihilation cross section for this process is given by

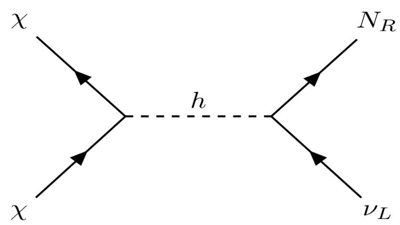

Figure 3.10: DM annihilation into neutrinos

$$\sigma(s) = \frac{\lambda^2 y^2}{8\pi s}\frac{(s-4m_\nu^2)^{3/2}}{\sqrt{s-4m_\chi^2}}\frac{1}{(s-m_h^2)^2} \tag{3.27}$$

where s is the Mandelstam variable and λ is the effective coupling shown in Fig. 3.10. The relic abundance of DM is calculated as

$$\Omega h^2 = \frac{2.14\times 10^9 GeV^{-1}}{\sqrt{g_*}M_{Pl}}\frac{1}{J(x_f)} \tag{3.28}$$

where $M_{Pl} = 1.22\times 10^{19}$ GeV is the Planck Mass, $g_* = 106.75$ is the total number of effective relativistic degrees of freedom and $J(x_f)$ is given as

$$J(x_f) = \int_{x_f}^{\infty}\frac{<\sigma v>(x)}{x^2}dx \tag{3.29}$$

and the thermal averaged cross section $<\sigma v>(x)$ is given as

$$<\sigma v>(x) = \frac{x}{8m_\chi^5 K_2^2(x)}\int_{4m_\chi^2}^{\infty}\sigma(s)\times(s-4m_\chi^2)\sqrt{s}K_1(\frac{x\sqrt{s}}{m_\chi})ds \tag{3.30}$$

where K_1, K_2 are modified Bessel functions, $x = \dfrac{m_\chi}{T}$ where T is the temperature. The x parameter corresponding to the freeze out temperature of DM is analytically given as

$$x_f = \ln\left(\frac{0.038 \mathrm{g M_{Pl} m_\chi} <\sigma \mathrm{v}> (\mathrm{x_f})}{(\mathrm{g_* x_f})^{1/2}}\right) \tag{3.31}$$

where g = internal degrees of freedom of DM particle. The relic density of DM is thus calculated by using Eq. 3.27 in Eq. 3.28 and its variation with mediator mass and DM mass is shown in Fig. 3.11.

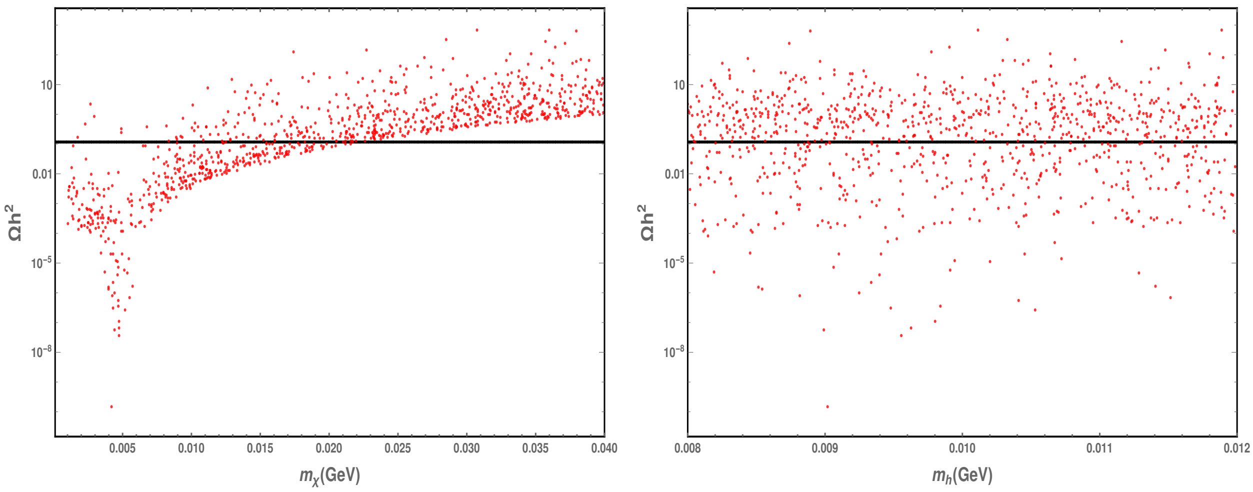

Figure 3.11: DM relic density with dark matter mass (left) and mediator mass (right). The black line shows the relic density observed by Planck.

3.5.2 Self-interaction of DM

Despite being extremely successful model for the large scale structure of the Universe, CDM model faces discrepancies at small scales such as, core-cusp problem, missing satellites problem, too-big-to-fail problem and diversity problem. A promising alternative to the CDM scenario, first proposed in [206] to solve core-cusp problem and missing satellites problem, is self interacting dark matter (SIDM). We refer the reader to [207] for a detailed review of SIDM and for the solution to the above mentioned problems in the SIDM scenario. The N-body simulations of DM self interaction [208] suggests DM to have a more Maxwellian distribution as compared to the CDM. Also the presence of self-interaction reduces the density of DM in the central region of halos which results in core [209] instead of a cusp as it is in the CDM halos [210]. As a consequence of self-interaction, SIDM halos are also negligibly elliptical as compared to the CDM halos [209]. In summary, all these can be understood just by considering the self scattering rate of DM particles,

$$R_{scat} = \frac{\sigma v_{rel} \rho_{DM}}{m_\chi} \tag{3.32}$$

where ρ_{DM} and v_{rel} respectively are the DM density and characteristic relative velocity of DM at a particular scale, with m_χ and σ being DM mass and self scattering cross section respectively. Since ρ_{DM} and v_{rel} are different at different scales, the ratio σ/m_χ

needed to explain the observations would depend on the observation scale. SIDM N-body simulations [211] predict $\sigma/m_\chi \sim 1cm^2/g$ on galaxy scales and $\sigma/m_\chi \sim 0.1cm^2/g$ on cluster scales.

In our model we allow $2 \to 2$ elastic self scattering of DM particles, which allows the deviations from the CDM predictions. The $2 \to 2$ DM scattering takes place through h and there is also a 4-point scattering of DM particles. The interaction diagrams are shown in Fig. 3.12. The ratio σ/m_χ is given as

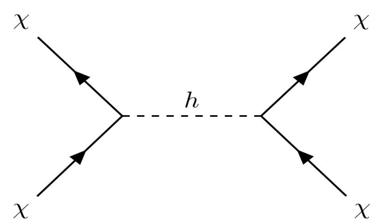

Figure 3.12: Self interaction of dark matter

$$\sigma = \frac{1}{64\pi m_\chi^2}\left[\lambda_\chi - \frac{(\lambda v_2)^2}{(4m_\chi^2 - m_h^2)}\right]^2 \tag{3.33}$$

The σ/m_χ constraint will be satisfied in this model for allowed parameter space of λ,m_h and m_χ, varying the free parameter λ_χ.

3.6 Discussion and Conclusion

A single power law flux of cosmic ray neutrinos cannot fit the event spectrum observed by the IceCube neutrino observatory. The cross section of the Glashow resonance process $\bar{\nu}_e e^-$ is larger than the neutrino nucleon interaction at energy around 6.3 PeV. Therefore, a dramatic increase in the number of events at this energy is expected, however IceCube has not seen any events at this energy until now. In this chapter, we discussed a phenomenon that can explain the absence of Glashow resonance at IceCube neutrino detector. We discussed a scenario where cosmic ray neutrinos are absorbed by cosmic neutrino background, therefore causing multiple dips in the cosmic ray neutrino flux, which correspond to three different neutrino mass eigenstates present in cosmic neutrino background.

We use ν2HDM which, in addition to SM fields, contains a second Higgs and 3 right-handed neutrinos. This model allows us to have a t-channel process in which a cosmic ray neutrino interacts with the cosmic neutrino background neutrino. The vev of the second Higgs is so chosen that the mixing between the two Higgs is very small.

The occurance of the dip in the flux due to CRν-CνB interaction is set by the condition $m_\nu E_\nu = m_h^2$ and strength of the dip depends on the Yukawa coupling y_i whereas the position of the dip depends on the mass of the right-handed neutrinos. However, due to different mass splittings, position and depth of the dips are different in normal and inverted mass hierarchies. Hence, the occurrence of dips in the neutrino flux is tuned to the energy of the expected GR events, explaining their absence at the IceCube. To obtain a appropriate dip at the Glashow bins (5-10 PeV) in the IceCube event specturm we chose $m_h \sim 10$ MeV, $m_R \sim 10$ MeV and $y_i \sim 1$. The same values for m_R and y_i with $v_2 \sim 1$ keV are used to obtain the O(0.1)eV Majorana neutrino mass through a very low scale type I seesaw mechanism. We next extended the ν2HDM with a siglet scalar dark matter χ which, having the same Z_2 charge as Φ_2, couples only to second Higgs. We find that the same value for the mass of second Higgs ($m_h = 10$ MeV) that generates suitable dips at the Glashow bins also mediates the DM annihilation to ν_L-N_R pair to give the correct relic density and DM self interaction.

The t-channel neutrino absorption phenomenon can be altered to fit presence of few events in the high energy bins as indicated by more recent IceCube results with nine year data [212].

Chapter 4

Cosmological Tensions and Dark Energy Models

The main conceptual problem with ΛCDM model is that there is no explanation of the origin and the unusually small value of the cosmological constant (Λ). One popular class of models which addresses this is the $f(R)$ gravity [213] models, in which the cosmological constant is generated dynamically from the curvature. The Hu-Sawicki $f(R)$ gravity model is one such model which gives explanation for coincidence problem and also satisfies the constraints from solar system tests [213]. One may also take a phenomenological approach of generalizing the cosmological constant to a dynamical variable and determine from observation how it changes in time. An example of this is the DDE model which also avoids the problem of phantom crossing. For earlier works on cosmological parameter estimation with DDE models and $f(R)$ gravity models see [214–216].

In this chapter we constrain the cosmological parameters in HS Model and DDE model. We primarily focus on H_0 and σ_8 tension between Planck data and LSS data. In Hu-Sawicki model, we find that the tension in σ_8 between Planck-CMB and LSS observations worsens in the HS model compared to the ΛCDM model. Whereas in DDE model the σ_8 tension is eased as compared to ΛCDM model. Interestingly, in both the models the H_0 is relieved just by adding a massive neutrinos in the picture, a result earlier obtained within the premises of ΛCDM model [52]. We also provide bounds on neutrino masses in both these models.

In Sec. 4.1 we briefly discuss the Hu-Sawicki $f(R)$ model and the modification in the evolution equations. In Sec. 4.2 we describe the phenomenological parametrization of DDE model. We describe the role of massive neutrinos in cosmology and their evolution equations in Sec. 4.3. In Sec. 4.4 matter power spectrum and it's relation to σ_8 has been discussed briefly. We also explain the effect of HS, DDE model parameters and massive neutrinos on the matter power spectrum in this section. The data sets used and analyses done is summarized in Sec. 4.5. We conclude with discussion in Sec. 4.6.

4.1 f(R) Theory

Scalar-tensor theories are generalized Brans-Dicke [217] theories described by the general action

$$\begin{aligned} S_{\text{st}} = \int d^4x\sqrt{-\tilde{g}}\Big(\frac{\tilde{R}}{16\pi G} - \frac{1}{2}\tilde{g}^{\mu\nu}\partial_\mu\phi\partial_\nu\phi - V(\phi)\Big) \\ + S_m(g_{\mu\nu},\psi), \end{aligned} \tag{4.1}$$

where $S_m(g_{\mu\nu},\psi)$ is the action for the matter fields, $g_{\mu\nu}$ is Jordan frame metric and $\tilde{g}_{\mu\nu}$ is Einstein frame metric which are related by the conformal transformation $g_{\mu\nu} = A^2(\phi)\tilde{g}_{\mu\nu}$, and ϕ is the scalar field which couples to Einstein metric as well as to matter fields ψ. Due to the presence of the scalar field the force of gravitation on a test particle in a gravitational field gets modified to

$$\vec{F} = -\vec{\nabla}\Psi - \frac{d\ln A(\phi)}{d\phi}\vec{\nabla}\phi\ , \tag{4.2}$$

and therefore the dynamics is governed by an effective potential

$$V_{\text{eff}}(\phi) = V(\phi) + (A(\phi) - 1)\rho, \tag{4.3}$$

where Ψ is Newtonian potential and ρ is density.

The interaction between the scalar field and the matter field would violate the Einstein Equivalence Principle [218] and signatures of this coupling would appear in non-gravitational experiments based on universality of free fall and local Lorentz symmetry [219] in the matter sector. These experiments put severe constraints on the presence of a scalar field which can be satisfied either by making the coupling of the scalar field with the matter field very small or by completely hiding the interaction through some mechanism. One such mechanism is called chameleon mechanism [220] in which $V(\phi)$

and $A(\phi)$ are chosen in such forms that $V_{eff}(\phi)$ has density dependent minimum, i.e., $V_{eff}(\phi)_{min} = V_{eff}(\phi(\rho))$. The required screening is achieved if either the coupling is very small at the minimum of $V_{eff}(\phi)$ or the mass of the scalar field is extremely large. If the scalar field stays at its density dependent minimum, $\phi(\rho)$, the theory can be parametrized into two functions, the mass function $m(\rho)$ and the coupling $\beta(\rho)$ at the minimum of the potential [221, 222]

$$\frac{\phi(\rho) - \phi_c}{m_{\rm Pl}} = \frac{1}{m_{\rm Pl}^2} \int_\rho^{\rho_c} d\rho \frac{\beta(\rho)}{m^2(\rho)}, \tag{4.4}$$

where $m_{\rm Pl}$ is the Planck mass. The mass of the scalar field $m(\rho)$ and the coupling parameter $\beta(\rho)$ are respectively given as

$$m^2(\rho) = \frac{d^2 V_{\rm eff}}{d\phi^2}|_{\phi=\phi(\rho)} \tag{4.5}$$

$$\beta(\rho) = m_{\rm Pl} \frac{d \ln A}{d\phi}|_{\phi=\phi(\rho)}. \tag{4.6}$$

Simplest modified gravity model is the $f(R)$ gravity [31, 32, 223] in which the Lagrangian density is promoted to a non linear functions of R from just R in GR. The general action for an $f(R)$ theory is given as

$$S = \frac{1}{16\pi G} \int d^4x \sqrt{-g} \left(f(R)\right) + S_m(g_{\mu\nu}, \psi). \tag{4.7}$$

The scalar degree of freedom in the $f(R)$ theories has been utilized as the quintessence field to explain DE. It has been shown [223, 224] that $f(R)$ theory is the equivalent to a scalar-tensor theory with an equivalence relation

$$f_R = e^{-2\beta_0 \phi_R / m_{\rm Pl}}, \tag{4.8}$$

and potential corresponding to extra scalar degree of freedom

$$V(\phi_R) = \frac{m_{\rm Pl}^2}{2} \frac{R f_R - f(R)}{f_R^2}, \tag{4.9}$$

where $f_R = \partial f / \partial R$.

4.1.1 Hu-Sawicki Model

The model that we choose for this purpose is the popular Hu-Sawicki $f(R)$ gravity, that was introduced in [213] and represents one of the few known viable functional forms of

$f(R)$ that evade the constraints from solar system tests of gravity. Cosmological scenarios such as non-linear structure formation via N-body simulation and astrophysical scenarios such as of this model are studied in [225–229]. In HS model the modification in the action is given as

$$f(R) = R - 2\Lambda - \frac{f_{R_0}}{n}\frac{R_0^{n+1}}{R^n}, \tag{4.10}$$

where $R \geq R_0$ and R_0 is the curvature at present. Here f_{R_0} and n are the free parameters of the HS model. Using equivalence relation Eq. 4.8 and Eq. 4.9, we find that

$$V(\phi_R) = \Lambda + \frac{n+1}{n} f_{R_0} R_0 \left(\frac{-2\beta_0\phi_R}{m_{\mathrm{Pl}} f_{R_0}}\right)^{n/(n+1)} \tag{4.11}$$

The coupling function $\beta(a)$ is constant for all the $f(R)$ models *i.e* $\beta(a) = \dfrac{1}{\sqrt{6}}$, whereas the mass function $m(a)$ is a model dependent quantity [221, 222, 230]. In particular for the HS model, for which form of $f(R)$ is given by Eq. 4.10, we have mass function

$$m(a) = m_0 \left(\frac{4\Omega_\Lambda + \Omega_m a^{-3}}{4\Omega_\Lambda + \Omega_m}\right)^{(n+2)/2}, \tag{4.12}$$

with

$$m_0 = H_0 \sqrt{\frac{4\Omega_\Lambda + \Omega_m}{(n+1) f_{R_0}}}, \tag{4.13}$$

These parameters contains all the information of the model, where Ω_Λ and Ω_m are the matter density fraction for dark energy and matter today. In the next subsection, we will derive the evolution equations in terms of these parameters.

4.1.2 Evolution Equations

In ΛCDM model based on GR the evolution of metric perturbation potentials and density perturbations is given by the following linearized equations,

$$k^2\Phi = -4\pi G a^2 \rho\delta \tag{4.14}$$

$$k^2(\Phi - \Psi) = 12\pi G a^2 (\rho + P)\sigma, \tag{4.15}$$

$$\delta'' + \mathcal{H}\delta' - 4\pi G a^2 \rho\delta = 0 \tag{4.16}$$

Where $'$ denotes the derivative with respect to the conformal time, δ is the co-moving density contrast and Φ and Ψ are the space-time dependent perturbations parametrized into the FRW metric,

$$ds^2 = -(1 + 2\Phi)dt^2 + a^2(t)(1 - 2\Psi)\delta_{ij}dx^i dx^j. \tag{4.17}$$

In models other than the ΛCDM model the evolution equations be different form. This change is parametrized in several ways in the literature [231–235]. In this chapter, we use the parametrization introduced in [231], which changes the evolution equations to

$$k^2\Psi = -4\pi G a^2 \mu(k, a)\rho\delta \tag{4.18}$$

$$\frac{\Phi}{\Psi} = \gamma(k, a), \tag{4.19}$$

where $\mu(k, a)$ and $\gamma(k, a)$ are two scale and time dependent functions introduced to incorporate any modified theory of gravity. Note the appearance of Ψ instead of Φ in the first equation. In the quasi-static approximation $\mu(k, a)$ and $\gamma(k, a)$ can be expressed as [221]

$$\mu(k, a) = A^2(\phi)(1 + \epsilon(k, a)), \tag{4.20}$$

$$\gamma(k, a) = \frac{1 - \epsilon(k, a)}{1 + \epsilon(k, a)}, \tag{4.21}$$

where

$$\epsilon(k, a) = \frac{2\beta^2(a)}{1 + m^2(a)\frac{a^2}{k^2}}. \tag{4.22}$$

Modification in the evolution of Ψ and Φ in turn modifies the evolution of matter perturbation as

$$\delta'' + \mathcal{H}\delta' - \frac{3}{2}\Omega_m \mathcal{H}^2 \mu(k, a)\delta = 0 \tag{4.23}$$

where $\mathcal{H} = a'/a$.

4.2 Dynamical Dark Energy Model

The current measurements of cosmic expansion [236–238], indicate that the present Universe is dominated by dark energy (DE). The most common dark energy candidate is cosmological constant Λ representing a constant energy density occupying the space homogeneously. The equation of state parameter for DE in cosmological constant model is $w_{DE} = \dfrac{P_{DE}}{\rho_{DE}} = -1$. However a constant Λ makes the near coincidence of Ω_Λ and Ω_m in the present epoch hard to explain naturally. This gives way for other models of

DE such as quintessence [239–241], interacting dark energy [242] and phenomenological parametrization of DE as in DDE models. The DDE models provide generalizations of ΛCDM cosmology to consider a time dependent equation of state parameter of the underlying dark energy fluid, which eventually gives extra parameters to reconstruct a cosmological history better fitting to the observed data. There are several parameterizations of the DDE approach available in the literature, see [243–254] and the references therein. In general, the phenomenological DE equation of state parameter is taken to be a variable, dependent on the scale factor (equivalently time or redshift),i.e.,

$$w_{\rm DE}(z) = \sum_n w_n x(z), \tag{4.24}$$

where w_n are parameters fixed by observations and $x(z)$ is function of redshift. The most commonly followed $w(z)$ dependence are phantom fields($w(z) < -1$) and non phantom field($-1 \leq w(z) \leq 1$). Energy density of each component of the Universe follows the continuity equation

$$\dot{\rho}_i = 3H(p_i + \rho_i) \tag{4.25}$$

where p_i and ρ_i are pressure and density of the species i, related by $p_i = w_i \rho_i$. Now for a DDE with $w_i = w_{\rm DE}(z)$, the solution of Eq. 4.25 gives

$$\rho_{\rm DE}(z) = \rho_{\rm DE,0}(1+z)^3 \exp\left(-3\int_0^z w_{\rm DE}(z)dz\right) \tag{4.26}$$

The above equation gives the evolution of DE in the DDE model parameterized by $w_{\rm DE}(z)$.

For our comparative analyses we use the Chavallier-Polarski-Linder (CPL) [243, 244] parametrization of DDE in this chapter. The equation of state parameter for DE in CPL parametrization is

$$w_{\rm DE}(z) = w_0 + w_a \frac{z}{z+1}, \tag{4.27}$$

where w_0 and w_a are the CPL parameters. This parametrization describes a non phantom field when $w_a + w_0 \geq -1$ and $w_0 \geq -1$. Choosing $w_0 = -1$ and $w_a = 0$, Eq. 4.27 gives back the ΛCDM model. As a result of this parametrization the evolution of DE density, Eq. 4.26, scaled by the critical density, gives the evolution of the DE density fraction as

$$\Omega_{\rm DE}(z) = \Omega_{\rm DE,0}(1+z)^{3(1+w_o+w_a)} e^{-3w_a \frac{z}{z+1}}, \tag{4.28}$$

where $\Omega_{\rm DE,0}$ is the DE density at present.

4.3 Massive Neutrino in Cosmology

Neutrinos play an important role in the evolution of the Universe. Neutrinos being massive can affect the background as well as matter perturbation which in-turn can leave its imprint on cosmological observations. In the early Universe, neutrinos are relativistic and interact weakly with other particles. As the temperature of the Universe decreases, the weak interaction rate becomes less than the Hubble expansion rate of the Universe and neutrinos decouple from rest of the plasma. Since neutrinos are relativistic, their energy density after decoupling is given [255, 256]

$$\rho_\nu = \left[\frac{7}{8}\left(\frac{4}{11}\right)^{4/3} N_{\text{eff}}\right]\rho_\gamma\,, \tag{4.29}$$

where ρ_γ is the photon energy density. N_{eff} is the effective number of relativistic neutrinos at early times which is theoretically predicted to be 3.045 [257] and estimated from CMB observation to be 2.99 ± 0.17 [128]. When the temperature of the Universe goes below the mass of the neutrinos, they turn into non-relativistic particles.The energy density fraction of neutrinos in the present Universe depends on the sum of their masses and is given as

$$\Omega_\nu = \frac{\sum m_\nu}{\text{eV}}\frac{1}{93.1h^2}\,, \tag{4.30}$$

where $\sum m_\nu$ is the sum of neutrino masses. Neutrinos in the present Universe contribute a very small fraction of energy density however they can affect the formation of structure at large scales.

After neutrinos decouple, they behave as collisionless fluid with individual particles streaming freely. The free streaming length is equal to the Hubble radius for the relativistic neutrinos, whereas non-relativistic neutrinos stream freely on the scales $k > k_{\text{fs}}$, where k_{fs} is the neutrino free-streaming scale. On the scales $k > k_{\text{fs}}$, the free-streaming of the neutrinos damp the neutrino density fluctuations and suppress the power in the matter power spectrum. On the other hand neutrinos behave like cold dark matter perturbations on the scales $k < k_{\text{fs}}$. [255, 256]

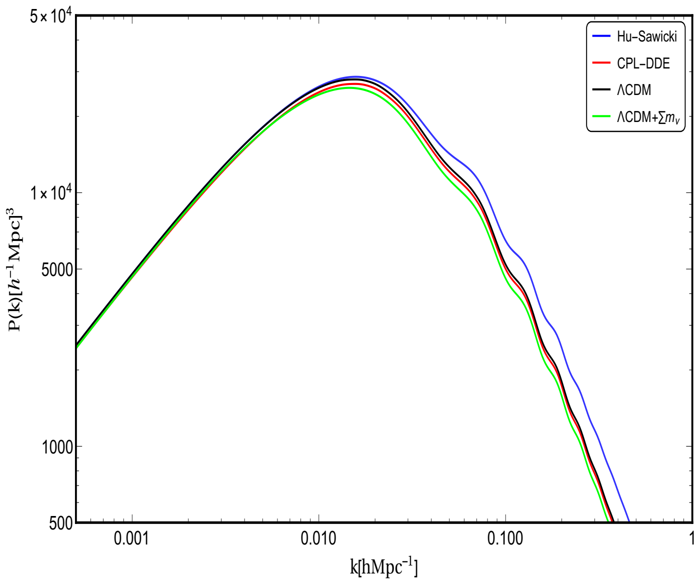

Figure 4.1: Matter power spectrum in HS, DDE and ΛCDM model.

4.3.1 Evolution Equations for Massive Neutrinos

Decoupled massive neutrinos obey the collision-less Boltzmann equation, therefore we solve the Boltzmann equation for the neutrinos to get their evolution equations. The energy momentum tensor for neutrinos is given as

$$T_{\mu\nu} = \int dP_1 dP_2 dP_3 (-g)^{-1/2} \frac{P_\mu P\nu}{P^0} f(x^i, P_j, \tau)\,, \tag{4.31}$$

where $f(x^i, P_j, \tau)$ and P_μ are the distribution function and the four momentum of neutrinos respectively. We expand the distribution function around the zeroth-order distribution function f_0 as

$$f(x^i, P_j, \tau) = f_0(q)[1 + \chi(x^i, P_j, \tau)], \tag{4.32}$$

where χ is the perturbation in the distribution function. Using Eq. 4.31 in Eq. 4.32 and equating the zeroth order terms, we get the unperturbed energy density and pressure for neutrinos

$$\bar{\rho} = 4\pi\, a^{-4} \int q^2 dq \epsilon f_0(q), \quad \bar{P} = \frac{4\pi a^{-4}}{3} \int q^2 dq \frac{q^2}{\epsilon} f_0(q). \tag{4.33}$$

Similarly, We get the perturbed quantities by equating the first order terms

$$\begin{aligned}
\delta\rho &= 4\pi\, a^{-4}\int q^2 dq \epsilon f_0(q)\chi, \\
\delta P &= \frac{4\pi a^{-4}}{3}\int q^2 dq \frac{q^2}{\epsilon} f_0(q)\chi. \\
\delta T^0_i &= 4\pi\, a^{-4}\int q^2 dq q n_i f_0(q)\chi, \\
\delta\Sigma^i_j &= \frac{4\pi a^{-4}}{3}\int q^2 dq \frac{q^2}{\epsilon}(n_i n_j - \frac{1}{3}\delta_{ij}) f_0(q)\chi,
\end{aligned} \tag{4.34}$$

where $q_i = qn_i$ is the co-moving momentum and $\epsilon = \epsilon(q,\tau) = \sqrt{q^2 + m_\nu^2 a^2}$. It is clear from Eq. 4.34 that we can not simply integrate out the q dependence as ϵ is the function of both τ and q. Hence, we will use the Legendre series expansion of the perturbation χ to get the perturbed evolution equations for the massive neutrino. Legendre series expansion of the perturbation χ is given as

$$\chi(\vec{k},\hat{n},q,\tau) = \sum_{l=0}^{\infty}(-i)^l(2l+1)\,\chi_l(\vec{k},q,\tau)P_l(\hat{k}.\hat{n})\,, \tag{4.35}$$

where $P_l(\hat{k}.\hat{n})$ are the Legendre polynomials. Using Eq. 4.35 in the Eq. 4.34, we get the perturbed evolution equations for the massive neutrino [258]

$$\begin{aligned}
\delta\rho_h &= 4\pi a^{-4}\int q^2 dq \epsilon f_0(q)\chi_0\,, \\
\delta P_h &= \frac{4\pi}{3}a^{-4}\int q^2 dq \frac{q^2}{\epsilon} f_0(q)\chi_0\,, \\
(\bar{\rho}_h + \bar{P}_h)\theta_h &= 4\pi k a^{-4}\int q^2 dq q f_0(q)\chi_1\,, \\
(\bar{\rho}_h + \bar{P}_h)\sigma_h &= \frac{8\pi}{3}a^{-4}\int q^2 dq \frac{q^2}{\epsilon} f_0(q)\chi_2\,,
\end{aligned} \tag{4.36}$$

where the Boltzmann equation governs the evolution of χ_l. In the Newtonian gauge Boltzmann equations for χ_l are given as

$$\begin{aligned}
\dot{\chi}_0 &= -\frac{qk}{\epsilon}\chi_1 - \dot{\Phi}\frac{d\ln f_0}{d\ln q}\,, \\
\dot{\chi}_1 &= \frac{qk}{3\epsilon}(\chi_0 - 2\chi_2) - \frac{\epsilon k}{3q}\Psi\frac{d\ln f_0}{d\ln q}\,, \\
\dot{\chi}_l &= \frac{qk}{(2l+1)\epsilon}[l\chi_{l-1} - (l+1)\chi_{l+1}]\,, \qquad \text{for, } l \geq 2.
\end{aligned} \tag{4.37}$$

4.4 Matter Power Spectrum and σ_8

In this section we discuss the effect of massive neutrinos, HS model parameters and DDE model parameters on the matter power spectrum and σ_8. Matter power spectrum is a scale dependent quantity defined as the two-point correlation function of matter density, $P(k) = k^{n_s}T^2(k)D^2(a)$. Where $T(k)$ is the matter transfer function, $D(a)$ is the linear growth factor and n_s is the tilt of the primordial power spectrum. Also, the r.m.s. fluctuation of density perturbations in a sphere of radius r is defined as

$$\sigma(r,z) = \left[\frac{1}{2\pi^2}\int_0^\infty dk k^2 P(k,z)|W(kr)|^2\right]^{1/2}, \tag{4.38}$$

where r is related to mass by $r = (3M/4\pi\rho_m(z=0))^{1/3}$ with $\rho_m(z=0)$ being the matter density of the Universe at present epoch. Here $W(kr) = 3(\sin kr - kr\cos kr)/(kr)^3$ is the filter function. This is a scale dependent quantity. The r.m.s. fluctuation of density perturbations on scale 8 h^{-1}Mpc is called $\sigma_8(z)$.

We use CAMB [259] to generate the matter power spectrum for DDE model, whereas we use MGCAMB [231, 232] to obtain the matter power spectrum for HS model. In order to see the effect of modified gravity models and massive neutrinos we plot matter power spectrum for some benchmark values of $\sum m_\nu$, HS model parameters and DDE model parameters. The power spectra are shown in Fig. 4.1.

- As we discussed in Sec. 4.3, massive neutrinos stream freely on the scales $k > k_{\rm fs}$ and they can escape out of the high density regions on those scales. The perturbations on length scales smaller than neutrino free streaming length will be washed out and therefore power spectrum gets suppressed on these scales. Neutrino mass cuts the power at length scales even larger than the 8 h^{-1}Mpc which requires a large Ω_m which in turn disfavors the compatibility of $\sigma_8 - \Omega_m$ between the two observations.

- DDE cuts the power spectrum at all length scales. Since, in the DDE model, dark energy density increases with the redshift, therefore, in the early time when the dark energy density is large, the power cut is more prominent at small scales.

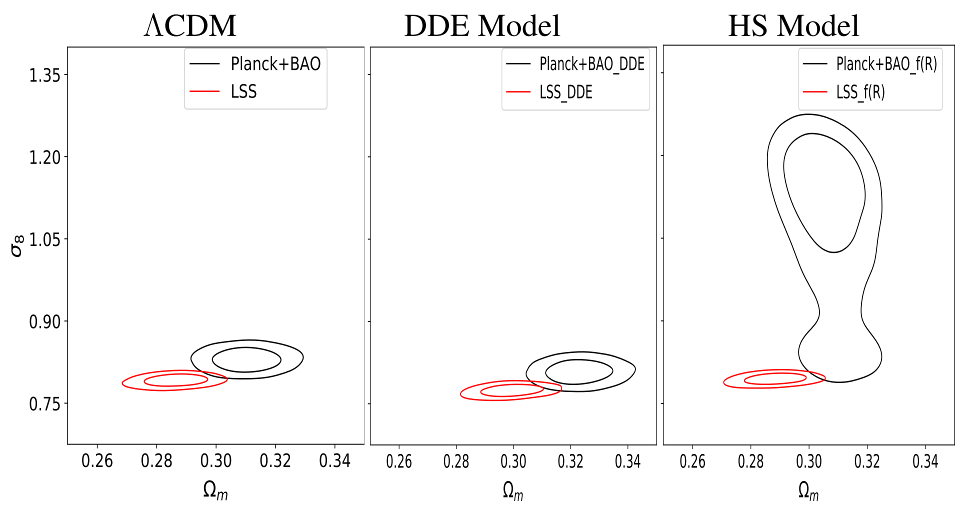

Figure 4.2: The 1-σ and 2-σ contours in $\sigma_8 - \Omega_m$ parameter space for ΛCDM, DDE and HS model with $\sum m_\nu = 0.06$eV are shown here. It is shown that the σ_8 discrepancy worsens in the HS model whereas in DDE model the descrepancy is somewhat relieved.

- On the other hand, the power spectrum gets affected in an opposite manner for HS model as the power increases slightly on small length scales.

4.5 Datasets and Analysis

As discussed in Sec. 2.4 there is a discrepancy in the values of H_0 and σ_8 reported by the large scale surveys and Planck CMB observations. In this section we examine these tensions through a comparative analysis of three cosmological models, namely ΛCDM, HS and DDE model. For analyzing these models, we use Planck CMB observations [96] for temperature anisotropy power spectrum over the multipole range $\ell \sim 2-2500$ and Planck CMB polarization data for low ℓ only. We refer to these data sets combined as Planck data. We also use the baryon acoustic oscillations(BAO) data from 6dF Galaxy Survey [146], BOSS DR11 [98, 147] and SDSS DR7 Main Galaxy Sample [100]. In addition we use the cluster count data from Planck SZ survey [148], lensing data from Canada France Hawaii Telescope Lensing Survey (CFHTLens) [149, 150] and CMB lensing data from Planck lensing survey [151] and South Pole Telescope (SPT) [152, 153]. We also use the data for Redshift space distortions (RSD) from BOSS DR11 RSD measurements [154]. We combine Planck SZ data, CFHTLens data, Planck lensing data, SPT lensing data and

RSD data and refer them as LSS data. We perform Markov Chain Monte Carlo (MCMC) analysis for ΛCDM, HS and DDE model with both Planck+BAO and LSS data. We use CosmoMC [260] to perform the MCMC analysis for ΛCDM and DDE model and add MGCosmoMC patch [231, 232] to it for HS model. MGCosmoMC patch includes the $\mu(k, a)$ and $\gamma(k, a)$ parametrization discussed in Sec. 4.1.

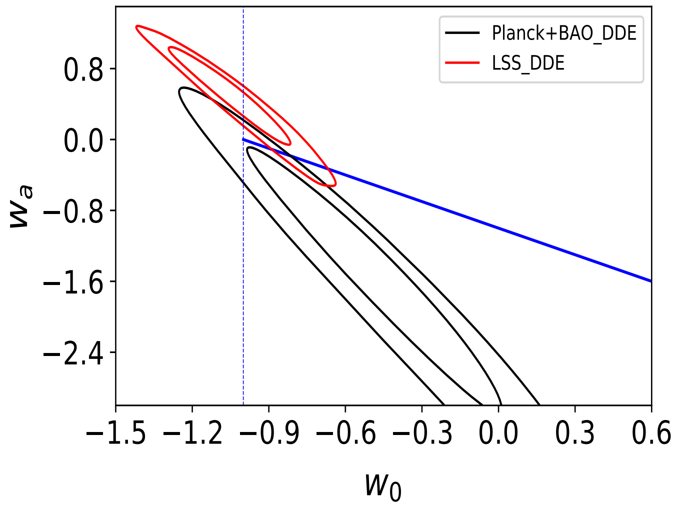

Figure 4.3: Parameter space for w_0 and w_a allowed by Planck+BAO and LSS data. Blue and Blue dashed lines correspond to $w_0+w_a = -1$ and $w_0 = -1$ respectively. The region above these lines is the non-phantom region.

In our analysis for ΛCDM model we have total six free parameter which are standard cosmological parameters namely, density parameters for cold dark matter (CDM) Ω_c and baryonic matter Ω_b, optical depth to re-ionization τ_{reio}, angular acoustic scale Θ_{MC}, amplitude A_s and tilt n_s of the primordial power spectrum. We fix $\sum m_\nu = 0.06$eV to satisfy the neutrino oscillation experiments results. We also have two derived parameters H_0 and σ_8. First we perform MCMC analysis with Planck+BAO data with these parameters and get constraints for each parameter. Next, we run the MCMC analysis with LSS data for ΛCDM model. Since τ_{reio} does not affects the LSS observation therefore we also use the best fit value of $\tau_{reio} = 0.08$, obtained from analyses with Planck+BAO data, as fixed prior. We have listed all the parameters with flat in Tab. 4.1. These analyses give $\sigma_8 = 0.829 \pm 0.015$ for the Planck+BAO data and $\sigma_8 = 0.7917 \pm 0.0074$ and for LSS data.

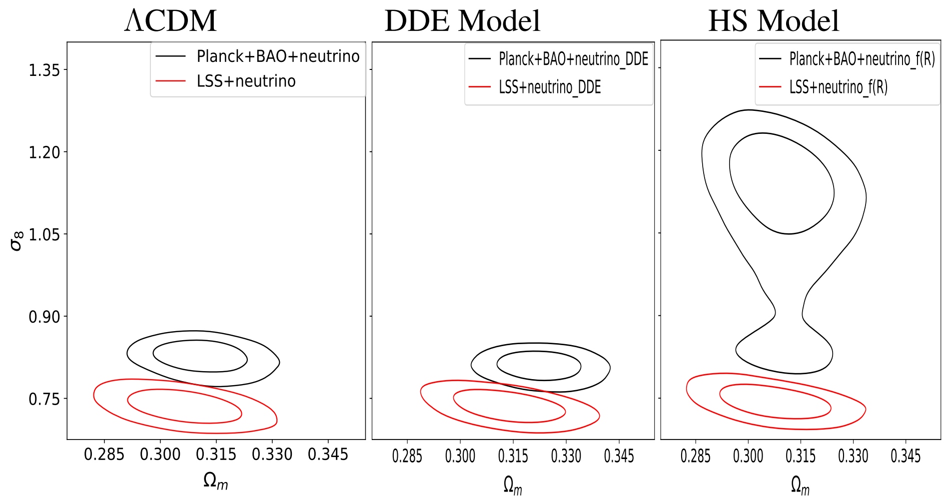

Figure 4.4: The 1-σ and 2-σ contours in $\sigma_8 - \Omega_m$ parameter space for ΛCDM, DDE and HS model with varying $\sum m_\nu$ are shown here. It is shown that the σ_8 discrepancy worsens in the HS model whereas in DDE model the descrepancy is somewhat relieved.

Parameters	Planck+BAO	LSS
$\Omega_c h^2$	[0.001, 0.99]	[0.001, 0.99]
$\Omega_b h^2$	[0.005, 0.1]	[0.005, 0.1]
τ_{reio}	[0.01, 0.8]	
$100\Theta_{\rm MC}$	[0.5, 10]	[0.5, 10]
$\ln(10^{10}A_s)$	[2, 4]	[2, 4]
n_s	[0.8, 1.2]	[0.8, 1.2]
$\sum M_\nu$	[0, 5.0]	[0, 5.0]
$\log_{10} f_{R_0}$	[-9.0,10]	[-9.0,10]

Table 4.1: Parameters with flat prios are listed in this table.

We plot the parameter space $\sigma_8 - \Omega_m$, obtained from two different analysis (Fig. 4.2). It is clear from the Fig. 4.2 that there is a mismatch between the values of σ_8 inferred from Planck+BAO data and that from LSS data.

In our analysis for HS model we have eight free parameter of which six are standard cosmological parameters, two are HS model parameters namely, f_{R_0} and n as defined in Sec. 4.1. Here we fix $n = 1$ and allowed f_{R_0} to vary in the range [10^{-9},10]. We repeat

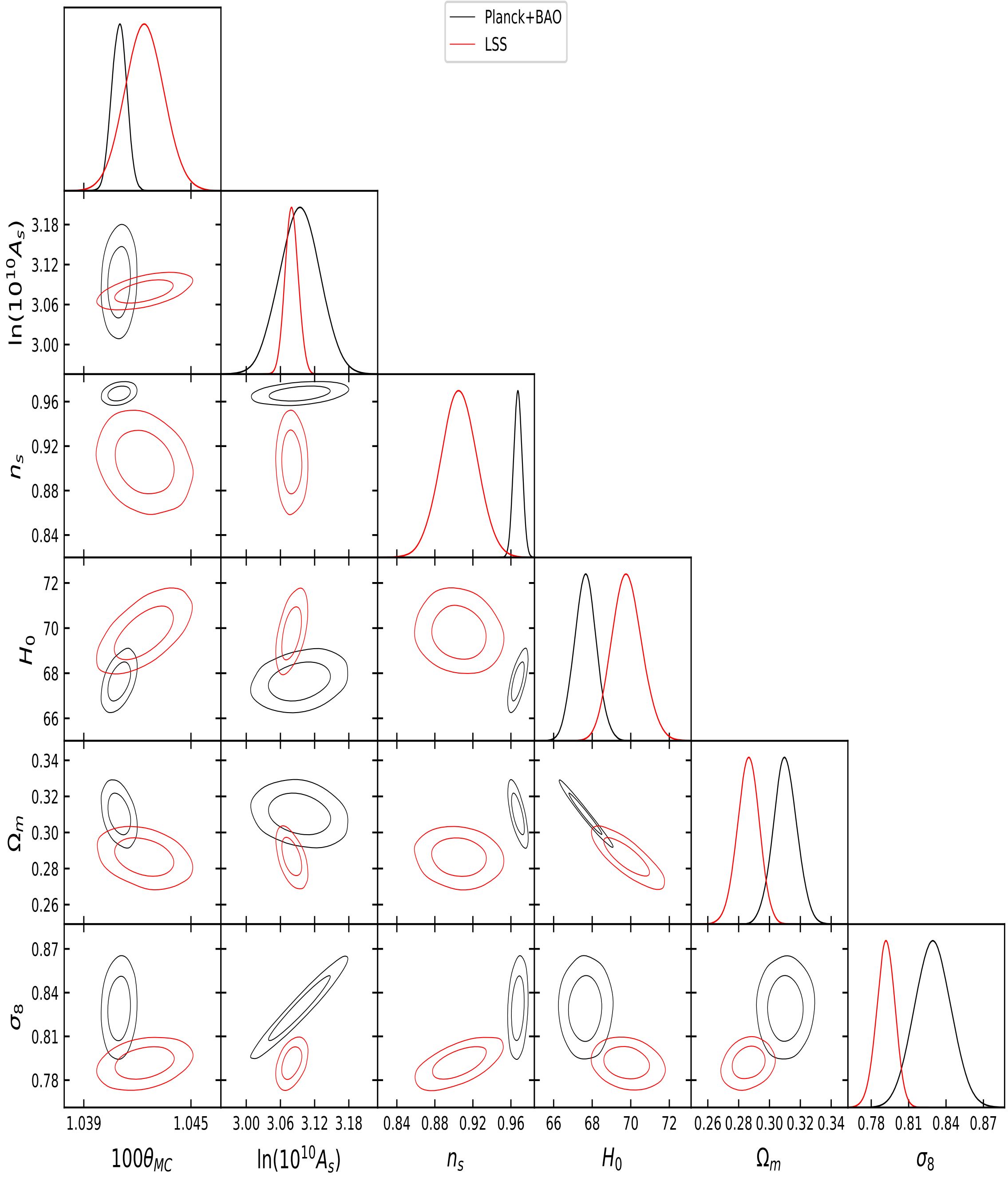

Figure 4.5: The triangle plot showing 1-σ and 2-σ contours of all the parameters for ΛCDM model with $\sum m_\nu = 0.06$eV is shown here.

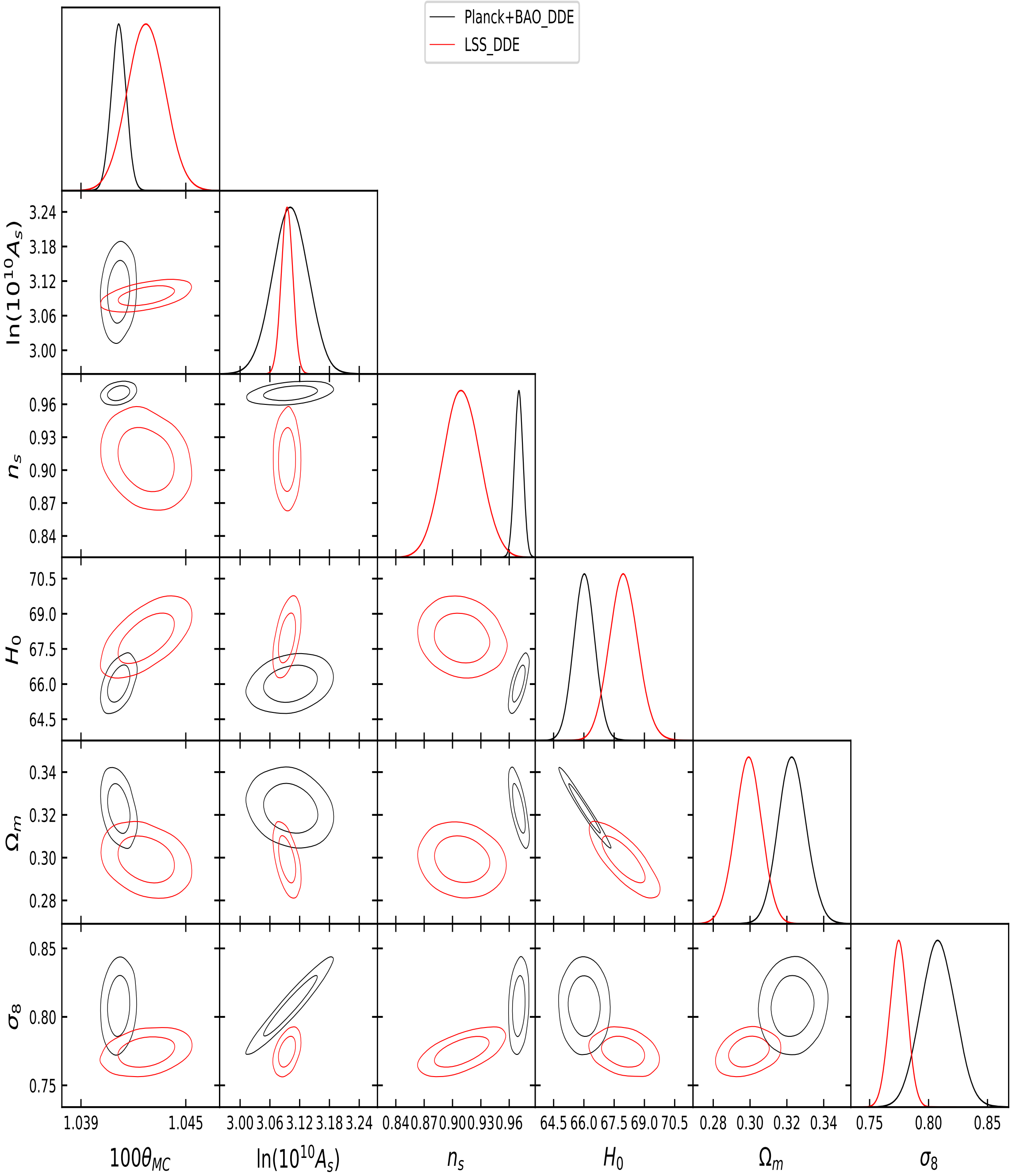

Figure 4.6: The triangle plot showing 1-σ and 2-σ contours of all the parameters for DDE model with $\sum m_\nu = 0.06$eV is shown here.

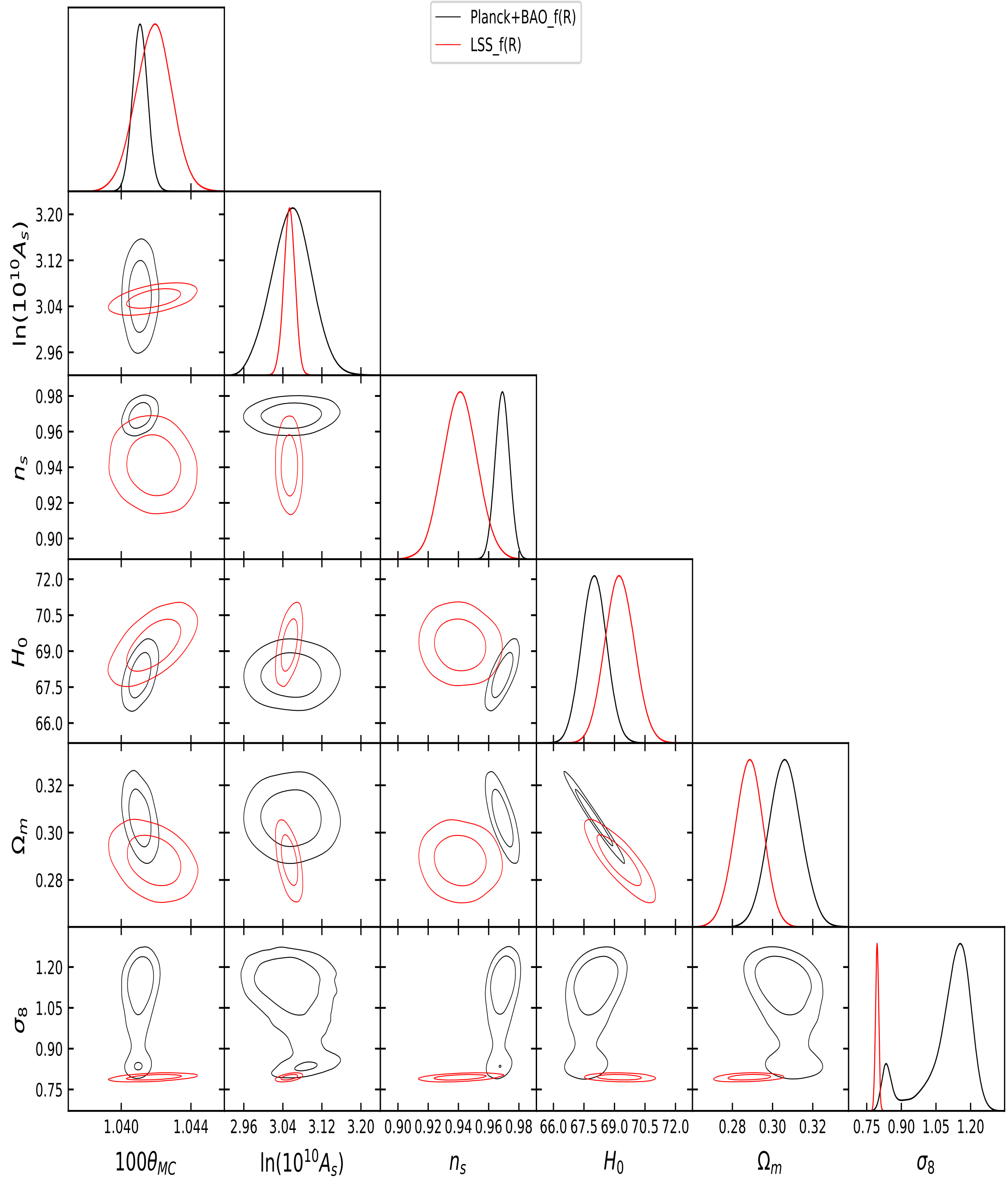

Figure 4.7: The triangle plot showing 1-σ and 2-σ contours of all the parameters for HS model with $\sum m_\nu = 0.06$eV is shown here.

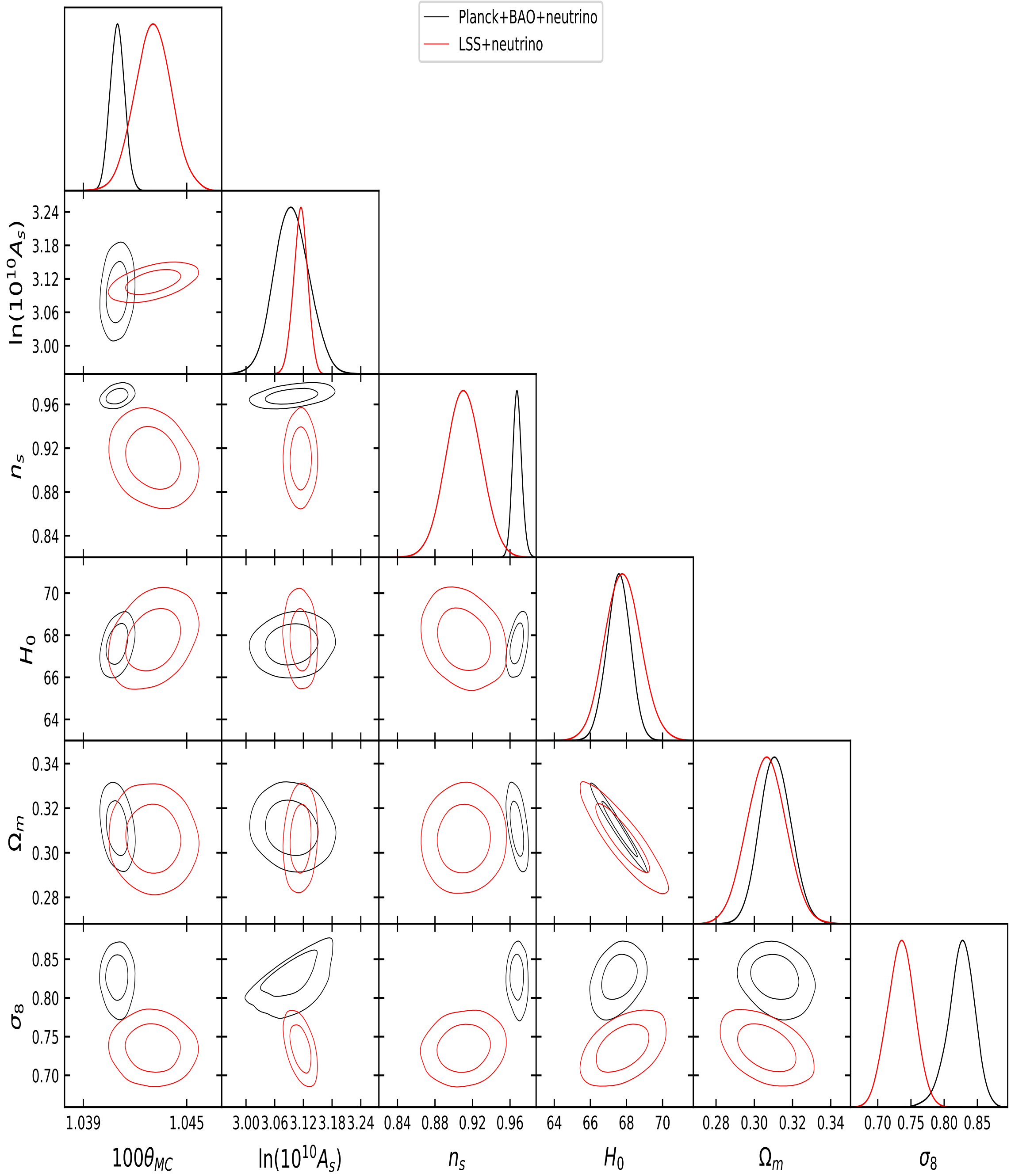

Figure 4.8: The triangle plot showing 1-σ and 2-σ contours of all the parameters for ΛCDM model with $\sum m_\nu$ as free parameter is shown here.

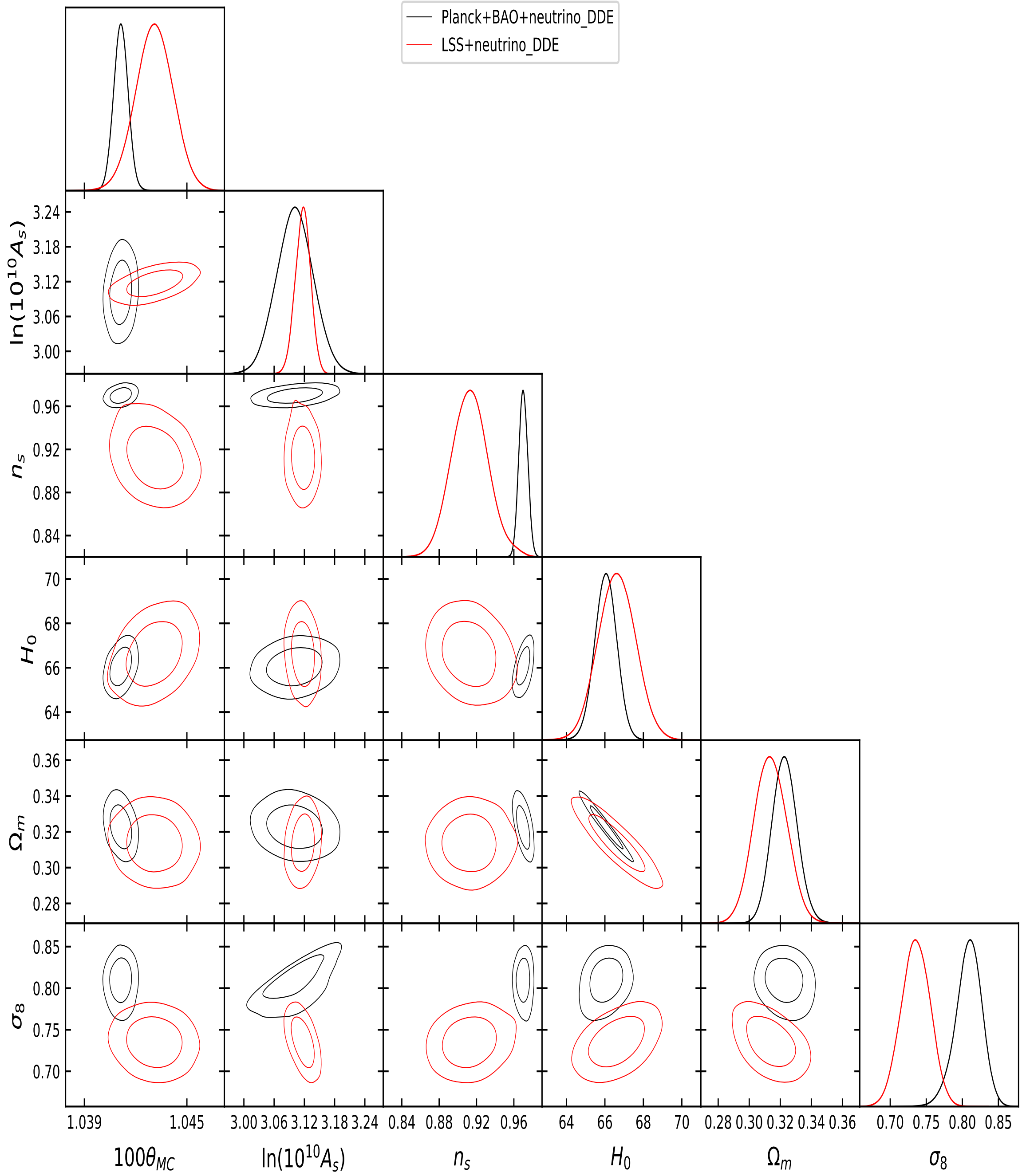

Figure 4.9: The triangle plot showing 1-σ and 2-σ contours of all the parameters for DDE model with $\sum m_\nu$ as free parameter is shown here.

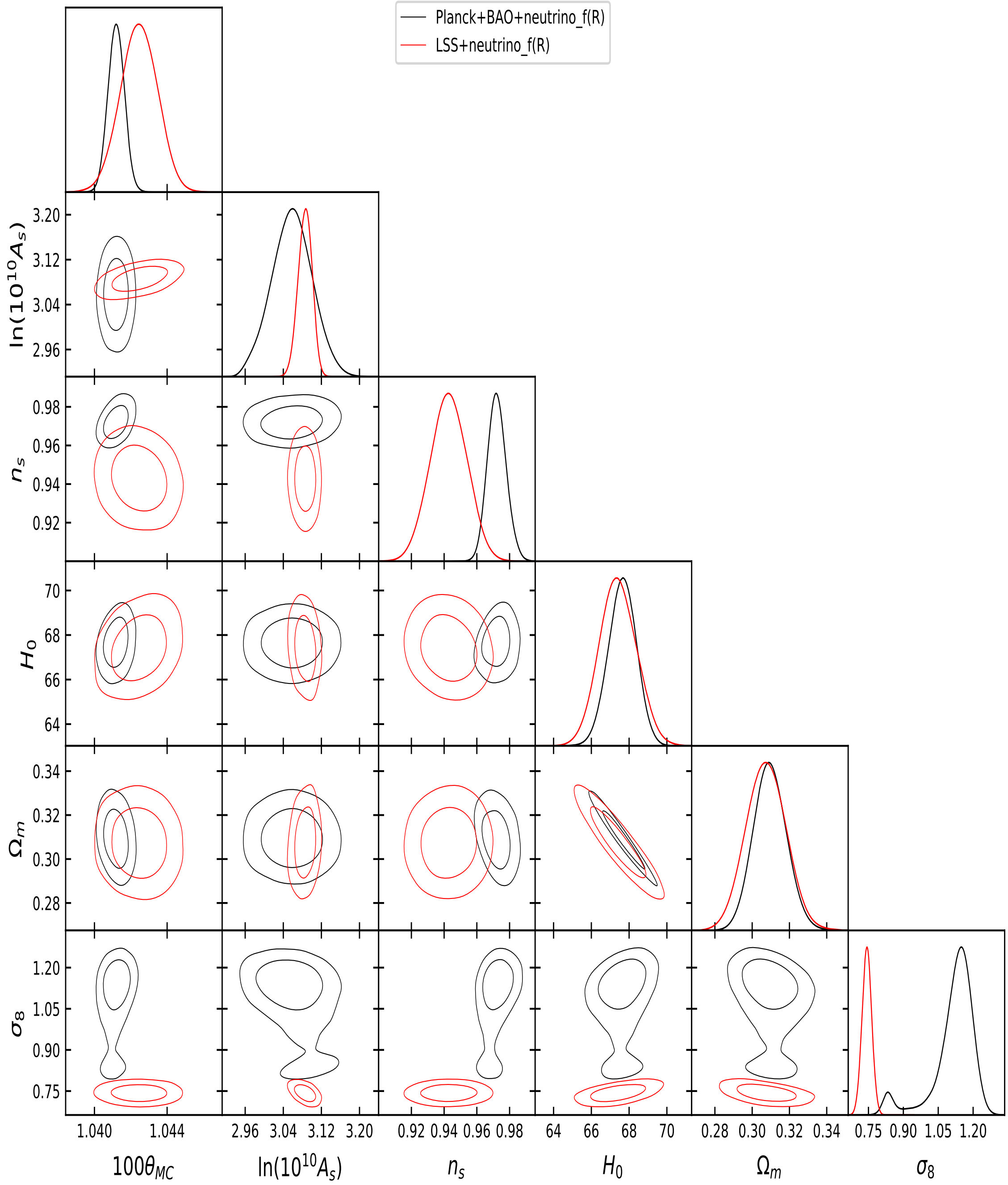

Figure 4.10: The triangle plot showing 1-σ and 2-σ contours of all the parameters for HS model with $\sum m_\nu$ as free parameter is shown here.

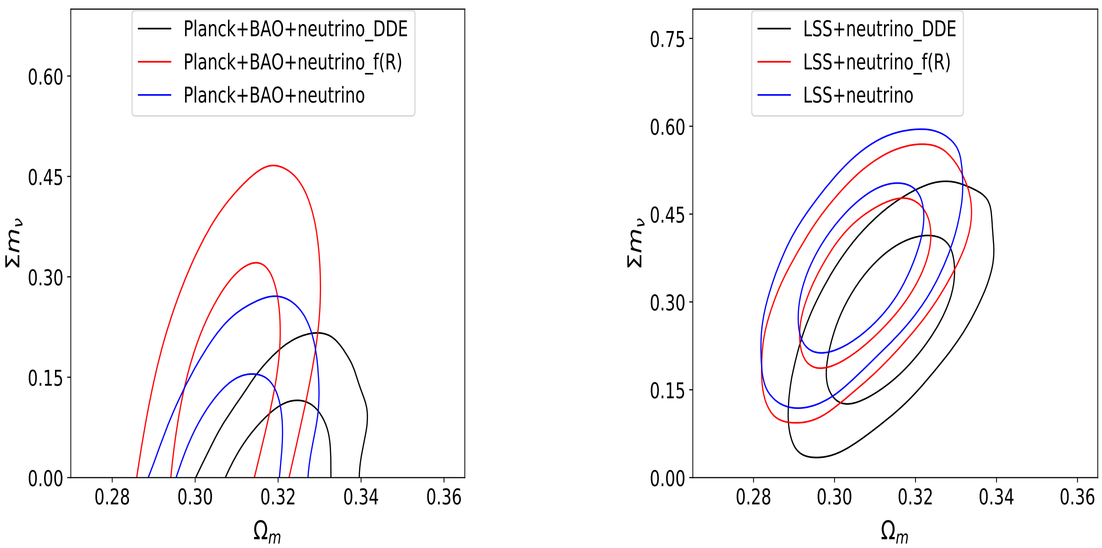

Figure 4.11: Bounds on the Neutrino mass in DDE, HS and ΛCDM models with Planck and LSS data.

Parameter	ΛCDM		DDE		HS	
	Planck+BAO	LSS	Planck+BAO	LSS	Planck+BAO	LSS
$\Omega_b h^2$	0.02227 ± 0.00020	0.02274 ± 0.00081	0.02236 ± 0.00020	0.02292 ± 0.00080	0.02243 ± 0.00022	0.02225 ± 0.00070
$\Omega_c h^2$	0.1190 ± 0.0013	0.1159 ± 0.0016	0.1178 ± 0.0013	0.1146 ± 0.0016	0.1185 ± 0.0013	0.1153 ± 0.0015
$100\theta_{MC}$	1.04098 ± 0.00042	1.0425 ± 0.0011	1.04116 ± 0.00042	1.0427 ± 0.0011	1.04108 ± 0.00043	1.0419 ± 0.0010
τ_{reio}	0.081 ± 0.018	0.08	0.086 ± 0.018	0.086	0.063 ± 0.020	0.65
$\ln(10^{10} A_s)$	3.094 ± 0.035	3.080 ± 0.012	3.101 ± 0.036	3.095 ± 0.011	3.058 ± 0.041	3.053 ± 0.011
n_s	0.9673 ± 0.0044	0.905 ± 0.019	0.9701 ± 0.0045	0.910 ± 0.019	0.9691 ± 0.0047	0.941 ± 0.011
H_0	67.65 ± 0.57	$69.81^{+0.73}_{-0.82}$	66.02 ± 0.52	67.98 ± 0.72	68.00 ± 0.61	69.26 ± 0.72
Ω_m	0.3102 ± 0.0077	0.2862 ± 0.0071	0.3230 ± 0.0077	0.2991 ± 0.0073	0.3062 ± 0.0079	0.2882 ± 0.0071
σ_8	0.829 ± 0.015	0.7917 ± 0.0074	0.808 ± 0.015	0.7745 ± 0.0074	$1.10^{+0.12}_{-0.030}$	0.7948 ± 0.0068
S_8	0.840 ± 0.018	$0.7732^{+0.0139}_{-0.0119}$	0.834 ± 0.018	$0.7732^{+0.0141}_{-0.0122}$	$1.105^{+0.110}_{-0.020}$	$0.7790^{+0.0137}_{-0.0119}$

Table 4.2: The best fit values with 1-σ error for all the parameters with fixed $\sum m_\nu$, obtained from the MCMC analyses for all the models considered are listed here.

the whole procedure to do the analysis with Planck+BAO and LSS data for HS model and obtain constraints for each parameter. Similar to the analysis for ΛCDM model, in the analysis of this model with LSS data, we fixed the $\tau_{reio} = 0.065$. The best fit values for σ_8 in this analysis are $1.10^{+0.12}_{-0.030}$ with Planck+BAO data and 0.7948 ± 0.0068 with LSS data. We plot the parameter space $\sigma_8 - \Omega_m$, obtained from analysis with two different data sets, see Fig. 4.2. We found that tension between the values of σ_8 inferred from Planck+BAO data and that from LSS data is increases.

Parameter	ΛCDM		DDE		HS	
	Planck+BAO	LSS	Planck+BAO	LSS	Planck+BAO	LSS
$\Omega_b h^2$	0.02228 ± 0.00020	0.02277 ± 0.00080	0.02236 ± 0.00020	0.02283 ± 0.00081	0.02254 ± 0.00025	$0.02216^{+0.00064}_{-0.00073}$
$\Omega_c h^2$	$0.1188^{+0.0015}_{-0.0014}$	0.1141 ± 0.0018	0.1177 ± 0.0014	0.1134 ± 0.0017	$0.1172^{+0.0020}_{-0.0017}$	0.1139 ± 0.0017
$100\theta_{MC}$	1.04097 ± 0.00042	1.0430 ± 0.0011	1.04114 ± 0.00042	1.0431 ± 0.0011	1.04120 ± 0.00045	1.0434 ± 0.0010
τ_{reio}	$0.082^{+0.018}_{-0.020}$	0.082	0.086 ± 0.018	0.086	0.065 ± 0.021	0.065
$\ln(10^{10} A_s)$	3.096 ± 0.037	3.114 ± 0.015	3.101 ± 0.036	3.117 ± 0.015	3.058 ± 0.042	3.085 ± 0.014
n_s	$0.9676^{+0.0045}_{-0.0050}$	0.911 ± 0.019	0.9702 ± 0.0047	0.913 ± 0.019	$0.9723^{+0.0053}_{-0.0060}$	0.943 ± 0.011
H_0	67.56 ± 0.65	67.80 ± 0.99	66.05 ± 0.57	66.65 ± 0.97	67.64 ± 0.74	67.45 ± 0.96
Ω_m	0.3112 ± 0.0082	0.306 ± 0.010	0.3227 ± 0.0079	0.314 ± 0.011	0.3096 ± 0.0089	0.307 ± 0.010
σ_8	$0.826^{+0.022}_{-0.017}$	0.735 ± 0.028	$0.809^{+0.019}_{-0.016}$	0.735 ± 0.020	$1.115^{+0.091}_{-0.034}$	0.743 ± 0.020
Σm_ν	< 0.157	0.364 ± 0.095	< 0.116	0.275 ± 0.095	< 0.318	0.333 ± 0.093
S_8	0.838 ± 0.022	$0.7431^{+0.0201}_{-0.0181}$	0.835 ± 0.020	$0.7522^{+0.0201}_{-0.0172}$	$1.127^{+0.089}_{-0.031}$	$0.7522^{+0.0201}_{-0.0175}$

Table 4.3: The best fit values with 1-σ error for all the parameters with varying $\sum m_\nu$, obtained from the MCMC analyses for all the models considered are listed here.

Next we do the analysis for DDE model. In our analysis for DDE model, in addition to the six standard parameters, we have two model parameters w_0 and w_a as defined in Sec. 4.2 making a total of eight parameters. First we do the MCMC analysis for both the data sets keeping w_a and w_0 as free parameters and get the 2-σ allowed ranges which are shown in Fig. 4.3. Next we put the non-phantom constraints represented by blue lines in Fig. 4.3. We see that the region allowed by both data sets satisfying the non phantom conditions $w_a + w_0 \geq -1$ and $w_0 \geq -1$ is very small and close to $w_0 = -0.9$ and $w_a = -0.1$. Therefore we choose these values for our further analysis, and do MCMC analysis scan over the remaining six parameters. We repeat the same procedure as we did for ΛCDM and HS model. First we do analysis with Planck+BAO data and get constraints on all the free parameters. In the analysis with LSS data, we fix $\tau_{reio} = 0.086$ (This value is obtained in the analysis with Planck+BAO data). We plot the parameter space $\sigma_8 - \Omega_m$, obtained from analysis with two different data sets, see Fig. 4.2. We find that tension between the values of σ_8 values inferred from Planck+BAO data and that from LSS data is somewhat alleviated in the DDE model. Constraints on σ_8, H_0, and other parameters for each model are listed in Tab. 4.2.

Next, we use sum of massive neutrino $\sum m_\nu$ as a free parameter and allow it to vary in the range [0,5]eV in our analysis for all three models. We repeat the whole procedure and obtain constraints for each parameter. We plot the parameter space $\sigma_8 - \Omega_m$ for each model, see Fig. 4.4. Constraints on $\sum M_\nu$, σ_8, H_0 and other parameters for each model are listed in Tab. 4.3. The triangle plots for all the three models with $\sum m_\nu = 0.06\text{eV}$ are shown in Figs. 4.5, 4.6 and 4.7. The triangle plots for all the three models with $\sum m_\nu$ as free parameter are shown in Figs. 4.8, 4.9 and 4.10. The corresponding 1σ and 2σ contours for $\sum M_\nu$ are shown in Fig. 4.11.

4.6 Discussion and Conclusion

Galaxy surveys and CMB lensing measure the parameter $\sigma_8\Omega_m^\alpha$, where Ω_m^α represents a model dependent growth function. In ΛCDM $\alpha = 0.5$ but it could be different for other DM-DE models. In CMB measurement of temperature anisotropy spectrum C_l and BAO determine Ω_m. The discrepancy between the CMB and LSS measurement is determined by the model dependent growth function Ω_m^α. The growth function can thus be used for testing theories of gravity and dynamical DE. In the present chapter we tested HS and DDE models in the context of $\sigma_8 - \Omega_m$ observations. We find that in the HS model the $\sigma_8 - \Omega_m$ tension worsens compared to the ΛCDM model. On the other hand in the DDE model there is slight improvement in the concordance between the two data sets. The discrepancy levels between values inferred from Planck+BAO and LSS data for ΛCDM, DDE and HS model are listed in Tab. 4.4. We also find that adding active massive neutrinos allows us to have larger value of Ω_m. $H(z)$ in $H(z) = H_0\sqrt{\Omega_m(1+z)^3 + \Omega_\Lambda}$ is determined by the observation, therefore a larger value of Ω_m brings down the H_0 value to satisfy the observation. Thus, we find that the H_0 tension between CMB and LSS observations is resolved by using active massive neutrinos. However, this increases the mismatch between H_0 values obtained from LSS and SN-Ia observations. In all three models, the n_s values obtained in the analysis with LSS data is smaller as compared to n_s value obtained from Planck+BAO which gives rise to another tension between the two data sets. The tilt of the primordial spectrum is calculated at a particular pivot scale(k_*). In our analysis the pivot scale is 0.05 Mpc^{-1}. The n_s discrepancy may be due to the fact that Planck data and LSS data have different pivot scale which can be a signature of running tilt of the primordial spectrum. This can be checked in future works. The bounds on neutrino mass become more stringent in the DDE model. In the HS model there is a loosening in the analysis with Planck data and not much effect in the analysis with the LSS data. In conclusion we see that σ_8 measurement from CMB and LSS experiments

	ΛCDM	DDE	HS
With fixed $\sum M_\nu$	1.722σ	1.522σ	1.793σ
With varying $\sum M_\nu$	1.960σ	1.796σ	2.273σ

Table 4.4: The descrepancy level between the σ_8 values inferred from Planck+BAO and LSS data for ΛCDM, DDE and HS model are listed here.

can be used as a probe of modified gravity or quintessence models. Future observations of CMB and LSS may shrink the parameter space for $\sigma_8 - \Omega_m$ and then help in selecting the correct $f(R)$ and DDE theory.

Chapter 5

Black Hole Observations and Phenomenology

As mentioned in the Sec. 2.5, the EHT has measured the angular diameter of the BH shadow to be 42 ± 3 μas [18–20] with an axis ratio of $4/3$. The observation puts an upper bound of 10$\%$ on the deviation from the circularity of the shadow of the M87* BH. A deviation from circularity could be a sign of it being a non-Kerr BH. Several studies using various non-Kerr black holes with origin either in general relativity or in string theory have tried to explain the observed deviation [261–264].

In this chapter, we explore the possibility of the M87* being a Kerr-Sen black hole (KSBH) [265] by assisting the EHT observation with the polarization measurements [266–270] of the same. In the absence of any polarimetry data from the EHT we use polarimetry studies given in ref. [266]. The analysis in [266] concludes that due to the large uncertainties in the measurements it is difficult to distinguish between the Faraday rotation and the internal rotation of the polarization angle. In case M87* is a KSBH, this rotation can be due to axion-photon interaction in the vicinity of the BH [271].

There have been several studies on the features of a KSBH including lensing [272–274], particle orbits [275], particle collision around KSBH [276], merger estimates [277] null geodesics and photon capture to produce a shadow [278–284], cosmic censorship [285, 286] and comparison with other rotating charged black holes [278, 287–289].

This chapter is organized in the following manner. In Sec. 5.1, a brief introduction to the KSBH is given. We calculate the trajectories of the null geodesics ending in unstable circular orbits to get the shadow of the KSBH in Sec. 5.2. In Sec. 5.3, we calculate the rotation of the polarization of circularly polarized photons around the KSBH due to its axion hair. Finally we conclude in Sec. 5.4 with discussions on the possible consequences of the results.

5.1 Kerr-Sen Black Hole

The no-hair theorem states that all black hole solutions of the Einstein-Maxwell theory can be completely characterized by only three parameters: mass, electric charge, and angular momentum. As we know, the Kerr-Newman metric is a solution for a rotating and charged black hole in the Einstein-Maxwell field equation. However, rotating and charged black hole solutions can also be found in other theories, such as string theory. Black holes in string theory can be coupled with other fields, such as the dilaton field, Yang-Mills field, and antisymmetric tensor gauge field. The Kerr-Sen black hole is a solution of the low-energy effective field theory [265] for heterotic string theory and is also characterized by mass, electric charges, and angular momentum, which are similar to those of the Kerr-Newman black hole. However, the geometry of the Kerr-Sen black hole is different from that of the Kerr-Newman black hole. Apart from checking the distinguishability of KSBH from KNBH, this particular chapter is motivated from the fact that KSBH arises from string theory and hence testing KS metric is an indirect test of string theory.

The KSBH is a rotating charged black hole which emerges as a solution to the low energy 4-dimensional effective action of the heterotic string theory involving the dilaton, a $U(1)$ gauge field and an axion appearing through the Kalb-Ramond 3-form tensor. The Kalb-Ramond field is made up of an axion field and the Chern-Simons term for the gauge field assuming weak gravity in the region far away from the space-time singularity of the KSBH. Due to this, axions become a natural hair of the black hole instead of being a part of the cloud in the accretion disk. In [265], Sen constructed a rotating charged black hole solution by applying certain transformations [290–305] on the Kerr black hole solution [306]. The form of the heterotic string action used in [265] and written in the string frame is

$$S = \int d^4x\sqrt{\mathcal{G}}e^{-\tilde{\phi}}\left(\tilde{R}' - \frac{1}{12}\tilde{H}'^2 - \partial'_\mu\tilde{\phi}\partial^{\mu'}\tilde{\phi} - \frac{\tilde{F}'^2}{8}\right), \tag{5.1}$$

where $\mathcal{G}_{\mu\nu}$ is the string frame metric and the prime on various quantities denotes the string frame equivalents of the Ricci scalar $\tilde{R}$, the Kalb-Ramond 3-form $\tilde{H}_{\mu\nu\lambda}$, the gauge field $\tilde{F}_{\mu\nu}$ and ϕ is the dilatonic field used to make the conformal transformation from the Einstein frame to the string frame. This is a low energy effective string action written upto $\mathcal{O}(\alpha')$ where α' is the inverse string tension. The low energy effective heterotic string action in four dimensions upto $\mathcal{O}(\alpha')$ as given in [287] is

$$S = \int d^4x\sqrt{g}\left(\frac{R}{2\kappa^2} - 6\,e^{-2\sqrt{2}\kappa\phi}H^{\mu\nu\lambda}H_{\mu\nu\lambda} - \frac{1}{2}\partial_\mu\phi\partial^\mu\phi - \frac{\alpha'}{16\kappa^2}e^{-\sqrt{2}\kappa\phi}F_{\mu\nu}F^{\mu\nu}\right), \tag{5.2}$$

where $H_{\mu\nu\lambda}$ is the Kalb-Ramond 3-form, R is the Ricci scalar and $F_{\mu\nu} = \partial_\mu A_\nu - \partial_\nu A_\mu$ is the gauge field all in the Einstein frame while ϕ is the dilatonic field and $\kappa^2 = M_{Pl}^{-2}$. We scale the action in Eq. 5.2 by $2\kappa^2$ and absorb the constants κ and α' in the fields by the following redefinitions

$$\begin{aligned} \tilde{H}_{\mu\nu\lambda} &= 12\kappa H_{\mu\nu\lambda}, \\ \tilde{\phi} &= \sqrt{2}\kappa\phi, \\ \tilde{F}_{\mu\nu} &= \sqrt{\alpha'}F_{\mu\nu}, \end{aligned} \tag{5.3}$$

In terms of the new fields $\tilde{H}_{\mu\nu\lambda}$, $\tilde{F}_{\mu\nu}$ and $\tilde{\phi}$, the action in Eq. 5.2 becomes

$$S = \int d^4x\sqrt{g}\left(R - \frac{1}{12}e^{-2\tilde{\phi}}\tilde{H}^2 - \partial_\mu\tilde{\phi}\,\partial^\mu\tilde{\phi} - \frac{1}{8}e^{-\tilde{\phi}}\tilde{F}^2\right). \tag{5.4}$$

The action in Eq. 5.4 is also the exact Einstein frame equivalent of the Sen action given in Eq. 5.1 obtained by transforming the string frame metric, $\mathcal{G}_{\mu\nu}$, to the Einstein frame metric, $g_{\mu\nu}$ by

$$\mathcal{G}_{\mu\nu} = e^{\tilde{\phi}}g_{\mu\nu}. \tag{5.5}$$

We ignore terms with more than two derivatives in metric since we are interested in regions far from a space-time singularity. This allows us to write the Kalb-Ramond 3-form as just a fully antisymmetrized derivative of an axion field and the gauge field Chern-Simons terms in the following manner

$$H_{\mu\nu\lambda} = \frac{e^{\sqrt{2}\kappa\phi}}{6\sqrt{2}}\epsilon_{\alpha\mu\nu\lambda}\partial^\alpha\chi - \frac{\alpha'}{32\kappa\sqrt{g}}A_{[\mu}F_{\nu\lambda]}, \tag{5.6}$$

where χ is the axion field and the square brackets around the indices denote a cyclic sum over the indices.

In the present case, we limit to the $U(1)$ gauge field. Substituting $H_{\mu\nu\lambda}$ in Eq. 5.2 in favor of the axion and the gauge fields we get

$$\begin{aligned} S &= \int d^4x\sqrt{g}[\frac{R}{2\kappa^2} - \frac{1}{2}\partial_\mu\phi\partial^\mu\phi - \frac{1}{2}\partial_\mu\chi\partial^\mu\chi - \frac{\alpha'}{16\kappa^2}e^{-\sqrt{2}\kappa\phi}F_{\mu\nu}F^{\mu\nu} \\ & -\frac{\alpha'}{8\kappa}\frac{6\sqrt{2}}{4!}e^{-\sqrt{2}\kappa\phi}\frac{\epsilon^{\mu\nu\lambda\sigma}}{\sqrt{g}}\chi F_{\mu\nu}F_{\lambda\sigma}] \end{aligned} \tag{5.7}$$

such that the equations of motion are as given below:

$$\Box\chi = \frac{\alpha'}{8\kappa}\frac{6\sqrt{2}}{4!}F_{\mu\nu}(^\star F)^{\mu\nu}e^{-\sqrt{2}\kappa\phi}, \tag{5.8}$$

$$\Box\phi = -e^{-\sqrt{2}\kappa\phi}\left[\frac{\sqrt{2}\alpha'}{16\kappa}F_{\mu\nu}F^{\mu\nu} + \frac{\sqrt{2}\alpha'}{48}\chi F_{\mu\nu}(^\star F)^{\mu\nu}\right], \tag{5.9}$$

$$\nabla_\mu F^{\mu\nu} = -\frac{\kappa}{\sqrt{2}}\left(\partial_\alpha\chi\right)\left(^\star F\right)^{\alpha\nu} \tag{5.10}$$

The solution for ϕ and χ is proportional to α'. Therefore upto the leading order in α', we can switch $e^{-\sqrt{2}\kappa\phi}\alpha' \to \alpha'$ and neglect the second term inside the bracket in the dilaton equation. The reduced equations of motion are:

$$\Box\chi = \frac{\alpha'}{8\kappa}\frac{6\sqrt{2}}{4!}F_{\mu\nu}(^\star F)^{\mu\nu}, \tag{5.11}$$

$$\Box\phi = -\frac{\sqrt{2}\alpha'}{16\kappa}F_{\mu\nu}F^{\mu\nu}, \tag{5.12}$$

$$\nabla_\mu F^{\mu\nu} = -\frac{\kappa}{\sqrt{2}}\left(\partial_\alpha\chi\right)\left(^\star F\right)^{\alpha\nu}, \tag{5.13}$$

where $(^\star F)^{\mu\nu} = \frac{\epsilon^{\mu\nu\lambda\sigma}}{\sqrt{g}}F_{\lambda\sigma}$ is the dual of $F_{\mu\nu}$, $\Box$ is the d'Alembertian operator: $\Box = \nabla_\mu\nabla^\mu$ and ∇_μ is the covariant derivative operator. The action given in Eq. 5.4 admits the following metric (named the Sen metric) as one of the inequivalent solutions obtained by the twisting procedures shown in [290–305]:

$$\begin{aligned} ds^2 &= -\frac{(r^2+a^2\cos^2\theta-2\mu r)(r^2+a^2\cos^2\theta)}{(r^2+a^2\cos^2\theta+2\mu r\sinh^2\frac{\alpha}{2})^2}dt^2 \\ &+\frac{r^2+a^2\cos^2\theta}{r^2+a^2-2\mu r}dr^2+(r^2+a^2\cos^2\theta)d\theta^2 \\ &+\{(r^2+a^2)(r^2+a^2\cos^2\theta)+2\mu r a^2\sin^2\theta+4\mu r(r^2+a^2)\sinh^2\frac{\alpha}{2} \end{aligned}$$

$$
\begin{aligned}
&+4\mu^2 r^2 \sinh^4 \frac{\alpha}{2}\} \times \frac{(r^2 + a^2\cos^2\theta)\sin^2\theta}{(r^2 + a^2\cos^2\theta + 2\mu r\sinh^2\frac{\alpha}{2})^2} d\phi^2 \\
&- \frac{4\mu r a \cosh^2\frac{\alpha}{2}(r^2 + a^2\cos^2\theta)\sin^2\theta}{(r^2 + a^2\cos^2\theta + 2\mu r\sinh^2\frac{\alpha}{2})^2} dt d\phi, \qquad (5.14)
\end{aligned}
$$

and the field solutions are

$$
\chi = -Q^2 \frac{\alpha'}{\kappa} \frac{a}{GM} \frac{\cos\theta}{r^2 + a^2\cos\theta}, \qquad (5.15)
$$

$$
A_t = -\frac{1}{\sqrt{\alpha'}} \left(\frac{2\mu r a \sinh\alpha \sin^2\theta}{r^2 + a^2\cos^2\theta + 2\mu r \sinh^2\frac{\alpha}{2}} \right), \qquad (5.16)
$$

$$
A_\phi = \frac{1}{\sqrt{\alpha'}} \left(\frac{2\mu r \sinh\alpha}{r^2 + a^2\cos^2\theta + 2\mu r \sinh^2\frac{\alpha}{2}} \right), \qquad (5.17)
$$

where the constants μ, α and a give the physical mass M, charge Q and angular momentum J through multipole expansions of g_{tt}, A_t and $g_{t\phi}$ respectively in powers of $1/r$,

$$
GM = \frac{\mu}{2}(1 + \cosh\alpha), \quad \sqrt{\alpha'}Q = \frac{\mu}{\sqrt{2}}\sinh\alpha, \quad J = \frac{a\mu}{2}(1 + \cosh\alpha). \qquad (5.18)
$$

The metric in Eq. 5.14 has a space-time singularity at $r = 0$ bound by two horizons at r_- and r_+ which encapsulate a rotating charged black hole, called the Kerr-Sen (KS) black hole. In terms of M, Q and J, $r_\pm$ are

$$
r_\pm = GM - \frac{Q^2}{2M} \pm \sqrt{\left(GM - \frac{Q^2}{2M}\right)^2 - \frac{J^2}{M^2}}. \qquad (5.19)
$$

The existence condition of the horizons ($r_\pm$ must be real and non-negative) gives a bound for the mass, charge and rotation of the black hole inside the horizon

$$
\left(GM - \frac{Q^2}{2M}\right)^2 \geq \frac{J^2}{M^2}, \qquad (5.20)
$$

called horizon regularity condition which is shown in the Fig. 5.1 along with a comparison of the horizon regularity for the charged rotating Kerr-Newman black hole (KNBH) arising from general relativity. A feature that distinguishes the KS black hole from the KNBH is its increased intrinsic charge carrying capacity without falling into a naked singularity.

5.2 Black Hole Image and Deviation from Circularity

Photons coming from a light source behind the black hole are either scattered away or fall into the black hole depending on their impact parameter from the black hole. The null

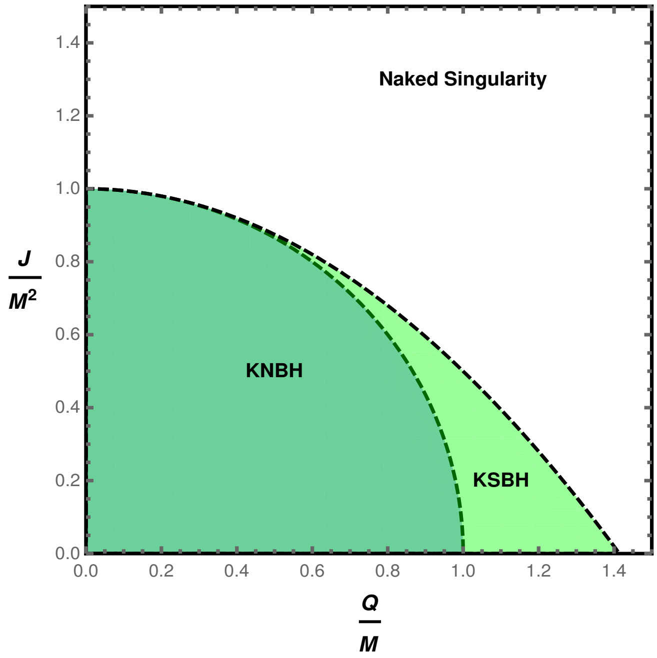

Figure 5.1: The dashed line shows the region where $r_- = r_+$. This is the extremal value where horizons can exist. The shaded region is where the black hole is bound by horizons while the unshaded region depicts a naked singularity marked by an absence of horizons. It's also seen that the KSBH can carry more charge than the KNBH.

geodesics which describe the circular photon orbits around the black hole are specially interesting because of their observational importance. These geodesics describe a capture region which can be understood as the shadow of the black hole cast at an observer at infinity in the impact parameter space [307–309]. This shadow can give information about the space-time behavior in a region of strong gravity near a black hole. Calculations in this section are done in geometric units with $G = c = 1$. For convenience, we use the Boyer-Lindquist coordinates [310] as follows

$$\Delta \equiv r(r + r_0) - 2Mr + a^2 \ , \quad \rho^2 \equiv r(r + r_0) + a^2 \cos^2\theta \ . \tag{5.21}$$

In terms of these new coordinates, the KS metric in Eq. 5.14 can be written as

$$\begin{aligned} ds^2 = &-\left(1 - \frac{2Mr}{\rho^2}\right) dt^2 - \frac{4Mra\sin^2\theta}{\rho^2} dt d\varphi + \frac{\rho^2}{\Delta} dr^2 + \rho^2 d\theta^2 \\ &+ \left(r(r + r_0) + a^2 + \frac{2Mra^2\sin^2\theta}{\rho^2}\right) \sin^2\theta d\varphi^2, \end{aligned} \tag{5.22}$$

with $r_0 = Q^2/M$.

5.2.1 Hamilton-Jacobi Equation

We use the formalism given in [311] to find the separate equations of motion. The Hamilton-Jacobi equation is given by

$$2\frac{\partial S}{\partial \lambda} = g^{\mu\nu}\frac{\partial S}{\partial x^\mu}\frac{\partial S}{\partial x^\nu}, \tag{5.23}$$

where $S(\lambda, x^\mu)$ is the Jacobian action and λ is the affine parameter. Motion of a test particle in an axisymmetric space-time, such as Kerr-Sen space-time, has two conserved quantities, angular momentum L_z with respect to the rotation axis of the black hole and energy E, associated with two Killing vectors ∂_ϕ and ∂_t respectively. Since the Hamiltonian is also independent of the affine parameter λ, the solution for S can be separated in terms of these to get

$$S = \frac{1}{2}m^2\lambda - Et + L_z\phi + S_{r\theta}(r,\theta). \tag{5.24}$$

$S_{r\theta}$ can be further separated into $S_r(r)$ and $S_\theta(\theta)$ as the metric in Eq. 5.22 doesn't have any $g_{r\theta}$ term, to finally give [312]

$$S(\lambda, x^\mu) = \frac{1}{2}m^2\lambda - Et + L_z\phi + S_r(r) + S_\theta(\theta), \tag{5.25}$$

where m is mass of the test particle.

Using Eq. 5.25 in Eq. 5.23 we get the separated radial and azimuthal parts of Hamilton-Jacobi equation [307, 312]

$$\Delta^2\left(\frac{dS_r}{dr}\right)^2 = \mathcal{R}(r) \Rightarrow S_r(r) = \int^r dr'\frac{\sqrt{\mathcal{R}(r')}}{\Delta}, \tag{5.26}$$

$$\left(\frac{dS_\theta}{d\theta}\right)^2 = \Theta(\theta) \Rightarrow S_\theta(\theta) = \int^\theta d\theta'\sqrt{\Theta(\theta')}, \tag{5.27}$$

with

$$\mathcal{R}(r) = \left[-\left\{r(r+r_0)+a^2\right\}E + aL_z\right]^2 - \Delta\left[\mathcal{Q} + (L_z - aE)^2 + m^2 r(r+r_0)\right], \tag{5.28}$$

$$\Theta(\theta) = \mathcal{Q} - \left(L_z^2\csc^2\theta - a^2E^2\right)\cos^2\theta - m^2a^2\cos^2\theta, \tag{5.29}$$

where $\mathcal{Q}$ is the constant of separation, also called the Carter constant [311].

Using the definitions $p_\mu \equiv \partial S/\partial x^\mu$ and $\partial x^\mu/\partial\lambda \equiv g^{\mu\nu}p_\nu$ we find the following equations of motion for the radial and azimuthal motion of the particle

$$\rho^4\left(\frac{dr}{d\lambda}\right)^2 = \mathcal{R}(r), \tag{5.30}$$

$$\rho^4 \left(\frac{d\theta}{d\lambda}\right)^2 = \Theta(\theta), \tag{5.31}$$
$$\rho^4 \left(\frac{d\phi}{d\lambda}\right)^2 = \frac{1}{\Delta^2}\left[2MarE + L_z \csc^2\theta\,(\Sigma - 2Mr)\,,\right]^2, \tag{5.32}$$

where

$$\Sigma \equiv \left[r(r+r_0)+a^2\right]^2 - a^2\Delta\sin^2\theta. \tag{5.33}$$

For a massless particle such as a photon coursing along null geodesics, $m = 0$, and the potentials $\mathcal{R}(r)$ and $\Theta(\theta)$ are parametrized only by E, L_z and the Carter's constant $\mathcal{Q}$. Scaling these potentials by E^2 such that $\mathcal{R}(r) = \overline{\mathcal{R}}(r)E^2$ and $\Theta(\theta) = \overline{\Theta}(\theta)E^2$ and defining

$$\xi \equiv \frac{L_z}{E}, \quad \eta \equiv \frac{\mathcal{Q}}{E^2}, \tag{5.34}$$

we get the following form for the E^2 scaled potentials $\overline{\mathcal{R}}$ and $\overline{\Theta}$

$$\overline{\mathcal{R}}(r) = \left[-\left\{r(r+r_0)+a^2\right\}+a\xi\right]^2 - \Delta\left[\eta+(a-\xi)^2\right], \tag{5.35}$$
$$\overline{\Theta}(\theta) = \eta - \left(\xi^2\csc^2\theta - a^2\right)\cos^2\theta, \tag{5.36}$$

From Eqs. 5.35 and 5.36 it's clear that the motion of a photon on a null geodesic is parametrized only by two parameters ξ and η [272].

5.2.2 Photon Orbits

Circular photon orbits are characterized by the vanishing of the radial potential and its derivative at r_{cpo},

$$\begin{aligned} \overline{\mathcal{R}}(r_{cpo}) &= 0, \\ \partial_r\overline{\mathcal{R}}(r_{cpo}) &= 0, \end{aligned} \tag{5.37}$$

where r_{cpo} is the radius of the photon orbit. The conditions in Eq. 5.37 can be used to solve for ξ and η in Eq. 5.35. There are two pairs of solutions

$$\xi = \frac{r(r+r_0)+a^2}{a}, \quad \eta = -\frac{r^2(r+r_0)^2}{a^2}, \tag{5.38}$$

and,

$$\xi = \frac{a^2\left(-2r_{\text{cpo}} - 2M - r_0\right) + 6Mr_{\text{cpo}}^2 + 2Mr_0r_{\text{cpo}} - 2r_{\text{cpo}}^3 - 3r_0r_{\text{cpo}}^2 - r_0^2r_{\text{cpo}}}{a\left(r_{\text{cpo}} - M + \frac{r_0}{2}\right)},$$

$$\eta = \frac{a^2 r_{\text{cpo}}^2 \left(16 M r_{\text{cpo}} + 8 M r_0\right) - r_{\text{cpo}}^2 \left(\left(r_{\text{cpo}} + r_0\right)\left(2 r_{\text{cpo}} + r_0\right) - 2M \left(3 r_{\text{cpo}} + r_0\right)\right)^2}{a^2 \left(2 r_{\text{cpo}} - 2M + r_0\right)^2} \tag{5.39}$$

for the solution pair in Eq. 5.38 the azimuthal potential Θ becomes negative which isn't allowed (see Eq. 5.27). On the other hand, the solution pair in Eq. 5.39 does give a consistent solution for the circular photon orbits.

Black hole image observations rely on photons that can reach the observer. Therefore, we need to look at unstable circular orbits of photons orbiting outside the exterior horizon of the KSBH, $r_{cpo} > r_+$. These photons reach the observer after a finite number of rotations around the black hole. If the distance between the black hole and the observer is l_0 and the angle of inclination (also called the viewing angle) of the black hole shadow is θ, then the photon has impact parameters (also known as the celestial coordinates) given by [313, 314] defined by

$$\alpha = \lim_{l_0 \to \infty} \left(-l_0^2 \sin\theta \frac{d\phi}{dr}\right), \beta = \lim_{l_0 \to \infty} \left(l_0^2 \frac{d\theta}{dr}\right). \tag{5.40}$$

Using Eq. 5.30-Eq. 5.32 in Eq. 5.40 we get

$$\alpha = -\xi \csc\theta, \quad \beta = \pm\sqrt{\eta + a^2 \cos^2\theta - \xi^2 \cot^2\theta}. \tag{5.41}$$

A representative image/shadow for the KSBH for the mass normalized celestial coordinates α/M and β/M is shown the Fig. 5.2.

5.2.3 Deviation of the BH Shadow from Circularity

As can be seen in Fig. 5.2, the image of the black hole is not an exact circle for non-zero values of the black hole charge, angular momentum and its inclination angle with respect to the observer. The amount of deviation from circularity is a measurable quantity and can give insight into the values of certain black hole hairs e.g. its charge and angular momentum. The image of the black hole is symmetric under reflection around $\beta = 0$ which is the α-axis. This tells us that the geometric center of this diameter is at $\beta = 0$. However, the geometric center under reflections around the β axis is shifted from $\alpha = 0$ and it's not symmetric as well. The geometric center of the image on the α axis is obtained by taking its mean $\alpha_C = \int \alpha dA / \int dA$ where dA is the area element of the image and fixing $\beta = 0 = \beta_C$.

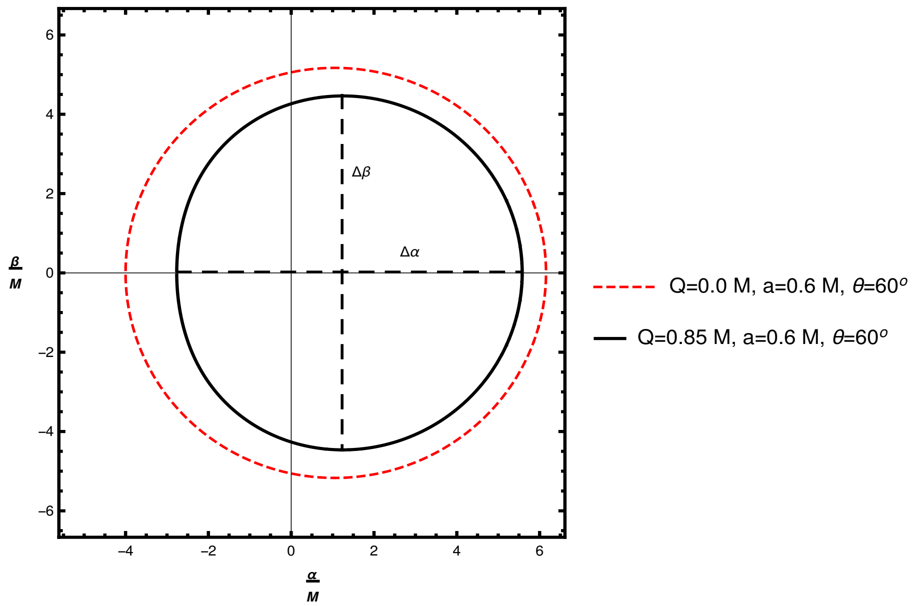

Figure 5.2: For fixed inclination angle θ and spin a the photon capture region gets smaller and deviates from circularity as the charge increases. Here we show the photon capture region for $\theta = 60^o$ and $a = 0.6M$ for $Q = 0$ (red, dashed) and $Q = 0.85M$ (black, solid).

One can now define the angle γ that a point (α, β) on the boundary of the image subtends on the α axis at the geometric center, $(\alpha_C, 0)$. If $\ell(\gamma)$ is the distance between the point (α, β) and $(\alpha_C, 0)$, the average radius $\bar{R}$ of the image is given by [315]

$$\begin{aligned} R_{avg}^2 &\equiv \frac{1}{2\pi}\int_0^{2\pi} d\gamma\, \ell^2(\gamma) \\ \text{where,} \quad \ell(\gamma) &\equiv \sqrt{\left(\alpha(\gamma) - \alpha_C\right)^2 + \beta(\gamma)^2}\,. \end{aligned} \tag{5.42}$$

Finally, the deviation from circularity, ΔC, is defined as the RMS difference of the distance between any point on the boundary and the center from the average radius of the shadow R_{avg} [315],

$$\Delta C \equiv \frac{1}{R_{avg}}\sqrt{\frac{1}{2\pi}\int_0^{2\pi} d\gamma\left(\ell(\gamma) - R_{avg}\right)^2}\,. \tag{5.43}$$

Another parameter that can be defined to quantify non-circularity of the photon shadow is the ratio of the diameters along the two axes [316]

$$D = \frac{\Delta\beta}{\Delta\alpha}. \tag{5.44}$$

For an inclination angle of 17^o, The EHT collaboration observed the angular diameter of the shadow of M87* BH to be $(42 \pm 3)\mu$as [18–20] with the axis ratio 4/3 which translates to an upper bound of 10 percent on ΔC. Since ΔC is a function of a and Q/M, this bound can be used to put constraints on the spin and charge of the black hole.

The variation of ΔC and D with charge for $\theta = 17^o$ and $a = 0.9M$ is shown in Fig. 5.3. As can be seen that ΔC and D do not reach the upper bound reported by the EHT collaboration which implies that with the accuracy of the EHT observation we cannot put any constraints on spin or charge of the KSBH.

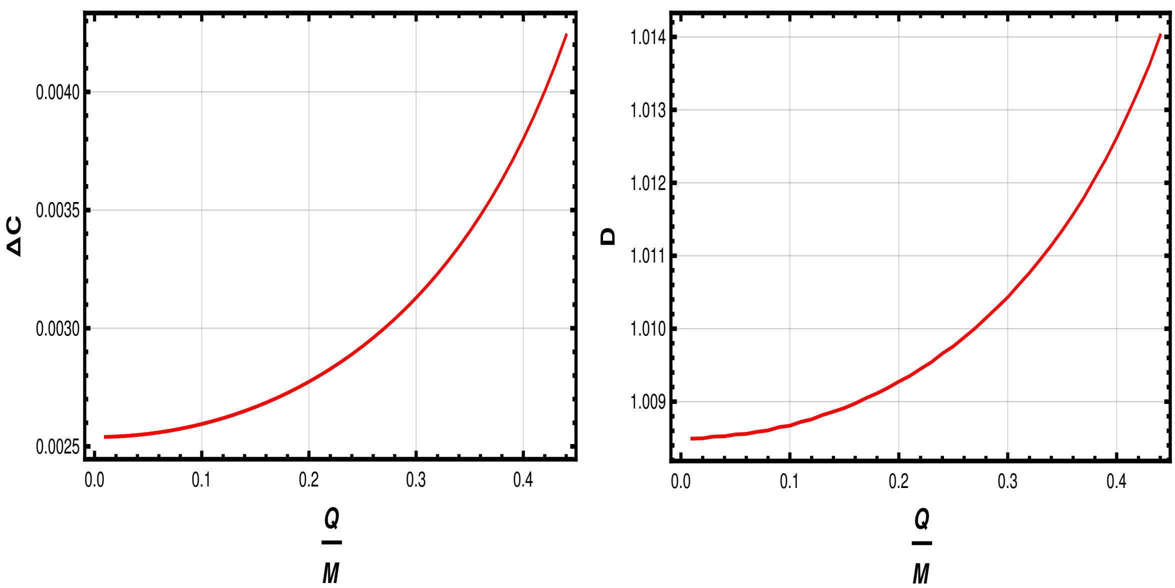

Figure 5.3: The deviation from circularity, ΔC, and the axis-ratio, D, as a function of Q for $a = 0.9M$ and $\theta = 17^0$.

5.3 Polarisation of Light by Axions

Circularly polarized photons coming from behind the black hole or those in the circular orbits around the black hole outside the horizon can interact with axions leading to axion-photon oscillation and birefringence such that their polarization angle gets rotated [317–320]. This rotation of the polarization (frequency independent "Faraday rotation") is an intrinsic feature of the black hole, distinguishing it from the usual Faraday rotation which is dependent on the wavelength of the photon.

The Lagrangian to study the polarization of light signal due to the axion cloud of the

KSBH is (see Eq. 5.10)

$$\mathcal{L} \supset \frac{\alpha'}{16\kappa^2} F_{\mu\nu} F^{\mu\nu} + \frac{\alpha'}{8\kappa} \frac{6\sqrt{2}}{4!} \chi F_{\mu\nu} \tilde{F}^{\mu\nu}. \tag{5.45}$$

And, the equation of motion of $F_{\mu\nu}$ is:

$$\partial_\mu F^{\mu\nu} = -\frac{\kappa}{\sqrt{2}} \left(\partial_\alpha \chi\right) \tilde{F}^{\alpha\nu}. \tag{5.46}$$

Using the Lorentz gauge, Eq. 5.46 reduces to the following equation for the gauge field A_μ,

$$\Box A^\nu = \frac{\kappa}{\sqrt{2}} \left(\partial_\alpha \chi\right) \tilde{F}^{\alpha\nu}. \tag{5.47}$$

We fix the axes of propagation such that the plane wave solution for A_μ propagates along the z-direction i.e.

$$A^\mu = A_0^\mu e^{i\omega t - ikz}, \tag{5.48}$$

where the frequency, ω, and the wave-number, k, obey the dispersion relation

$$\omega = k \pm \frac{i\kappa}{2\sqrt{2}} \left(\partial_z \chi\right). \tag{5.49}$$

Fixing $A_0 = A_3 = 0$ for circularly polarized light and defining $A_\pm = A_1 \pm i A_2$ finally gives

$$\begin{aligned} A_\pm(t,z) = A_\pm\left(t', z'\right) \exp\Big[&-i\omega_\gamma\left(t - t'\right) + i\omega_\gamma\left(z - z'\right) \\ &\pm i \frac{\kappa}{2\sqrt{2}} \left(\partial_z \chi\right)\Big], \end{aligned} \tag{5.50}$$

where $\pm$ denotes the left and right circularly polarized light respectively. It's evident that the axion-photon interaction term produces a rotation of the electromagnetic wave by the angle $\Delta\Theta$ given by

$$\begin{aligned} \Delta\Theta &= \int dz \frac{\kappa}{2\sqrt{2}} \left(\partial_z \chi\right) \\ &= \frac{\kappa}{2\sqrt{2}} \left(\chi(z_{obs}) - \chi(z_{emit})\right) \\ &= -\frac{\kappa}{2\sqrt{2}} \chi(z_{emit}). \end{aligned} \tag{5.51}$$

Substituting the axion solution from Eq. 5.17 in Eq. 5.51, the angle of rotation turns out to be

$$\Delta\Theta = \frac{\alpha'}{32} \frac{Q^2 a}{GM} \frac{\cos\theta}{r^2 + a^2\cos^2\theta}. \tag{5.52}$$

The EHT results from the observation of M87* black hole do not include the polarimetric data at present. In [266], M87* BH is observed in four frequency bands and it is assumed in the analysis that the position polarization angle follows the λ^2 law (Faraday rotation). However, the large uncertainties in the data (see Tab. 5.1, data from [266]) indicate that the polarization is not necessarily due to the Faraday rotation. This can be the polarization arising from the photon-axion interaction since it is independent of the wavelength of the photon.

Frequency (ν GHz)	Polarization Angle ($\Delta\Theta$)
230.3	30.7 ± 2.2
232.3	31.6 ± 2.0
220.4	31.4 ± 1.9
218.4	27.3 ± 2.0

Table 5.1: The observed polarization angle for different frequencies taken from [266]. The observations suggest that the polarization angle is independent of the frequency and can be due to some intrinsic feature of the black hole.

Eq. 5.52 shows that the polarization of light by the axion hair of the KSBH is dependent on the inverse string tension α'. Assuming that the axion hair is the only source of polarization, we show the behavior of α' with the charge of the KSBH in Fig. 5.4. We use the average, 30.25 ± 2.02, of the four polarization angles in Tab. 5.1 in our estimation of α'. The $U(1)$ gauge kinetic term in Eq. 5.45 comes with a pre-factor of $\alpha'/(16\kappa^2)$ (having taken $e^{-\phi} \simeq 1$) that can be identified with $1/(4g^2)$ where g is the gauge coupling strength [47, 49, 321]. For the photon, this is just the electric charge e. Using this, we have:

$$\frac{\alpha'}{16\kappa^2} = \frac{1}{4e^2} \tag{5.53}$$

This corresponds to the horizontal line in Fig. 5.4 from where we can extract the value of electric charge present in the black hole.

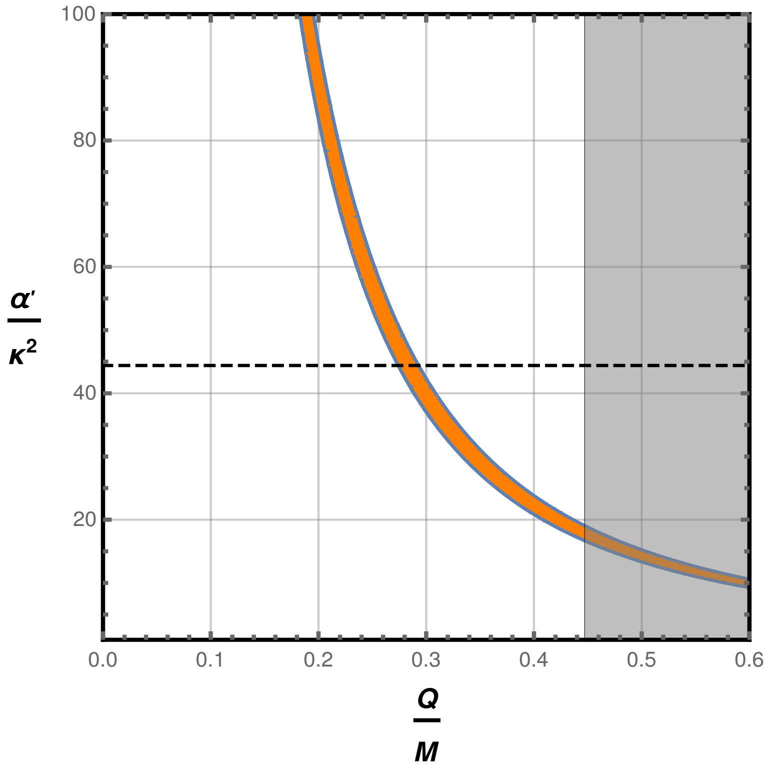

Figure 5.4: The variation of α'/κ^2 with the charge in the KSBH. The horizontal line marks the value of α' corresponding to the electromagnetic coupling e and the values of Q/M in the shaded region on the right are excluded for spin $a = 0.9M$ from the horizon regularity condition.

5.4 Discussion and Conclusion

In this chapter, we studied the features of the KSBH in light of the recent M87* black hole observations from EHT and studies of polarization of light coming from near the black hole. The KSBH is a rotating charged black hole solution arising from string theory. As reported by the EHT, the black hole shadow at an inclination angle of 17^0 is not completely circular with an experimental upper bound of 10% on the deviation from circularity, ΔC. Kerr black holes arising from general relativity cast highly circular shadows irrespective of the inclination angle leaving room for the M87* to be a non-Kerr black hole. We calculated the ΔC of the KSBH shadow using the observed M87* parameters from EHT in Sec. 5.2. We also found the rotation angle of the polarization of the circularly polarized light, $\Delta\Theta$, due to the axion hair of the KSBH in Sec. 5.3. Identifying the inverse string tension α' in terms of the electromagnetic coupling strength e in the relation for $\Delta\Theta$

$\frac{Q}{M}$	Inclination (θ in degrees)	Polarization Angle ($\Delta\Theta$ in degrees)	Deviation (ΔC)
0.1	10	1.54	0.00021
	30	1.34	0.00124
	50	0.99	0.00282
	70	0.53	0.00414
	90	0	0.00463
0.3	10	14.79	0.00018
	30	12.95	0.00136
	50	9.54	0.00310
	70	5.06	0.00453
	90	0	0.00507
0.5	10	47.56	0.00031
	30	41.60	0.00168
	50	30.64	0.00380
	70	16.25	0.00554
	90	0	0.00618
0.7	10	119.55	0.00030
	30	104.56	0.00242
	50	77.06	0.00545
	70	49.81	0.00786
	90	0	0.00874
0.9	10	301.29	0.00063
	30	265.01	0.00479
	50	195.64	0.01059
	70	103.59	0.01492
	90	0	0.01646

Table 5.2: The rotation angle of the polarization of circularly polarized light and the deviation from circularity of the BH shadows for various benchmark values of charge and inclination angle. The spin of the BH is fixed at $a = 0.5$ and $\alpha'/(16\kappa^2) = 1/(4e^2)$.

gives us the charge of the KSBH which can then be used to predict the ΔC of the KSBH shadow in a future precision experiment. Simultaneous observation of a constant $\Delta\Theta$ (independent of the frequency of light) and ΔC for a particular value of the spin of the black hole, its inclination angle, its mass and charge could be a signature of the KSBH and thus indirectly of the string theory. We give the expected values of $\Delta\Theta$ and ΔC for some benchmark values of the KSBH charge and its inclination angle in Tab. 5.2 for a BH spin of $a/M = 0.5$. As can be seen from the table, for values of the inclination angle other than 90^0, ($\theta \neq 90^0$), it's possible to make simultaneous observations of $\Delta\Theta$ and ΔC allowing the BH to be identified as a Kerr-Sen black hole.

There are three distinct features which can distinguish KSBH from a generic Kerr-Newman BH with axion hair:

- Although the charge of the KSBH is electric in nature it is sourced by the axion-photon coupling instead of the in-falling charged particles, such as electrons or positions as in the case of charged astrophysical BH like the KNBH.
- Owing to a different origin of charge, the KSBH can hold more of it than a KNBH. Q/M for KSBH can be upto 1.4 whereas for KNBH, it cannot exceed 1.
- In the KSBH, $\Delta\Theta$ and ΔC are correlated and the measurement of one yields the value of the other whereas in the KNBH these are independent observables.

Future, more precise, observations may be able to verify if a string solution exists in nature in the form of a Kerr-Sen black hole.

Chapter 6

Summary and Conclusions

Recent years have seen unprecedented advancement of observational as well as computational techniques and physical quantities are now calculated or inferred with unmatched accuracy. This development has happened at all fronts of the physical science. The works discussed in this thesis build upon establishing a connection between the precise observations and theoretical models in the context of astroparticle physics. We focus on three major constituents of the astroparticle physics: theories of elementary particles and their interactions, cosmological models and underlying theories of gravity. The widely accepted paradigms in these three sectors are Standard model of particle physics, ΛCDM (cold dark matter) model of cosmology and Einstein's theory of General relativity, respectively. Time and again these models and theories have proven their competency by explaining experimental observations and passing tests. However recent technological developments in measurements and computations have brought many shortcomings of these so-called standard theories into light. This thesis stands on the idea of searching for improvements over the standard theories in the light of the shortcomings discovered through recent precision measurements and observations. Ch. 1 discussed these standard theories in brief and in Ch. 2, we provided a collection of observations that hint towards the existence of physics beyond the standard picture.

In Ch. 3 we dealt with three issues which are there in the standard model of particle physics: (1) Observation of more than expected number of neutrino event in 1-3 PeV energy bins and non observation of Glashow resonance in 6-years IceCube data, (2) Generation of neutrino mass and (3) Particle nature of dark matter. We invoke a variant of

2HDM where we add right handed neutrinos to it and also impose Z_2 symmetry over second Higgs and the right handed neutrinos, hence the model is called ν2HDM. Power law flux of cosmic ray neutrinos (parametrized as $\phi_0 E_\nu^{-\gamma}$) undergoing standard model interactions at the IceCube fails in explaining the observed features of IceCube event spectrum. To resolve this anomaly, we proposed a phenomenon in which cosmic ray neutrinos interact with the cosmic neutrino background and as a result of this interactions the power law flux gets modified. The interaction structure of the ν2HDM allows one such process through t-channel via second neutral Higgs. In this t-channel process cosmic ray neutrinos interacting with cosmic neutrino background produce right handed neutrinos which cannot be detected at IceCube, hence suppressing the flux reaching at the IceCube detector. Tuning the parameters involved in the t-channel process within the range allowed by the vacuum stability of the ν2HDM we attain the suppression at the Glashow bins resulting in lesser events. The presence of this suppression makes it easier to fit the rest of the bins by adjusting ϕ_0 and γ of the flux and hence the whole event spectrum fits better than a simple power law flux. The full analysis with all the three neutrinos reveals that this t-channel process for each neutrino flavor produces one dip in the flux of the neutrino, hence in total there are three dips with positions (in energy) depending on the mass of the left handed neutrinos. This dependence gives rise to different suppression signatures for the normal mass hierarchy and inverted mass hierarchy. The neutrino mass in ν2HDM is generated by a low scale Type-I see-saw model enabled by the second neutral Higgs. In addition we extend ν2HDM by a singlet scalar as a candidate for dark matter. The same second neutral Higgs which helps in suppressing the neutrino flux and generating the neutrino mass also enables the dark matter annihilation to produce the correct relic density and also assists in generating self interaction of the DM of the strength allowed by the N-body simulations of the structure formation. In future more and precise data (above 6 PeV energy) from the IceCube or similar experiments can confirm the flux suppression hypothesis by observing the unique signature of neutrino mass hierarchy. This can also confirm the correct neutrino mass hierarchy. Additionally, this model can also be tested in the context of secret neutrino interaction using the present and future cosmological data, lepton flavor violating processes, leptogenesis and non-standard neutrino interactions. The effects of heavy right handed neutrinos can also be observed at the proposed Future Circular Collider.

In Ch. 4 we study two dark energy models (1) Hu-Sawicki $f(R)$ gravity model and (2) Dynamical dark energy model in the light of σ_8-Ω_m and H_0-Ω_m tension between the early and the late Universe observations. We also explored the effect of massive neutrinos on the structure formation in these two models along with the standard ΛCDM model. We did a comparative analyses of ΛCDM model, Hu-Sawicki model and the dynamical dark energy model with constant as well as free $\sum m_\nu$. We found that in all three models the H_0-Ω_m tension is resolved just by including the massive neutrinos. But in ΛCDM model the σ_8-Ω_m tension got worse by the inclusion of massive neutrinos. Hence to solve both the discrepancies together we turn towards other dark energy models. We found that simultaneous resolution of both the discrepancies prefers dynamical dark energy model over other two models. We would like to mention that even thought the mismatch is not fully resolved in DDE model, the agreement between the CMB and LSS observations is better in this model comparatively. This comparative result holds for both fixed and free $\sum m_\nu$. In future more precise observations from the upcoming cosmological can help deciding between these dark energy models. The current experiment like Dark Energy Survey (DES). EUCLID [104] and the future experiments like WFIRST [103] will measure the distance ladder more precisely and hence the expansion rate of the Universe, leading to better tests of the dark energy models.

In Ch. 5 we test the Kerr-Sen metric against the black hole shadow observations by the Event Horizon telescope. The Kerr-Sen black hole, predicted by the 4-D effective heterotic string theory, is a rotating charged black hole with 4 bosonic fields: a $U(1)$ gauge boson, a Kalb-Ramond 3-form which is equivalent to a pseudo scalar axion in 4-dimensions, the dilaton and the graviton. We use the shadow observation by EHT and an earlier polarimetric measurement of the M87* to constrain the parameters of Kerr-Sen metric and in-turn provide a unique signature of the Kerr-Sen black hole which distinguishes it from other rotating charged black holes. The identification of the $U(1)$ charge of the black hole in terms of the photon coupling leads to a correlated prediction for a frequency independent Faraday rotation and the deviation from circularity of the black hole shadow. Similar measurements of the Kerr-Newman black hole with axion hair have no correlation with the shape of the image and the amount of polarization angle rotation. In the EHT observation of M87* shadow, the deviation from circularity has an upper bound of 10%. In our analysis we conclude that if this observation is refined to 1% accuracy then a definitive prediction of the charge of the Kerr-Sen black hole and the Faraday rotation can be made. Also, using the formalism described in this thesis, the Kerr-Sen metric can be put to test every time a new black image observation along with polarimetric observation takes place. The correlation among image and polarimetric observation is distinctive test of the Kerr-Sen metric and an indirect affirmation for string theory. Additionally, the string tension parameter α' can also constrained through other string phenomenological studies, for example, in the context of cosmological parameter estimation in string cosmology models.

In conclusion of the work done in this thesis, we find that recent observations and measurements may lead us towards new theories in physics. The novel precision measurement experiments such as IceCube, Planck, EHT play a crucial role in checking these new theories beyond the standard picture. However, the analyses done in this thesis suggest that more and better data is needed to select the one true theory.

Bibliography

[1] S. Glashow, *Partial Symmetries of Weak Interactions,* Nucl. Phys. **22**, 579–588 (1961).

[2] S. Weinberg, *A Model of Leptons,* Phys. Rev. Lett. **19**, 1264–1266 (1967).

[3] A. Salam, *Weak and Electromagnetic Interactions,* Conf. Proc. C **680519**, 367–377 (1968).

[4] R. Abbasi *et al.*, *The IceCube Data Acquisition System: Signal Capture, Digitization, and Timestamping,* Nucl. Instrum. Meth. A **601**, 294–316 (2009).

[5] S. Adrian-Martinez *et al.*, *Searches for Point-like and extended neutrino sources close to the Galactic Centre using the ANTARES neutrino Telescope,* Astrophys. J. Lett. **786**, L5 (2014).

[6] S. Barwick *et al.*, *Constraints on cosmic neutrino fluxes from the anita experiment,* Phys. Rev. Lett. **96**, 171101 (2006).

[7] A. Anker, P. Baldi, S. W. Barwick, D. Bergman, H. Bernhoff, D. Z. Besson, N. Bingefors, O. Botner, P. Chen, Y. Chen, D. García-Fernández, G. Gaswint, C. Glaser, A. Hallgren, J. C. Hanson, J. J. Huang, S. R. Klein, S. A. Kleinfelder, C. Y. Kuo, R. Lahmann, U. Latif, T. Liu, Y. Lyu, S. McAleer, J. Nam, A. Novikov, A. Nelles, M. P. Paul, C. Persichilli, I. Plaisier, J. Y. Shiao, J. Tatar, A. van Vliet, S. H. Wang, Y. H. Wang, and C. Welling, *White Paper: ARIANNA-200 high energy neutrino telescope,* arXiv e-prints arXiv:2004.09841 (2020).

[8] A. H. Guth, *The Inflationary Universe: A Possible Solution to the Horizon and Flatness Problems,* Adv. Ser. Astrophys. Cosmol. **3**, 139–148 (1987).

[9] A. D. Linde, *A New Inflationary Universe Scenario: A Possible Solution of the Horizon, Flatness, Homogeneity, Isotropy and Primordial Monopole Problems,* Adv. Ser. Astrophys. Cosmol. **3**, 149–153 (1987).

[10] V. F. Mukhanov and G. V. Chibisov, *Quantum Fluctuations and a Nonsingular Universe,* JETP Lett. **33**, 532–535 (1981).

[11] A. A. Starobinsky, *Dynamics of Phase Transition in the New Inflationary Universe Scenario and Generation of Perturbations,* Phys. Lett. B **117**, 175–178 (1982).

[12] S. Hawking, *The Development of Irregularities in a Single Bubble Inflationary Universe,* Phys. Lett. B **115**, 295 (1982).

[13] A. Albrecht and P. J. Steinhardt, *Cosmology for Grand Unified Theories with Radiatively Induced Symmetry Breaking,* Adv. Ser. Astrophys. Cosmol. **3**, 158–161 (1987).

[14] F. Lucchin and S. Matarrese, *Power Law Inflation,* Phys. Rev. D **32**, 1316 (1985).

[15] V. F. Mukhanov, H. Feldman, and R. H. Brandenberger, *Theory of cosmological perturbations. Part 1. Classical perturbations. Part 2. Quantum theory of perturbations. Part 3. Extensions,* Phys. Rept. **215**, 203–333 (1992).

[16] B. P. Abbott *et al.*, *Observation of Gravitational Waves from a Binary Black Hole Merger,* Phys. Rev. Lett. **116**, 061102 (2016).

[17] B. P. Abbott *et al.*, *GWTC-1: A Gravitational-Wave Transient Catalog of Compact Binary Mergers Observed by LIGO and Virgo during the First and Second Observing Runs,* Phys. Rev. **X9**, 031040 (2019).

[18] K. Akiyama *et al.*, *First M87 Event Horizon Telescope Results. I. The Shadow of the Supermassive Black Hole,* Astrophys. J. **875**, L1 (2019).

[19] K. Akiyama *et al.*, *First M87 Event Horizon Telescope Results. VI. The Shadow and Mass of the Central Black Hole,* Astrophys. J. **875**, L6 (2019).

[20] K. Akiyama *et al.*, *First M87 Event Horizon Telescope Results. V. Physical Origin of the Asymmetric Ring,* Astrophys. J. **875**, L5 (2019).

[21] K. Akiyama *et al.*, *First M87 Event Horizon Telescope Results. IV. Imaging the Central Supermassive Black Hole,* Astrophys. J. **875**, L4 (2019).

[22] K. Akiyama *et al.*, *First M87 Event Horizon Telescope Results. II. Array and Instrumentation,* Astrophys. J. **875**, L2 (2019).

[23] K. Akiyama *et al.*, *First M87 Event Horizon Telescope Results. III. Data Processing and Calibration,* Astrophys. J. **875**, L3 (2019).

[24] R. Penrose, *Gravitational collapse and space-time singularities,* Phys. Rev. Lett. **14**, 57–59 (1965).

[25] S. W. Hawking, *Breakdown of predictability in gravitational collapse,* Phys. Rev. D **14**, 2460–2473 (1976).

[26] D. Christodoulou, *The formation of black holes and singularities in spherically symmetric gravitational collapse,* Communications on Pure and Applied Mathematics **44**, 339–373 (1991).

[27] C. Rovelli, *Black hole entropy from loop quantum gravity,* Phys. Rev. Lett. **77**, 3288–3291 (1996).

[28] F. Dowker, *Causal sets and the deep structure of spacetime* (2005), pp. 445–464.

[29] A. Ashtekar, T. Pawlowski, and P. Singh, *Quantum nature of the big bang,* Phys. Rev. Lett. **96**, 141301 (2006).

[30] D. Kothawala, *Minimal Length and Small Scale Structure of Spacetime,* Phys. Rev. D **88**, 104029 (2013).

[31] S. Nojiri, S. D. Odintsov, and V. K. Oikonomou, *Modified Gravity Theories on a Nutshell: Inflation, Bounce and Late-time Evolution,* Phys. Rept. **692**, 1–104 (2017).

[32] S. Nojiri and S. D. Odintsov, *Unified cosmic history in modified gravity: from F(R) theory to Lorentz non-invariant models,* Phys. Rept. **505**, 59–144 (2011).

[33] S. Capozziello, S. Nojiri, S. Odintsov, and A. Troisi, *Cosmological viability of f(R)-gravity as an ideal fluid and its compatibility with a matter dominated phase,* Phys. Lett. B **639**, 135–143 (2006).

[34] T. Padmanabhan and D. Kothawala, *Lanczos-Lovelock models of gravity,* Phys. Rept. **531**, 115–171 (2013).

[35] C. Charmousis and M. Tsoukalas, *Lovelock Galileons and black holes,* Phys. Rev. D **92**, 104050 (2015).

[36] T. Shiromizu, K.-i. Maeda, and M. Sasaki, *The Einstein equation on the 3-brane world,* Phys. Rev. D **62**, 024012 (2000).

[37] N. Dadhich, R. Maartens, P. Papadopoulos, and V. Rezania, *Black holes on the brane,* Phys. Lett. B **487**, 1–6 (2000).

[38] T. Harko and M. Mak, *Vacuum solutions of the gravitational field equations in the brane world model,* Phys. Rev. D **69**, 064020 (2004).

[39] T. Kobayashi, T. Shiromizu, and N. Deruelle, *Low energy effective gravitational equations on a Gauss-Bonnet brane,* Phys. Rev. D **74**, 104031 (2006).

[40] T. Carames, M. Guimaraes, and J. Hoff da Silva, *Effective gravitational equations for $f(R)$ braneworld models,* Phys. Rev. D **87**, 106011 (2013).

[41] S. Chakraborty and S. SenGupta, *Spherically symmetric brane spacetime with bulk $f(\mathcal{R})$ gravity,* Eur. Phys. J. C **75**, 11 (2015).

[42] G. W. Horndeski, *Second-order scalar-tensor field equations in a four-dimensional space,* Int. J. Theor. Phys. **10**, 363–384 (1974).

[43] T. P. Sotiriou and S.-Y. Zhou, *Black hole hair in generalized scalar-tensor gravity,* Phys. Rev. Lett. **112**, 251102 (2014).

[44] E. Babichev, C. Charmousis, and A. Lehbel, *Black holes and stars in Horndeski theory,* Class. Quant. Grav. **33**, 154002 (2016).

[45] P. Horava and E. Witten, *Heterotic and type I string dynamics from eleven-dimensions,* Nucl. Phys. B **460**, 506–524 (1996).

[46] P. Horava and E. Witten, *Eleven-dimensional supergravity on a manifold with boundary,* Nucl. Phys. B **475**, 94–114 (1996).

[47] J. Polchinski, *String theory. Vol. 1: An introduction to the bosonic string*, Cambridge Monographs on Mathematical Physics (Cambridge University Press, 2007).

[48] J. Polchinski, *String theory. Vol. 2: Superstring theory and beyond*, Cambridge Monographs on Mathematical Physics (Cambridge University Press, 2007).

[49] M. B. Green, J. H. Schwarz, and E. Witten, *Superstring Theory Vol. 2*, Cambridge Monographs on Mathematical Physics (Cambridge University Press, 2012).

[50] Y. Fukuda *et al.*, *Evidence for oscillation of atmospheric neutrinos,* Phys. Rev. Lett. **81**, 1562–1567 (1998).

[51] P. Ade *et al.*, *Planck 2013 results. XVI. Cosmological parameters,* Astron. Astrophys. **571**, A16 (2014).

[52] R. A. Battye, T. Charnock, and A. Moss, *Tension between the power spectrum of density perturbations measured on large and small scales,* Phys. Rev. **D91**, 103508 (2015).

[53] H. Velten, R. vom Marttens, and W. Zimdahl, *Aspects of the cosmological "coincidence problem",* Eur. Phys. J. C **74**, 3160 (2014).

[54] IceCube Neutrino Observatory `https://icecube.wisc.edu/`.

[55] R. Gandhi, C. Quigg, M. H. Reno, and I. Sarcevic, *Ultrahigh-energy neutrino interactions,* Astropart. Phys. **5**, 81–110 (1996).

[56] S. L. Glashow, *Resonant scattering of antineutrinos,* Phys. Rev. **118**, 316–317 (1960).

[57] M. G. Aartsen *et al.*, *Evidence for Astrophysical Muon Neutrinos from the Northern Sky with IceCube,* Phys. Rev. Lett. **115**, 081102 (2015).

[58] I. Cholis and D. Hooper, *On The Origin of IceCube's PeV Neutrinos,* JCAP **1306**, 030 (2013).

[59] L. A. Anchordoqui *et al.*, *Cosmic Neutrino Pevatrons: A Brand New Pathway to Astronomy, Astrophysics, and Particle Physics,* JHEAp **1-2**, 1–30 (2014).

[60] K. Murase, *On the Origin of High-Energy Cosmic Neutrinos,* AIP Conf. Proc. **1666**, 040006 (2015).

[61] S. Sahu and L. S. Miranda, *Some possible sources of IceCube TeVPeV neutrino events,* Eur. Phys. J. **C75**, 273 (2015).

[62] M. G. Aartsen *et al.*, *Multimessenger observations of a flaring blazar coincident with high-energy neutrino IceCube-170922A,* Science **361**, eaat1378 (2018).

[63] M. G. Aartsen *et al.*, *Neutrino emission from the direction of the blazar TXS 0506+056 prior to the IceCube-170922A alert,* Science **361**, 147–151 (2018).

[64] P. Meszaros, *Astrophysical Sources of High Energy Neutrinos in the IceCube Era,* Ann. Rev. Nucl. Part. Sci. **67**, 45–67 (2017).

[65] A. Esmaili and P. D. Serpico, *Are IceCube neutrinos unveiling PeV-scale decaying dark matter?* JCAP **1311**, 054 (2013).

[66] K. Murase, R. Laha, S. Ando, and M. Ahlers, *Testing the Dark Matter Scenario for PeV Neutrinos Observed in IceCube,* Phys. Rev. Lett. **115**, 071301 (2015).

[67] P. S. B. Dev, D. Kazanas, R. N. Mohapatra, V. L. Teplitz, and Y. Zhang, *Heavy right-handed neutrino dark matter and PeV neutrinos at IceCube,* JCAP **1608**, 034 (2016).

[68] A. Bhattacharya, R. Gandhi, and A. Gupta, *The Direct Detection of Boosted Dark Matter at High Energies and PeV events at IceCube,* JCAP **1503**, 027 (2015).

[69] D. Borah, A. Dasgupta, U. K. Dey, S. Patra, and G. Tomar, *Multi-component Fermionic Dark Matter and IceCube PeV scale Neutrinos in Left-Right Model with Gauge Unification,* JHEP **09**, 005 (2017).

[70] V. Barger and W.-Y. Keung, *Superheavy Particle Origin of IceCube PeV Neutrino Events,* Phys. Lett. **B727**, 190–193 (2013).

[71] B. Dutta, Y. Gao, T. Li, C. Rott, and L. E. Strigari, *Leptoquark implication from the CMS and IceCube experiments,* Phys. Rev. **D91**, 125015 (2015).

[72] U. K. Dey and S. Mohanty, *Constraints on Leptoquark Models from IceCube Data,* JHEP **04**, 187 (2016).

[73] B. Chauhan, B. Kindra, and A. Narang, *Discrepancies in simultaneous explanation of flavor anomalies and IceCube PeV events using leptoquarks,* Phys. Rev. **D97**, 095007 (2018).

[74] U. K. Dey, D. Kar, M. Mitra, M. Spannowsky, and A. C. Vincent, *Searching for Leptoquarks at IceCube and the LHC,* Phys. Rev. **D98**, 035014 (2018).

[75] P. S. B. Dev, D. K. Ghosh, and W. Rodejohann, *R-parity Violating Supersymmetry at IceCube,* Phys. Lett. **B762**, 116–123 (2016).

[76] V. S. Berezinsky and A. Z. Gazizov, *Cosmic neutrino and the possibility of Searching for W bosons with masses 30-100 GeV in underwater experiments,* JETP Lett. **25**, 254–256 (1977). [Pisma Zh. Eksp. Teor. Fiz.25,276(1977)].

[77] V. S. Berezinsky and A. Z. Gazizov, *Neutrino - electron scattering at energies above the W boson production threshold,* Sov. J. Nucl. Phys. **33**, 120–125 (1981). [Yad. Fiz.33,230(1981)].

[78] S. Sahu and B. Zhang, *On the non-detection of Glashow resonance in IceCube,* JHEAp **18**, 1–4 (2018).

[79] M. D. Kistler and R. Laha, *Multi-PeV Signals from a New Astrophysical Neutrino Flux Beyond the Glashow Resonance,* Phys. Rev. Lett. **120**, 241105 (2018).

[80] A. Bhattacharya, R. Gandhi, W. Rodejohann, and A. Watanabe, *The Glashow resonance at IceCube: signatures, event rates and pp vs. $p\gamma$ interactions,* JCAP **1110**, 017 (2011).

[81] A. S. Joshipura, S. Mohanty, and S. Pakvasa, *Pseudo-Dirac neutrinos via a mirror world and depletion of ultrahigh energy neutrinos,* Phys. Rev. **D89**, 033003 (2014).

[82] S. Pakvasa, A. Joshipura, and S. Mohanty, *Explanation for the low flux of high energy astrophysical muon-neutrinos,* Phys. Rev. Lett. **110**, 171802 (2013).

[83] G. Tomar, S. Mohanty, and S. Pakvasa, *Lorentz Invariance Violation and IceCube Neutrino Events,* JHEP **11**, 022 (2015).

[84] L. A. Anchordoqui, V. Barger, H. Goldberg, J. G. Learned, D. Marfatia, S. Pakvasa, T. C. Paul, and T. J. Weiler, *End of the cosmic neutrino energy spectrum,* Phys. Lett. **B739**, 99–101 (2014).

[85] J. Liao and D. Marfatia, *IceCubes astrophysical neutrino energy spectrum from CPT violation,* Phys. Rev. **D97**, 041302 (2018).

[86] B. Pontecorvo, *Mesonium and anti-mesonium,* Sov. Phys. JETP **6**, 429 (1957).

[87] S. Bilenky, *On the phenomenology of neutrino oscillations in vacuum,* (2012).

[88] S. Bilenky, *Some comments on high precision study of neutrino oscillations,* Phys. Part. Nucl. Lett. **12**, 453–461 (2015).

[89] Q. R. Ahmad *et al.*, *Measurement of the rate of $\nu_e + d \to p + p + e^-$ interactions produced by ^8B solar neutrinos at the Sudbury Neutrino Observatory,* Phys. Rev. Lett. **87**, 071301 (2001).

[90] S. Bilenky, *On atmospheric neutrino mass-squared difference in the precision era,* (2015).

[91] L. Wolfenstein, *Neutrino Oscillations in Matter,* Phys. Rev. D **17**, 2369–2374 (1978).

[92] S. Mikheyev and A. Smirnov, *Resonance Amplification of Oscillations in Matter and Spectroscopy of Solar Neutrinos,* Sov. J. Nucl. Phys. **42**, 913–917 (1985).

[93] S. Mikheev and A. Smirnov, *Resonant amplification of neutrino oscillations in matter and solar neutrino spectroscopy,* Nuovo Cim. C **9**, 17–26 (1986).

[94] H. Bethe, *A Possible Explanation of the Solar Neutrino Puzzle,* Phys. Rev. Lett. **56**, 1305 (1986).

[95] C. Giunti and C. W. Kim, *Fundamentals of Neutrino Physics and Astrophysics* (2007).

[96] P. A. R. Ade *et al.*, *Planck 2015 results. XIII. Cosmological parameters,* Astron. Astrophys. **594**, A13 (2016).

[97] M. Betoule *et al.*, *Improved cosmological constraints from a joint analysis of the SDSS-II and SNLS supernova samples,* Astron. Astrophys. **568**, A22 (2014).

[98] L. Anderson *et al.*, *The clustering of galaxies in the SDSS-III Baryon Oscillation Spectroscopic Survey: baryon acoustic oscillations in the Data Releases 10 and 11 Galaxy samples,* Mon. Not. Roy. Astron. Soc. **441**, 24–62 (2014).

[99] F. Beutler, C. Blake, M. Colless, D. H. Jones, L. Staveley-Smith, L. Campbell, Q. Parker, W. Saunders, and F. Watson, *The 6dF Galaxy Survey: baryon acoustic oscillations and the local Hubble constant,* MNRAS**416**, 3017–3032 (2011).

[100] A. J. Ross, L. Samushia, C. Howlett, W. J. Percival, A. Burden, and M. Manera, *The clustering of the SDSS DR7 main Galaxy sample I. A 4 per cent distance measure at* $z = 0.15$*,* Mon. Not. Roy. Astron. Soc. **449**, 835–847 (2015).

[101] N. Palanque-Delabrouille *et al.*, *Constraint on neutrino masses from SDSS-III/BOSS Ly*α *forest and other cosmological probes,* JCAP **02**, 045 (2015).

[102] http://www.lsst.org.

[103] http://wfirst.gsfc.nasa.gov.

[104] http://sci.esa.int/euclid.

[105] http://www.simonsobservatory.org.

[106] https://cmb-s4.org.

[107] P. Minkowski, $\mu \to e\gamma$ *at a Rate of One Out of* 10^9 *Muon Decays?* Phys. Lett. B **67**, 421–428 (1977).

[108] M. Gell-Mann, P. Ramond, and R. Slansky, *Complex Spinors and Unified Theories,* Conf. Proc. C **790927**, 315–321 (1979).

[109] R. N. Mohapatra and G. Senjanović, *Neutrino mass and spontaneous parity non-conservation,* Phys. Rev. Lett. **44**, 912–915 (1980).

[110] J. Schechter and J. W. F. Valle, *Neutrino masses in su(2) $\bigotimes$ u(1) theories,* Phys. Rev. D **22**, 2227–2235 (1980).

[111] G. Lazarides, Q. Shafi, and C. Wetterich, *Proton Lifetime and Fermion Masses in an SO(10) Model,* Nucl. Phys. B **181**, 287–300 (1981).

[112] R. N. Mohapatra and G. Senjanović, *Neutrino masses and mixings in gauge models with spontaneous parity violation,* Phys. Rev. D **23**, 165–180 (1981).

[113] R. Foot, H. Lew, X. He, and G. C. Joshi, *Seesaw Neutrino Masses Induced by a Triplet of Leptons,* Z. Phys. C **44**, 441 (1989).

[114] F. Zwicky, *Die Rotverschiebung von extragalaktischen Nebeln,* Helv. Phys. Acta **6**, 110–127 (1933). [Gen. Rel. Grav.41,207(2009)].

[115] H. W. Babcock, *The rotation of the Andromeda Nebula,* Lick Observatory Bulletin **498**, 41–51 (1939).

[116] V. C. Rubin and W. K. Ford, Jr., *Rotation of the Andromeda Nebula from a Spectroscopic Survey of Emission Regions,* Astrophys. J. **159**, 379–403 (1970).

[117] M. S. Roberts and R. N. Whitehurst, *The rotation curve and geometry of M31 at large galactocentric distances.* ApJ**201**, 327–346 (1975).

[118] V. Rubin, N. Thonnard, and J. Ford, W.K., *Rotational properties of 21 SC galaxies with a large range of luminosities and radii, from NGC 4605 /R = 4kpc/ to UGC 2885 /R = 122 kpc/,* Astrophys. J. **238**, 471 (1980).

[119] A. Taylor, S. Dye, T. J. Broadhurst, N. Benitez, and E. van Kampen, *Gravitational lens magnification and the mass of abell 1689,* Astrophys. J. **501**, 539 (1998).

[120] E. Corbelli and P. Salucci, *The Extended Rotation Curve and the Dark Matter Halo of M33,* Mon. Not. Roy. Astron. Soc. **311**, 441–447 (2000).

[121] H. Baer, K.-Y. Choi, J. E. Kim, and L. Roszkowski, *Dark matter production in the early Universe: beyond the thermal WIMP paradigm,* Phys. Rept. **555**, 1–60 (2015).

[122] D. Akerib *et al.*, *Limits on spin-dependent WIMP-nucleon cross section obtained from the complete LUX exposure,* Phys. Rev. Lett. **118**, 251302 (2017).

[123] E. Aprile *et al.*, *Constraining the spin-dependent WIMP-nucleon cross sections with XENON1T,* Phys. Rev. Lett. **122**, 141301 (2019).

[124] W. J. G. de Blok, *The Core-Cusp Problem,* Advances in Astronomy **2010**, 789293 (2010).

[125] A. A. Klypin, A. V. Kravtsov, O. Valenzuela, and F. Prada, *Where are the missing Galactic satellites?* Astrophys. J. **522**, 82–92 (1999).

[126] M. Boylan-Kolchin, J. S. Bullock, and M. Kaplinghat, *Too big to fail? The puzzling darkness of massive Milky Way subhaloes,* MNRAS**415**, L40–L44 (2011).

[127] https://www.nasa.gov/mission_pages/planck.

[128] N. Aghanim *et al.*, *Planck 2018 results. VI. Cosmological parameters,* (2018).

[129] A. G. Riess, L. Macri, S. Casertano, H. Lampeitl, H. C. Ferguson, A. V. Filippenko, S. W. Jha, W. Li, and R. Chornock, *A 3% Solution: Determination of the Hubble Constant with the Hubble Space Telescope and Wide Field Camera 3,* Astrophys. J. **730**, 119 (2011). [Erratum: Astrophys.J. 732, 129 (2011)].

[130] A. G. Riess *et al.*, *A 2.4% Determination of the Local Value of the Hubble Constant,* Astrophys. J. **826**, 56 (2016).

[131] A. G. Riess *et al.*, *Milky Way Cepheid Standards for Measuring Cosmic Distances and Application to Gaia DR2: Implications for the Hubble Constant,* Astrophys. J. **861**, 126 (2018).

[132] H. Hildebrandt *et al.*, *KiDS-450: Cosmological parameter constraints from tomographic weak gravitational lensing,* Mon. Not. Roy. Astron. Soc. **465**, 1454 (2017).

[133] K. Kuijken *et al.*, *Gravitational Lensing Analysis of the Kilo Degree Survey,* Mon. Not. Roy. Astron. Soc. **454**, 3500–3532 (2015).

[134] I. Fenech Conti, R. Herbonnet, H. Hoekstra, J. Merten, L. Miller, and M. Viola, *Calibration of weak-lensing shear in the Kilo-Degree Survey,* Mon. Not. Roy. Astron. Soc. **467**, 1627–1651 (2017).

[135] C. Heymans, L. Van Waerbeke, L. Miller, T. Erben, H. Hildebrandt, H. Hoekstra, T. D. Kitching, Y. Mellier, P. Simon, C. Bonnett, J. Coupon, L. Fu, J. Harnois Déraps, M. J. Hudson, M. Kilbinger, K. Kuijken, B. Rowe, T. Schrabback, E. Semboloni, E. van Uitert, S. Vafaei, and M. Velander, *CFHTLenS: the Canada-France-Hawaii Telescope Lensing Survey,* MNRAS**427**, 146–166 (2012).

[136] T. Erben, H. Hildebrandt, L. Miller, L. van Waerbeke, C. Heymans, H. Hoekstra, T. D. Kitching, Y. Mellier, J. Benjamin, C. Blake, C. Bonnett, O. Cordes, J. Coupon, L. Fu, R. Gavazzi, B. Gillis, E. Grocutt, S. D. J. Gwyn, K. Holhjem, M. J. Hudson, M. Kilbinger, K. Kuijken, M. Milkeraitis, B. T. P. Rowe, T. Schrabback, E. Semboloni, P. Simon, M. Smit, O. Toader, S. Vafaei, E. van Uitert, and M. Velander, *CFHTLenS: the Canada-France-Hawaii Telescope Lensing Survey - imaging data and catalogue products,* MNRAS**433**, 2545–2563 (2013).

[137] S. Joudaki *et al.*, *CFHTLenS revisited: assessing concordance with Planck including astrophysical systematics,* Mon. Not. Roy. Astron. Soc. **465**, 2033–2052 (2017).

[138] N. Aghanim *et al.*, *Planck intermediate results. LI. Features in the cosmic microwave background temperature power spectrum and shifts in cosmological parameters,* Astron. Astrophys. **607**, A95 (2017).

[139] G. Addison, Y. Huang, D. Watts, C. Bennett, M. Halpern, G. Hinshaw, and J. Weiland, *Quantifying discordance in the 2015 Planck CMB spectrum,* Astrophys. J. **818**, 132 (2016).

[140] A. Vikhlinin *et al.*, *Chandra Cluster Cosmology Project III: Cosmological Parameter Constraints,* Astrophys. J. **692**, 1060–1074 (2009).

[141] E. Macaulay, I. K. Wehus, and H. K. Eriksen, *Lower Growth Rate from Recent Redshift Space Distortion Measurements than Expected from Planck,* Phys. Rev. Lett. **111**, 161301 (2013).

[142] N. MacCrann, J. Zuntz, S. Bridle, B. Jain, and M. R. Becker, *Cosmic Discordance: Are Planck CMB and CFHTLenS weak lensing measurements out of tune?* Mon. Not. Roy. Astron. Soc. **451**, 2877–2888 (2015).

[143] K. Aylor *et al.*, *A Comparison of Cosmological Parameters Determined from CMB Temperature Power Spectra from the South Pole Telescope and the Planck Satellite,* (2017).

[144] M. Raveri, *Are cosmological data sets consistent with each other within the Λ cold dark matter model?* Phys. Rev. **D93**, 043522 (2016).

[145] W. Lin and M. Ishak, *Cosmological discordances: A new measure, marginalization effects, and application to geometry versus growth current data sets,* Phys. Rev. **D96**, 023532 (2017).

[146] F. Beutler, C. Blake, M. Colless, D. H. Jones, L. Staveley-Smith, L. Campbell, Q. Parker, W. Saunders, and F. Watson, *The 6dF Galaxy Survey: Baryon Acoustic Oscillations and the Local Hubble Constant,* Mon. Not. Roy. Astron. Soc. **416**, 3017–3032 (2011).

[147] A. Font-Ribera *et al.*, *Quasar-Lyman α Forest Cross-Correlation from BOSS DR11 : Baryon Acoustic Oscillations,* JCAP **1405**, 027 (2014).

[148] P. A. R. Ade *et al.*, *Planck 2013 results. XX. Cosmology from SunyaevZeldovich cluster counts,* Astron. Astrophys. **571**, A20 (2014).

[149] M. Kilbinger *et al.*, *CFHTLenS: Combined probe cosmological model comparison using 2D weak gravitational lensing,* Mon. Not. Roy. Astron. Soc. **430**, 2200–2220 (2013).

[150] C. Heymans *et al.*, *CFHTLenS tomographic weak lensing cosmological parameter constraints: Mitigating the impact of intrinsic galaxy alignments,* Mon. Not. Roy. Astron. Soc. **432**, 2433 (2013).

[151] P. A. R. Ade *et al.*, *Planck 2013 results. XVII. Gravitational lensing by large-scale structure,* Astron. Astrophys. **571**, A17 (2014).

[152] K. K. Schaffer *et al.*, *The First Public Release of South Pole Telescope Data: Maps of a 95-square-degree Field from 2008 Observations,* Astrophys. J. **743**, 90 (2011).

[153] A. van Engelen *et al.*, *A measurement of gravitational lensing of the microwave background using South Pole Telescope data,* Astrophys. J. **756**, 142 (2012).

[154] F. Beutler *et al.*, *The clustering of galaxies in the SDSS-III Baryon Oscillation Spectroscopic Survey: Testing gravity with redshift-space distortions using the power spectrum multipoles,* Mon. Not. Roy. Astron. Soc. **443**, 1065–1089 (2014).

[155] Z. Pan, L. Knox, and M. White, *Dependence of the Cosmic Microwave Background Lensing Power Spectrum on the Matter Density,* Mon. Not. Roy. Astron. Soc. **445**, 2941–2945 (2014).

[156] P. A. R. Ade *et al.*, *Planck 2015 results. XV. Gravitational lensing,* Astron. Astrophys. **594**, A15 (2016).

[157] B. A. Bassett and R. Hlozek, *Baryon Acoustic Oscillations,* (2009).

[158] I. G. Mccarthy, S. Bird, J. Schaye, J. Harnois-Deraps, A. S. Font, and L. Van Waerbeke, *The BAHAMAS project: the CMB–large-scale structure tension and the roles of massive neutrinos and galaxy formation,* Mon. Not. Roy. Astron. Soc. **476**, 2999–3030 (2018).

[159] G. Efstathiou, *H0 Revisited,* Mon. Not. Roy. Astron. Soc. **440**, 1138–1152 (2014).

[160] T. Shanks, L. Hogarth, and N. Metcalfe, *Gaia Cepheid parallaxes and 'Local Hole' relieve H_0 tension,* Mon. Not. Roy. Astron. Soc. **484**, L64–L68 (2019).

[161] A. G. Riess, S. Casertano, D. Kenworthy, D. Scolnic, and L. Macri, *Seven Problems with the Claims Related to the Hubble Tension in arXiv:1810.02595,* (2018).

[162] J. Soltis, A. Farahi, D. Huterer, and C. M. Liberato, *Percent-Level Test of Isotropic Expansion Using Type Ia Supernovae,* Phys. Rev. Lett. **122**, 091301 (2019).

[163] V. Poulin, T. L. Smith, T. Karwal, and M. Kamionkowski, *Early Dark Energy can Resolve the Hubble Tension,* Phys. Rev. Lett.**122**, 221301 (2019).

[164] T. Karwal and M. Kamionkowski, *Dark energy at early times, the Hubble parameter, and the string axiverse,* Phys. Rev. D **94**, 103523 (2016).

[165] A. Bhattacharyya, U. Alam, K. Lal Pandey, S. Das, and S. Pal, *Are H_0 and σ_8 Tensions Generic to Present Cosmological Data?* ApJ**876**, 143 (2019).

[166] V. Poulin, K. K. Boddy, S. Bird, and M. Kamionkowski, *Implications of an extended dark energy cosmology with massive neutrinos for cosmological tensions,* Phys. Rev. D**97**, 123504 (2018).

[167] E. Di Valentino, A. Melchiorri, E. V. Linder, and J. Silk, *Constraining dark energy dynamics in extended parameter space,* Phys. Rev. D**96**, 023523 (2017).

[168] E. Di Valentino, A. Melchiorri, and J. Silk, *Reconciling Planck with the local value of H_0 in extended parameter space,* Physics Letters B **761**, 242–246 (2016).

[169] E. Di Valentino, A. Melchiorri, and J. Silk, *Beyond six parameters: Extending Λ CDM,* Phys. Rev. D**92**, 121302 (2015).

[170] K. Ichikawa, M. Kawasaki, K. Nakayama, M. Senami, and F. Takahashi, *Increasing effective number of neutrinos by decaying particles,* JCAP **05**, 008 (2007).

[171] K. Enqvist, S. Nadathur, T. Sekiguchi, and T. Takahashi, *Decaying dark matter and the tension in σ_8,* JCAP **09**, 067 (2015).

[172] E. Di Valentino and S. Bridle, *Exploring the Tension between Current Cosmic Microwave Background and Cosmic Shear Data,* Symmetry **10**, 585 (2018).

[173] Z. Berezhiani, A. D. Dolgov, and I. I. Tkachev, *Reconciling Planck results with low redshift astronomical measurements,* Phys. Rev. D**92**, 061303 (2015).

[174] R. C. Nunes, *Structure formation in f(T) gravity and a solution for H_0 tension,* JCAP**2018**, 052 (2018).

[175] S. Anand, P. Chaubal, A. Mazumdar, and S. Mohanty, *Cosmic viscosity as a remedy for tension between PLANCK and LSS data,* JCAP**2017**, 005 (2017).

[176] S. Kumar, R. C. Nunes, and S. K. Yadav, *Cosmological bounds on dark matter-photon coupling,* Phys. Rev. D**98**, 043521 (2018).

[177] A. Chudaykin, D. Gorbunov, and I. Tkachev, *Dark matter component decaying after recombination: Lensing constraints with Planck data,* Phys. Rev. D**94**, 023528 (2016).

[178] J. L. Bernal, L. Verde, and A. G. Riess, *The trouble with H_0,* JCAP **10**, 019 (2016).

[179] J. Evslin, A. A. Sen, and Ruchika, *Price of shifting the Hubble constant,* Phys. Rev. D **97**, 103511 (2018).

[180] K. Aylor, M. Joy, L. Knox, M. Millea, S. Raghunathan, and W. K. Wu, *Sounds Discordant: Classical Distance Ladder & ΛCDM -based Determinations of the Cosmological Sound Horizon,* Astrophys. J. **874**, 4 (2019).

[181] T. Johannsen and D. Psaltis, *Testing the No-Hair Theorem with Observations in the Electromagnetic Spectrum: II. Black-Hole Images,* Astrophys. J. **718**, 446–454 (2010).

[182] T. Weiler, *Resonant absorption of cosmic-ray neutrinos by the relic-neutrino background,* Phys. Rev. Lett. **49**, 234–237 (1982).

[183] T. J. Weiler, *Relic neutrinos, Z bursts, and cosmic rays above 10**20-eV,* in "Beyond the desert: Accelerator, non-accelerator and space approaches into the next millennium. Proceedings, 2nd International Conference on particle physics beyond the standard model, Ringberg Castle, Tegernsee, Germany, June 6-12, 1999," (1999), pp. 1085–1106.

[184] S. Yoshida, *Propagation of ultrahigh-energy neutrinos in the black body neutrino field,* Astropart. Phys. **2**, 187–198 (1994).

[185] S. Yoshida, H.-y. Dai, C. C. H. Jui, and P. Sommers, *Extremely high-energy neutrinos and their detection,* Astrophys. J. **479**, 547–559 (1997).

[186] Y. Farzan and S. Palomares-Ruiz, *Dips in the Diffuse Supernova Neutrino Background,* JCAP **1406**, 014 (2014).

[187] M. Ibe and K. Kaneta, *Cosmic neutrino background absorption line in the neutrino spectrum at IceCube,* Phys. Rev. **D90**, 053011 (2014).

[188] C.-Y. Chen, P. S. Bhupal Dev, and A. Soni, *Standard model explanation of the ultrahigh energy neutrino events at IceCube,* Phys. Rev. **D89**, 033012 (2014).

[189] S. Palomares-Ruiz, A. C. Vincent, and O. Mena, *Spectral analysis of the high-energy IceCube neutrinos,* Phys. Rev. **D91**, 103008 (2015).

[190] N. Mileo, A. de la Puente, and A. Szynkman, *Implications of a Electroweak Triplet Scalar Leptoquark on the Ultra-High Energy Neutrino Events at IceCube,* JHEP **11**, 124 (2016).

[191] S. Gabriel and S. Nandi, *A New two Higgs doublet model,* Phys. Lett. **B655**, 141–147 (2007).

[192] P. A. N. Machado, Y. F. Perez, O. Sumensari, Z. Tabrizi, and R. Z. Funchal, *On the Viability of Minimal Neutrinophilic Two-Higgs-Doublet Models,* JHEP **12**, 160 (2015).

[193] A. Datta, M. Guchait, and A. Pilaftsis, *Probing lepton number violation via majorana neutrinos at hadron supercolliders,* Phys. Rev. D **50**, 3195–3203 (1994).

[194] F. M. L. Almeida, Jr., Y. do Amaral Coutinho, J. A. Martins Simoes, and M. A. B. Vale, do., *On a signature for heavy Majorana neutrinos in hadronic collisions,* Phys. Rev. D **62**, 075004 (2000).

[195] O. Panella, M. Cannoni, C. Carimalo, and Y. N. Srivastava, *Signals of heavy Majorana neutrinos at hadron colliders,* Phys. Rev. D **65**, 035005 (2002).

[196] T. Han and B. Zhang, *Signatures for Majorana neutrinos at hadron colliders,* Phys. Rev. Lett. **97**, 171804 (2006).

[197] F. del Aguila, J. A. Aguilar-Saavedra, and R. Pittau, *Heavy neutrino signals at large hadron colliders,* JHEP **10**, 047 (2007).

[198] N. Haba, S. Matsumoto, and K. Yoshioka, *Observable Seesaw and its Collider Signatures,* Phys. Lett. B **677**, 291–295 (2009).

[199] O. Seto, *Large invisible decay of a Higgs boson to neutrinos,* Phys. Rev. **D92**, 073005 (2015).

[200] G. Bhattacharyya, S. Banerjee, and P. Roy, *Oblique electroweak corrections and new physics,* Phys. Rev. D **45**, R729–R733 (1992).

[201] S. Sadhukhan and S. Mohanty, *Explanation of IceCube spectrum with $\nu \to 3\nu$ neutrino splitting in a ν2HDM model,* (2018).

[202] E. Bertuzzo, Y. F. Perez G., O. Sumensari, and R. Zukanovich Funchal, *Limits on Neutrinophilic Two-Higgs-Doublet Models from Flavor Physics,* JHEP **01**, 018 (2016).

[203] M. Sher and C. Triola, *Astrophysical Consequences of a Neutrinophilic Two-Higgs-Doublet Model,* Phys. Rev. **D83**, 117702 (2011).

[204] D. Williams, *Recent Results from IceCube,* Int. J. Mod. Phys. Conf. Ser. **46**, 1860048 (2018).

[205] E. Ma, *Naturally small seesaw neutrino mass with no new physics beyond the TeV scale,* Phys. Rev. Lett. **86**, 2502–2504 (2001).

[206] D. N. Spergel and P. J. Steinhardt, *Observational evidence for selfinteracting cold dark matter,* Phys. Rev. Lett. **84**, 3760–3763 (2000).

[207] S. Tulin and H.-B. Yu, *Dark Matter Self-interactions and Small Scale Structure,* Phys. Rept. **730**, 1–57 (2018).

[208] M. Kuhlen, M. Vogelsberger, and R. Angulo, *Numerical Simulations of the Dark Universe: State of the Art and the Next Decade,* Phys. Dark Univ. **1**, 50–93 (2012).

[209] M. Rocha, A. H. G. Peter, J. S. Bullock, M. Kaplinghat, S. Garrison-Kimmel, J. Onorbe, and L. A. Moustakas, *Cosmological Simulations with Self-Interacting Dark Matter I: Constant Density Cores and Substructure,* Mon. Not. Roy. Astron. Soc. **430**, 81–104 (2013).

[210] J. F. Navarro, C. S. Frenk, and S. D. M. White, *A Universal density profile from hierarchical clustering,* Astrophys. J. **490**, 493–508 (1997).

[211] M. Kaplinghat, S. Tulin, and H.-B. Yu, *Dark matter halos as particle colliders: Unified solution to small-scale structure puzzles from dwarfs to clusters,* Phys. Rev. Lett. **116**, 041302 (2016).

[212] M. G. Aartsen *et al.*, *Differential limit on the extremely-high-energy cosmic neutrino flux in the presence of astrophysical background from nine years of IceCube data,* Phys. Rev. **D** (2018). [Phys. Rev.D98,062003(2018)].

[213] W. Hu and I. Sawicki, *Models of f(R) Cosmic Acceleration that Evade Solar-System Tests,* Phys. Rev. **D76**, 064004 (2007).

[214] E. Di Valentino, A. Melchiorri, E. V. Linder, and J. Silk, *Constraining Dark Energy Dynamics in Extended Parameter Space,* Phys. Rev. **D96**, 023523 (2017).

[215] J. Dossett, B. Hu, and D. Parkinson, *Constraining models of f(R) gravity with Planck and WiggleZ power spectrum data,* JCAP **1403**, 046 (2014).

[216] B. Hu, M. Raveri, M. Rizzato, and A. Silvestri, *Testing HuSawicki f(R) gravity with the effective field theory approach,* Mon. Not. Roy. Astron. Soc. **459**, 3880–3889 (2016).

[217] C. Brans and R. H. Dicke, *Mach's principle and a relativistic theory of gravitation,* Phys. Rev. **124**, 925–935 (1961).

[218] D. Lovelock, *The einstein tensor and its generalizations,* Journal of Mathematical Physics **12**, 498–501 (1971).

[219] V. A. Kostelecky, *Gravity, Lorentz violation, and the standard model,* Phys. Rev. **D69**, 105009 (2004).

[220] J. Khoury and A. Weltman, *Chameleon fields: Awaiting surprises for tests of gravity in space,* Phys. Rev. Lett. **93**, 171104 (2004).

[221] P. Brax, A.-C. Davis, B. Li, and H. A. Winther, *A Unified Description of Screened Modified Gravity,* Phys. Rev. **D86**, 044015 (2012).

[222] P. Brax, A.-C. Davis, and B. Li, *Modified Gravity Tomography,* Phys. Lett. **B715**, 38–43 (2012).

[223] A. De Felice and S. Tsujikawa, *f(R) theories,* Living Rev. Rel. **13**, 3 (2010).

[224] T. P. Sotiriou, *f(R) gravity and scalar-tensor theory,* Class. Quant. Grav. **23**, 5117–5128 (2006).

[225] G.-B. Zhao, B. Li, and K. Koyama, *N-body Simulations for f(R) Gravity using a Self-adaptive Particle-Mesh Code,* Phys. Rev. D **83**, 044007 (2011).

[226] M. Baldi, F. Villaescusa-Navarro, M. Viel, E. Puchwein, V. Springel, and L. Moscardini, *Cosmic degeneracies – I. Joint N-body simulations of modified gravity and massive neutrinos,* Mon. Not. Roy. Astron. Soc. **440**, 75–88 (2014).

[227] C. Llinares, D. F. Mota, and H. A. Winther, *ISIS: a new N-body cosmological code with scalar fields based on RAMSES. Code presentation and application to the shapes of clusters,* Astron. Astrophys. **562**, A78 (2014).

[228] L. Lombriser, K. Koyama, and B. Li, *Halo modelling in chameleon theories,* JCAP **03**, 021 (2014).

[229] H. A. Winther *et al.*, *Modified Gravity N-body Code Comparison Project,* Mon. Not. Roy. Astron. Soc. **454**, 4208–4234 (2015).

[230] P. Brax and P. Valageas, *Impact on the power spectrum of Screening in Modified Gravity Scenarios,* Phys. Rev. **D88**, 023527 (2013).

[231] G.-B. Zhao, L. Pogosian, A. Silvestri, and J. Zylberberg, *Searching for modified growth patterns with tomographic surveys,* Phys. Rev. **D79**, 083513 (2009).

[232] A. Hojjati, L. Pogosian, and G.-B. Zhao, *Testing gravity with CAMB and CosmoMC,* JCAP **1108**, 005 (2011).

[233] Y. S. Song, W. Hu, and I. Sawicki, *The Large Scale Structure of f(R) Gravity,* Phys. Rev. **D75**, 044004 (2007).

[234] E. Bertschinger, *On the Growth of Perturbations as a Test of Dark Energy,* Astrophys. J. **648**, 797–806 (2006).

[235] P. Zhang, *Testing $f(R)$ gravity against the large scale structure of the universe.* Phys. Rev. **D73**, 123504 (2006).

[236] A. G. Riess *et al.*, *Observational evidence from supernovae for an accelerating universe and a cosmological constant,* Astron. J. **116**, 1009–1038 (1998).

[237] S. Perlmutter *et al.*, *Measurements of Omega and Lambda from 42 high redshift supernovae,* Astrophys. J. **517**, 565–586 (1999).

[238] D. M. Scolnic *et al.*, *The Complete Light-curve Sample of Spectroscopically Confirmed SNe Ia from Pan-STARRS1 and Cosmological Constraints from the Combined Pantheon Sample,* Astrophys. J. **859**, 101 (2018).

[239] L. H. Ford, *Cosmological-constant damping by unstable scalar fields,* Phys. Rev. D **35**, 2339–2344 (1987).

[240] B. Ratra and P. J. E. Peebles, *Cosmological consequences of a rolling homogeneous scalar field,* Phys. Rev. D **37**, 3406–3427 (1988).

[241] T. Chiba, N. Sugiyama, and T. Nakamura, *Cosmology with x matter,* Mon. Not. Roy. Astron. Soc. **289**, L5–L9 (1997).

[242] R. J. F. Marcondes, *Interacting dark energy models in Cosmology and large-scale structure observational tests,* Ph.D. thesis (2016).

[243] M. Chevallier and D. Polarski, *Accelerating universes with scaling dark matter,* Int. J. Mod. Phys. **D10**, 213–224 (2001).

[244] E. V. Linder, *Exploring the expansion history of the universe,* Phys. Rev. Lett. **90**, 091301 (2003).

[245] H. K. Jassal, J. S. Bagla, and T. Padmanabhan, *Understanding the origin of CMB constraints on Dark Energy,* Mon. Not. Roy. Astron. Soc. **405**, 2639–2650 (2010).

[246] G. Efstathiou, *Constraining the equation of state of the universe from distant type Ia supernovae and cosmic microwave background anisotropies,* Mon. Not. Roy. Astron. Soc. **310**, 842–850 (1999).

[247] E. M. Barboza, Jr. and J. S. Alcaniz, *A parametric model for dark energy,* Phys. Lett. **B666**, 415–419 (2008).

[248] G.-B. Zhao *et al.*, *Dynamical dark energy in light of the latest observations,* Nat. Astron. **1**, 627–632 (2017).

[249] W. Yang, R. C. Nunes, S. Pan, and D. F. Mota, *Effects of neutrino mass hierarchies on dynamical dark energy models,* Phys. Rev. D **95**, 103522 (2017).

[250] E. Di Valentino, *Crack in the cosmological paradigm,* Nature Astron. **1**, 569–570 (2017).

[251] M. Rezaei, M. Malekjani, S. Basilakos, A. Mehrabi, and D. F. Mota, *Constraints to Dark Energy Using PADE Parameterizations,* Astrophys. J. **843**, 65 (2017).

[252] R. J. F. Marcondes and S. Pan, *Cosmic chronometers constraints on some fast-varying dark energy equations of state,* (2017).

[253] W. Yang, S. Pan, and A. Paliathanasis, *Latest astronomical constraints on some non-linear parametric dark energy models,* Mon. Not. Roy. Astron. Soc. **475**, 2605–2613 (2018).

[254] S. Vagnozzi, S. Dhawan, M. Gerbino, K. Freese, A. Goobar, and O. Mena, *Constraints on the sum of the neutrino masses in dynamical dark energy models with $w(z) \geq -1$ are tighter than those obtained in ΛCDM,* (2018).

[255] J. Lesgourgues and S. Pastor, *Massive neutrinos and cosmology,* Phys. Rept. **429**, 307–379 (2006).

[256] J. Lesgourgues, G. Mangano, G. Miele, and S. Pastor, *Neutrino cosmology,* (2013).

[257] P. F. de Salas and S. Pastor, *Relic neutrino decoupling with flavour oscillations revisited,* JCAP **1607**, 051 (2016).

[258] C.-P. Ma and E. Bertschinger, *Cosmological perturbation theory in the synchronous and conformal Newtonian gauges,* Astrophys. J. **455**, 7–25 (1995).

[259] A. Lewis, A. Challinor, and A. Lasenby, *Efficient computation of CMB anisotropies in closed FRW models,* Astrophys. J. **538**, 473–476 (2000).

[260] A. Lewis and S. Bridle, *Cosmological parameters from CMB and other data: A Monte Carlo approach,* Phys. Rev. **D66**, 103511 (2002).

[261] I. Banerjee, S. Chakraborty, and S. SenGupta, *Silhouette of M87*: A New Window to Peek into the World of Hidden Dimensions,* Phys. Rev. **D101**, 041301 (2020).

[262] V. I. Dokuchaev and N. O. Nazarova, *Silhouettes of invisible black holes,* (2019).

[263] S. O. Alexeyev and V. A. Prokopov, *Shadows from spinning black holes in extended gravity,* (2020).

[264] R. Kumar, S. G. Ghosh, and A. Wang, *Light Deflection and Shadow Cast by Rotating Kalb-Ramond Black Holes,* (2020).

[265] A. Sen, *Rotating charged black hole solution in heterotic string theory,* Phys. Rev. Lett. **69**, 1006–1009 (1992).

[266] C. Y. Kuo *et al.*, *Measuring Mass Accretion Rate onto the Supermassive Black Hole in M87 Using Faraday Rotation Measure with the Submillimeter Array,* Astrophys. J. **783**, L33 (2014).

[267] F. N. Owen, J. A. Eilek, and W. C. Keel, *Detection of Large Faraday Rotation in the Inner 2 Kiloparsecs of M87,* apj **362**, 449 (1990).

[268] J.-C. Algaba, K. Asada, and M. Nakamura, *Resolving the Rotation Measure of the m87 jet on Kiloparsec Scales,* Astrophys. J. **823**, 86 (2016).

[269] W. Junor, J. A. Biretta, and J. F. C. Wardle, *VLBA lambda lambda 6, 4 cm polarimetry of Vir A,* in "Galaxies and their Constituents at the Highest Angular Resolutions," , vol. 205 of *IAU Symposium*, R. T. Schilizzi, ed. (2001), vol. 205 of *IAU Symposium*, p. 136.

[270] R. T. Zavala and G. B. Taylor, *Faraday rotation measures in the parsec-scale jets of the radio galaxies m87, 3c 111, and 3c 120,* Astrophys. J. **566**, L9 (2002).

[271] Y. Chen, J. Shu, X. Xue, Q. Yuan, and Y. Zhao, *Probing Axions with Event Horizon Telescope Polarimetric Measurements,* Phys. Rev. Lett. **124**, 061102 (2020).

[272] G. N. Gyulchev and S. S. Yazadjiev, *Kerr-Sen dilaton-axion black hole lensing in the strong deflection limit,* Phys. Rev. **D75**, 023006 (2007).

[273] G. N. Gyulchev and S. S. Yazadjiev, *Analytical Kerr-Sen Dilaton-Axion Black Hole Lensing in the Weak Deflection Limit,* Phys. Rev. D **81**, 023005 (2010).

[274] R. Uniyal, H. Nandan, and P. Jetzer, *Bending angle of light in equatorial plane of KerrSen Black Hole,* Phys. Lett. **B782**, 185–192 (2018).

[275] C. Liu, C. Ding, and J. Jing, *Periodic orbits around Kerr Sen black holes,* Commun. Theor. Phys. **71**, 1461 (2019).

[276] J. An, J. Peng, Y. Liu, and X.-H. Feng, *Kerr-Sen Black Hole as Accelerator for Spinning Particles,* Phys. Rev. D **97**, 024003 (2018).

[277] H. M. Siahaan, *Merger estimates for Kerr-Sen black holes,* Phys. Rev. D **101**, 064036 (2020).

[278] K. Hioki and U. Miyamoto, *Hidden symmetries, null geodesics, and photon capture in the Sen black hole,* Phys. Rev. **D78**, 044007 (2008).

[279] S.-W. Wei and Y.-X. Liu, *Observing the shadow of Einstein-Maxwell-Dilaton-Axion black hole,* JCAP **11**, 063 (2013).

[280] S. Dastan, R. Saffari, and S. Soroushfar, *Shadow of a Kerr-Sen dilaton-axion Black Hole,* (2016).

[281] S. Soroushfar, R. Saffari, and E. Sahami, *Geodesic equations in the static and rotating dilaton black holes: Analytical solutions and applications,* Phys. Rev. D **94**, 024010 (2016).

[282] Z. Younsi, A. Zhidenko, L. Rezzolla, R. Konoplya, and Y. Mizuno, *New method for shadow calculations: Application to parametrized axisymmetric black holes,* Phys. Rev. D **94**, 084025 (2016).

[283] R. Uniyal, H. Nandan, and K. D. Purohit, *Null geodesics and observables around the KerrSen black hole,* Class. Quant. Grav. **35**, 025003 (2018).

[284] X. Lan and J. Pu, *Observing the contour profile of a Kerr–Sen black hole,* Mod. Phys. Lett. A **33**, 1850099 (2018).

[285] B. Gwak, *Cosmic Censorship Conjecture in Kerr-Sen Black Hole,* Phys. Rev. D **95**, 124050 (2017).

[286] B. Gwak, *Weak Cosmic Censorship in Kerr-Sen Black Hole under Charged Scalar Field,* JCAP **03**, 058 (2020).

[287] B. A. Campbell, N. Kaloper, R. Madden, and K. A. Olive, *Physical properties of four-dimensional superstring gravity black hole solutions,* Nucl. Phys. **B399**, 137–168 (1993).

[288] M. Guo, S. Song, and H. Yan, *Observational signature of a near-extremal Kerr-Sen black hole in the heterotic string theory,* Phys. Rev. D **101**, 024055 (2020).

[289] X.-H. Feng and H. Lu, *On the size of rotating black holes,* Eur. Phys. J. C **80**, 551 (2020).

[290] S. Ferrara, J. Scherk, and B. Zumino, *Algebraic Properties of Extended Supergravity Theories,* Nucl. Phys. **B121**, 393–402 (1977).

[291] E. Cremmer, J. Scherk, and S. Ferrara, *U(n) Invariance in Extended Supergravity,* Phys. Lett. **68B**, 234–238 (1977).

[292] E. Cremmer, J. Scherk, and S. Ferrara, *SU(4) Invariant Supergravity Theory,* Phys. Lett. **74B**, 61–64 (1978).

[293] E. Cremmer and J. Scherk, *Algebraic Simplifications in Supergravity Theories,* Nucl. Phys. **B127**, 259–268 (1977).

[294] E. Cremmer and B. Julia, *The SO(8) Supergravity,* Nucl. Phys. **B159**, 141–212 (1979).

[295] M. de Roo, *GAUGED N=4 MATTER COUPLINGS,* Phys. Lett. **156B**, 331–334 (1985).

[296] L. Castellani, A. Ceresole, S. Ferrara, R. D'Auria, P. Fre, and E. Maina, *The Complete $N = 3$ Matter Coupled Supergravity,* Nucl. Phys. **B268**, 317–348 (1986).

[297] L. Castellani, A. Ceresole, R. D'Auria, S. Ferrara, P. Fre, and E. Maina, *σ Models, Duality Transformations and Scalar Potentials in Extended Supergravities,* Phys. Lett. **161B**, 91 (1985). [,91(1985)].

[298] S. Cecotti, S. Ferrara, and L. Girardello, *Hidden Noncompact Symmetries in String Theory,* Nucl. Phys. **B308**, 436–450 (1988).

[299] G. Veneziano, *Scale factor duality for classical and quantum strings,* Phys. Lett. **B265**, 287–294 (1991).

[300] M. J. Duff, *Duality Rotations in String Theory,* Nucl. Phys. **B335**, 610 (1990).

[301] K. A. Meissner and G. Veneziano, *Symmetries of cosmological superstring vacua,* Phys. Lett. **B267**, 33–36 (1991).

[302] K. A. Meissner and G. Veneziano, *Manifestly O(d,d) invariant approach to space-time dependent string vacua,* Mod. Phys. Lett. **A6**, 3397–3404 (1991).

[303] M. Gasperini, J. Maharana, and G. Veneziano, *From trivial to nontrivial conformal string backgrounds via O(d,d) transformations,* Phys. Lett. **B272**, 277–284 (1991).

[304] A. Sen, *O(d) x O(d) symmetry of the space of cosmological solutions in string theory, scale factor duality and two-dimensional black holes,* Phys. Lett. **B271**, 295–300 (1991).

[305] J. H. Horne, G. T. Horowitz, and A. R. Steif, *An Equivalence between momentum and charge in string theory,* Phys. Rev. Lett. **68**, 568–571 (1992).

[306] R. P. Kerr, *Gravitational field of a spinning mass as an example of algebraically special metrics,* Phys. Rev. Lett. **11**, 237–238 (1963).

[307] A. de Vries, *The apparent shape of a rotating charged black hole, closed photon orbits and the bifurcation setA4,* Classical and Quantum Gravity **17**, 123–144 (1999).

[308] A. Zakharov, A. Nucita, F. DePaolis, and G. Ingrosso, *Measuring the black hole parameters in the galactic center with radioastron,* New Astronomy **10**, 479 – 489 (2005).

[309] Zakharov, A. F., De Paolis, F., Ingrosso, G., and Nucita, A. A., *Direct measurements of black hole charge with future astrometrical missions,* A&A **442**, 795–799 (2005).

[310] R. H. Boyer and R. W. Lindquist, *Maximal analytic extension of the kerr metric,* Journal of Mathematical Physics **8**, 265–281 (1967).

[311] B. Carter, *Global structure of the Kerr family of gravitational fields,* Phys. Rev. **174**, 1559–1571 (1968).

[312] P. A. Blaga and C. Blaga, *Bounded radial geodesics around a Kerr-Sen black hole,* Class. Quant. Grav. **18**, 3893–3905 (2001).

[313] P. J. Young, *Capture of particles from plunge orbits by a black hole,* Phys. Rev. **D14**, 3281–3289 (1976).

[314] C. Gooding and A. V. Frolov, *Five-Dimensional Black Hole Capture Cross-Sections,* Phys. Rev. **D77**, 104026 (2008).

[315] C. Bambi, K. Freese, S. Vagnozzi, and L. Visinelli, *Testing the rotational nature of the supermassive object M87* from the circularity and size of its first image,* Phys. Rev. **D100**, 044057 (2019).

[316] O. Yu. Tsupko, *Analytical calculation of black hole spin using deformation of the shadow,* Phys. Rev. **D95**, 104058 (2017).

[317] F. Wilczek, *Two Applications of Axion Electrodynamics,* Phys. Rev. Lett. **58**, 1799 (1987).

[318] S. M. Carroll, G. B. Field, and R. Jackiw, *Limits on a Lorentz and Parity Violating Modification of Electrodynamics,* Phys. Rev. **D41**, 1231 (1990).

[319] S. M. Carroll and G. B. Field, *The Einstein equivalence principle and the polarization of radio galaxies,* Phys. Rev. **D43**, 3789 (1991).

[320] D. Harari and P. Sikivie, *Effects of a Nambu-Goldstone boson on the polarization of radio galaxies and the cosmic microwave background,* Phys. Lett. **B289**, 67–72 (1992).

[321] A. Uranga, *String theory phenomenology,* J. Phys. Conf. Ser. **259**, 012014 (2010).

List of Publications

Thesis related Publications

1. G. Lambise, S. Mohanty,**Ashish Narang** and P. Parashari,
   Tesing dark energy models in the light of σ_8 tension
   Eur.Phys.J.C **79** (2019) 2, 141. arXiv: 1804.07154

2. S. Mohanty,**Ashish Narang** and S. Sadhukhan,
   Cut-off of IceCube neutrino spectrum due to t-channel resonant absorption by CνB
   JCAP 03 (2019) 041. arXiv:1808.01272

3. **Ashish Narang**, S. Mohanty and A. Kumar,
   Test of Kerr-Sen metric with black hole observations
   arXiv:2002.12786 (Under review in Phys. Rev. D)

Publications not part of this thesis

1. B. Chauhan, B. Kindra, **Ashish Narang**,
   Discrepancies in simultaneous explanation of flavor anomalies and IceCube PeV events using leptoquarks
   Phys.Rev.D **97** 095007 (2018). arXiv:1706.04598